University of Nottingham
UK | CHINA | MALAYSIA

Semiconductor and Circuit Modelling Methods for Next Generation RF Protection Devices

Thesis submitted to the University of Nottingham for the degree of **PhD Physics, 11th September 2024.**

Luke Matthews

14341986

Supervised by

Dr. Christopher Mellor
Prof. Ana Vukovic
Prof. Phillip Sewell
Prof. Trevor Benson

Abstract

This thesis explores modelling a receiver protector system (RxP) in unprecedented detail. Using the UTLM method and software developed at the University of Nottingham by Prof. Phil Sewell and Prof Ana Vukovic, the research presented in this thesis uses detailed simulations to initially explore the effects of adding some of the key components in a piecewise manner. Predictably, the inclusion of the inductive post has the most significant impact on the performance, with the diameter of the post varied and investigated, along with the diameter of the upper boss and lower cavity and the depth of protrusion for both the upper boss and lower cavity.

Furthermore, a detailed analysis of the PiN diode model structure is presented. Progressing the model of the diode from a solid metallic block with simple behaviour, to a model of a silicon PiN diode where each of the 3 layers is defined individually, it is hoped that this final model can then be the foundations for further research into the semiconductors that drive RxP systems.

Finally, an exploration into the scattering effects of the RxP system is presented. The inductive post has the capability of scattering the incident signal, some of which excite modes with higher cut-off frequencies. Which modes are excited and what criteria they most fulfil are also considered. The scattering into higher order modes presented in this research is an as yet unexplored area of study in electromagnetic simulation work.

The results presented here offer an insight into the behaviour of the RxP system above the desired operating band and indicate what happens to the "lost" power at higher frequencies.

This research was impacted by the 2020 COVID-19 Pandemic, with restrictions in the UK limiting access to required infrastructure and reducing the collaboration opportunities with some stakeholders. Furthermore, as this research is based around modelling a practical system, commercial sensitivities have mean that some parameters have been modified and other elements remain unpublished to protect the IP of the industry advisors. Nonetheless, the data presented in this thesis provides a detailed analysis of specific elements of the RxP, a detailed development of the PiN diode model and an interesting exploration of the scattering effects of the RxP at frequencies higher than the operating band, and how the response of the system at these frequencies is similar to that of a high-pass filter.

Acknowledgements

There are many people to thank that have helped me along on this momentous journey and I am truly humbled, grateful and indebted to you all in different ways. Thank You! Special thanks goes to the EPSRC for funding my endeavours for the last years.

I would like to express in particular my gratitude to my supervisors, Chris, Ana, Phil and Trevor. Thank you all for allowing me to darken your door with endless questions, difficulties, results and ideas. Thank you for helping me through my woes, celebrating my successes and guiding me on the right path to the end of my PhD. I could not have reached the end without you, thank you for bringing me on this roller-coaster and helping me through it to the end!

I am also extremely grateful to Keith, Gary and the team at e2V Technologies, Lincoln for their guidance on the more practical aspects of this project, for answering my technical questions and for providing me with data, measurements and diodes to study, allowing me to confirm my simulations were as realistic as possible.

I would be remiss in not mentioning thanks to my parents for their helping with looking after the children and for their continued support, encouragement and care, thank you!

I would like to thank God for giving me the gifts of strength, knowledge and perseverance, for helping me through to the end and for blessing me with such a beautiful family. I pray that this be the work of His hands and that it may inspire and help others in the future.

Last but by no means least, I would like to give my most special thanks to my wonderful wife, parents and three beautiful children, for being by my side throughout this project. I can't express enough how invaluable your love, care, support, cuddles and smiles have been throughout this project and I look forward to the exciting years ahead with you all and (hopefully) repaying you by supporting you through your own projects.

Publications

Elements of this research were published in a workshop delivered at 14th European Conference on Antennas and Propagation (EuCAP) in 2020. The associated paper is available on IEEE Xplore. The title and abstract are presented below:

Luke Matthews; Ana Vukovic; Chris Mellor; Phil Sewell; Trevor Benson *"Time-Domain Modelling of Solid State RF Receiver Protection Systems,"* 2020 14th European Conference on Antennas and Propagation (EuCAP), Copenhagen, Denmark, 2020, pp. 1-5,

doi: 10.23919/$EuCAP$48036.2020.9135249.

Abstract: We investigate the effects of switching the state of a PIN diode from insulating to conducting as a component within a Solid-State Receiver Protection (SSRP) system. The investigation follows a component adding process, ultimately arriving at a full configuration of a metallic post insulated from the waveguide by two dielectric blocks in the Off-state, which is then connected at one end in the On-state. The effects of the diameter of the post are also studied. The S-parameters of the system are calculated from the voltage and current transmission line observations sampled directly with a single time-domain numerical method based upon an unstructured mesh.

URL: $https://ieeexplore.ieee.org/stamp/stamp.jsp?tp=\&arnumber=9135249\&isnumber=9135070$

Contents

Abstract i

Acknowledgements iii

Publications iii

List of Tables viii

List of Figures ix

Abbreviations xii

Chapter 1 Introduction 1

1.1 Background 2

1.2 Motivation for this Research 10

1.3 Thesis Outline 13

Chapter 2 The Basic Principles of Electromagnetism, Microwave and Electronic Engineering 16

2.1 Electromagnetism 17

2.2 Electronic and Microwave Engineering 19

2.3 Transmission Lines 20

2.4 Waveguide Theory 23

2.5 Microwave Analysis 41

Chapter 3 Modelling Microwave Waveguides and RxP Components 49

3.1 Overview 50

3.2 Common EM Modelling Techniques 51

3.3 The Unstructured Transmission Line Modelling Method (UTLM) 71
3.4 Receiver Protectors (RxPs) in Literature 73
3.5 Analytical Waveguide Models 75

Chapter 4 Piecewise Analysis of an RxP 85

4.1 Introduction 86
4.2 Method 86
4.3 Construction of the RxP 89
4.4 Empty Waveguide 90
4.5 Adding the Post 92
4.6 Adding the Upper Boss 99
4.7 Adding the Lower Cavity 108
4.8 Other Components 113

Chapter 5 Semiconductor Physics and PiN Diodes 115

5.1 Semiconductor Physics Basics 115
5.2 PiN Diode Basics 123
5.3 PiN Diode Uses and Applications 126

Chapter 6 PiN Diode Modelling Techniques: A Review 129

6.1 EM Fields and Equivalent Circuits 130
6.2 The Development of TLM 131
6.3 Expansion of TLM 133
6.4 Non-Linear Component Behaviour 136
6.5 Behavioural Modelling and Modern Day Simulations 137
6.6 Motivation 139
6.7 Model Integration 140
6.8 SPICE Model 141
6.9 IBIS Model 143
6.10 IBIS - SPICE Compatibility 146

6.11 Diode Models in Simulations 147

Chapter 7 A Systematic Approach to Modelling a PiN Diode 152

7.1 Introduction and Motivation 153

7.2 Investigation Outline 154

7.3 Model 1 - The Simple Switching Block 159

7.4 Stage 2 - 2 Switching Blocks 163

7.5 Stage 3 - Adding the Ribbons 168

7.6 Stage 4 - Introducing Surface Layers 172

7.7 Stage 5 - Surface Layer PiN Diode Model 176

7.8 Scattering Effects 182

7.9 Conclusions 187

Chapter 8 Conclusions and Future Research Directions 189

8.1 Chapter Summaries 189

8.2 Key Results 192

8.3 Further Development and Research Ideas 197

8.4 Concluding Remarks 199

Bibliography 201

List of Tables

2.1 Dielectric Constants 21

2.2 TE-mode cut-off frequencies 39

7.1 Key Simulation Parameter Definitions 157

7.2 Diode Stage 1 Key Simulation Parameters 162

7.3 Diode Stage 2 Key Simulation Parameters 165

7.4 Diode Stage 3 Key Simulation Parameters 169

7.5 Diode Stage 4 Key Simulation Parameters 174

7.6 Diode Stage 5 Key Simulation Parameters 178

List of Figures

1.1 Schematic of a RADAR System 3
1.2 Waveguide Receiver image 7
1.3 Primitive Waveguide-Post Mesh 7
1.4 Rectangular Waveguide Dimensions 8
1.5 4-Port Waveguide Directional Filter 9

2.1 Commutative Diagram of Harmonic Wave Properties 24
2.2 Rectangular Waveguide Dimensions 25
2.3 Two graphs illustrating transmission and reflection characteristics using S-Parameters 45

3.1 Yee Cell 58
3.2 Series and Shunt Nodes 60
3.3 Symmetrical Condensed Node 65
3.4 Staircasing Error 70
3.5 UTLM Primitive Mesh 72
3.6 Lossless Transmission line 76
3.7 The Marcuvitz equivalent circuit for an inductive post in a waveguide 80
3.8 T- Network for a general discontinuity 81

4.1 Modelling Phases Flow Chart 87
4.2 Example Time Domain data for calculating the required number of time steps 88
4.3 Simulation Data from an Empty Waveguide 91

4.4 Post Diameter Investigation 93
4.5 Post Sides Investigation Data 95
4.6 Simulation Data from Post Diameter Investigation1 97
4.7 Simulation Data from Post Diameter Investigation 2 98
4.8 Boss Diameter Investigation 100
4.9 Simulation Data from Boss Diameter Investigation 1 102
4.10 Simulation Data from Boss Diameter Investigation 2 103
4.11 Boss Depth Investigation 105
4.12 Simulation Data from Boss Depth Investigation 2 106
4.13 Simulation Data from Boss Depth Investigation 2 107
4.14 Cavity Diameter Investigation 109
4.15 Simulation Data from Cavity Diameter Investigation 1 . . . 111
4.16 Simulation Data from Cavity Diameter Investigation 2 . . . 112

5.1 Semiconductor Bandgap 116
5.2 Semiconductor Elements 118
5.3 pn Junction 121

6.1 Series and Shunt Nodes 131
6.2 Symmetrical Condensed Node 134
6.3 The integration of the SPICE model with FDTD simulation (a) and the interface between the SPICE model and FDTD (b) are some of the key features of modern SPICE modelling techniques. 142
6.4 SPICE models can also be integrated into TLM (a), using an equivalent circuit at the interface (b). 150
6.5 Diagram showing the 1-D TLM circuit modeling the IBIS package parasitics between the non-linear IBIS source/load on the left and the 3-D field TLM on the right. [1] 151

7.1 X-ray tomography rendering of a PiN diode 155
7.2 Model Development Pathway 158
7.3 Single "Switching Block" Model Geometry - Diode Model Development Stage 1 159
7.4 Simulation data for Diode Model Stage 1 161
7.5 Two "Switching Block" Model Geometry - Diode Model Development Stage 2 164
7.6 Simulation data for Diode Model Stage 2 166
7.7 Two "Switching Blocks" with Bonding Ribbons Model Geometry - Diode Model Development Stage 3 168
7.8 Simulation data for Diode Model Stage 3 171
7.9 Physical I-Layer, Surface P- and N- Layer Geometry - Diode Model Development Stage 4 173
7.10 Simulation data for Diode Model Stage 4 175
7.11 Surface Layer Diode Representation Geometry - Diode Model Development Stage 5 177
7.12 Simulation data for Diode Model Stage 5 179
7.13 Simulation data for Diode Model Stage 5 up to 20 GHz . . . 181
7.14 Simulation data for Higher Mode Transmission 184
7.15 Power Analysis of Higher Modes 185
7.16 Field lines of some of the lower order modes of a rectangular waveguide 186

Abbreviations

EM electromagnetic.

FD Frequency Domain.

FDTD Finite Difference Time Domain.

FEA / FEM Finite Element Analysis.

MoM Method of Moments.

RF radio frequency.

RxP receiver protection system.

SSRP solid state receiver protector.

TD Time Domain.

TE Transverse Electric.

TEM Transverse Electromagnetic.

TLM Transmission Line Matrix Method.

TM Transverse Magnetic.

UTLM Unstructured Transmission Line Modelling Method.

Chapter 1

Introduction

In this initial chapter, the main aim of this project will be introduced. It will start with a brief presentation of the background behind this research and why modelling a receiver protection system (RxP) is so important (section 1.1). Included in this section is an overview of radio frequency (RF) systems (1.1.1), receiver protection (1.1.2) and waveguides (1.1.3). Then the motivation for carrying out this research, along with a statement of the problems this research aims to solve, will be presented in section 1.2. Finally, an overview of the structure of the thesis (1.3).

1.1 Background

RF systems are ubiquitous in the world around us. With a variety of uses from air traffic control to weather forecasting, satellite navigation to military applications, thus the advancement of this technology is of the utmost importance to the modern world [2, 3, 4]. With many uses across the world of science, including radio astronomy, large scale object detection and nautical uses (including naval fire control, marine navigation and communications [5]), RF systems are widely used and of great importance. The proliferation of modern radar and electronic warfare systems, coupled with the growing requirements to protect sensitive receivers from a broad spectrum of electromagnetic threats, has seen the extension of receiver protection techniques from radar into communications, transponder channels and other transceiver and receiver domains [6]. Understanding fully how these systems operate and how to better to protect them, is critical to the advancement not only of RF systems themselves, but the systems and devices used to protect the receivers, and consequently, the modern world that relies on their function.

1.1.1 RF Systems

One of the more familiar RF systems is RADAR and finds much use in air traffic control and the military. RADAR works by emitting a signal, guided in a specific direction, which propagates away from the receiver. Upon reaching an object, for example a storm cloud, aircraft or ship, the signal wave is scattered, with a finite amount of the signal being reflected back towards the original source, and crucially, the receiver. Once detected at the receiver, the distance and size of the object are calculated using a

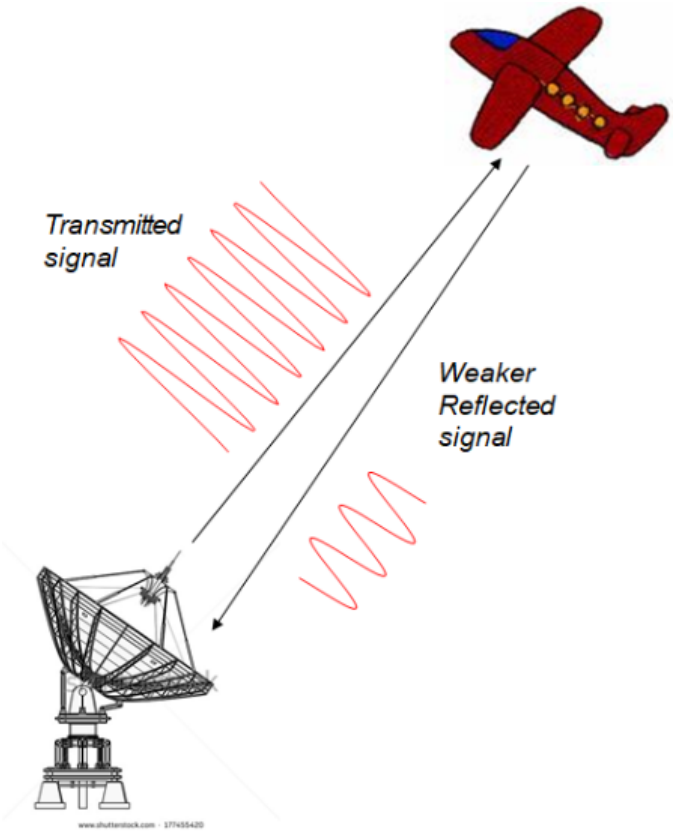

Figure 1.1: A schematic on how a RADAR system works. (Adapted, with permission, from an illustration in the lecture notes for the Analogue Electronics Module [A. Vukovic: H62CET Lecture Notes, 2018])

combination of the strength of the returning signal and the time difference between the initial signal and the received reflection. If the object is moving, these calculations must consider the slight change in the frequency of the signal resulting from the Doppler effect. Figure 1.1 shows the principles of how a RADAR system works.

RF systems typically contain a collection of waveguides, electronic components, receiver protection systems and other junction and filter components. As necessitated by the diminishing strength of the reflected signal with distance from the source, the receiver within RF systems must be highly sensitive. If left unprotected, this high sensitivity leaves them vulnerable to damage or destruction if the power of the incident RF signal is large. The source of these large power signals can simply be reflections

off of nearby large object, such as ships docked adjacent in a port, or other sources, such as the aforementioned ships switching on their own RADAR systems and emitting high power signals. The next subsection will explore some of the more common receiver protection components.

1.1.2 Receiver Protection

Therefore, receiver protection is a critical aspect of designing microwave and radio frequency (RF) systems. The receiver needs to be highly sensitive to detect faint signals reflected off distant objects whilst equally being protected from large incoming RF power [7] e.g. from the high power microwave pulse of a RADAR. These large, incoming signals are not unusual and can occur in mundane situations as simple as ships docked at port - when initiating the vital RADAR system, the proximity of the nearby harbour and ships can cause a powerful reflected pulse incident on the receiver. Consequently, it is imperative that receiver protection devices are installed in front of the receiver to short the system if the incoming signal is large enough to pose a threat to the receiver, to divert the signal, and consequently the power transmitted by the signal wave, away from the sensitive components[8]. The choice of receiver protection depends on the application and frequently it consists of a combination or assembly of components [8].

The original form of a receiver protection device was a gas filled TR (Transmit-Receive) tube and TR limiter [7, 9]. These consisted of tubes or cavities within the waveguide that were filled with a mixture of gases, usually a radioactive element and an electron quenching agent. If the RF power exceeded the threshold level, the free electrons released by the radioactive element were accelerated, creating a gas discharge within

the tube. This discharge formed a short circuit, often causing the tube to glow, and limited power to the receiver [7]. The TR tubes have good power handling, but a relatively low response. Therefore modern systems often incorporate a form of solid state receiver protector (SSRP) that includes a PiN diode connected to the base of an inductive metal post by a series of thin ribbons or wires [6]. The PiN diode in the SSRP allows the bipartite behaviour of the system. In the "Off-State", when the incident signal is appropriately powered, the diode is reverse biased, allowing the signal to pass relatively uninhibited. However, when the incoming wave is too high a voltage, the diode switches to forward bias, allowing the current to pass down the inductive post and create a strong resistance to propagation, effectively shorting the incoming wave.

SSRPs have a faster response than a TR tube and a long operational life without performance degradation [7], but lower peak power capabilities, meaning that the maximum power they can handle is lower than their TR tube counterparts. As a result, SSRPs are often combined with a TR tube "front end" to allow for maximum protection.

The SSRPs found in modern systems can be active, passive, quasi-active, or quasi-passive, depending on their implementation and design [10]. Which of these is most useful depends on the requirements of the final device. Active configurations allow the limiter to be driven as an attenuator, providing Sensitivity Time Control (STC) attenuation in front of the system receiver. This is the process of attenuating (reducing) incident signals for a short period of time to protect the receiver from very strong signals from nearby ground clutter targets, such as animals or insects, atmospheric turbulence or rain to name but a few. This can be used to blank out any very near-range reflections, then progressively reduce the switched attenuation level and limit the magnitude of any near-to-mid range reflected signals [6]. The anatomy of an SSRP will be explored in more detail in

later chapters, but the operation of the device is driven by a PiN diode attached to an inductive post centred in the waveguide (see figure 3.5). Below a threshold voltage, the post remains non-conducting as the diode is forward biased, not affecting the impedance of the waveguide. This is known as the *off-state* and the incident signal wave can propagate unattenuated [11]. However, when the diode becomes forward-biased, it "switches on", an impedance mismatch (when the impedance of the waveguide does not match that of the signal) is caused inside the waveguide by the post becoming conducting and creating a short circuit. The incoming wave is reflected back out of the waveguide, protecting the receiver. The impedance mismatch achieves this by reflecting the signal to create standing waves in front of the discontinuity (in this case the post) which interfere with the incoming signals. The diode switches on when the RF signal increases the voltage across the diode above the threshold voltage. This causes a net injection of carriers into the diodes intrinsic (I) region that is located between the p- and the n- doped layers of the semiconductor. The physics behind semiconductors and their operation will be presented in more detail in chapter 5.

A key part of the developmental process is to be able to accurately model the geometry and response of the waveguides, receiver protection systems and other RF components. Currently, one of the most common techniques is to replace the complex, intricate geometry of the PiN diode with a homogeneous block of predetermined electrical behaviour, making use of the equivalent circuit method often found in systems modelling today. More detail of current modelling methods and techniques ia given later in chapter 6.

Gaining an in depth understanding of how each of the components work, both independently and together in a system is critical to advance the technology behind these devices and to minimising the problems encoun-

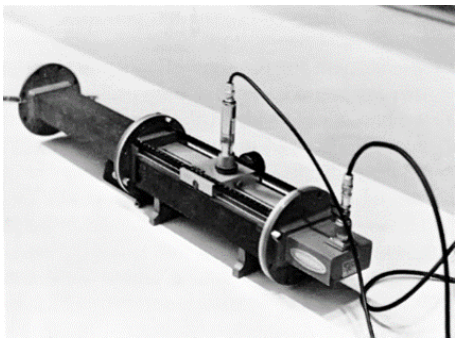

Figure 1.2: An image of a waveguide-receiver set up. The long rectangular tubes that guide the wave to the receiver (waveguides) are clearly visible between the circular flanges. Image taken from Feynman's Lectures in Physics Vol. 2 [12]

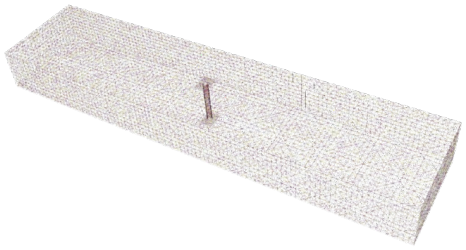

Figure 1.3: An early, simplified mesh of a waveguide with an inductive post included. The flanges have been excluded from the mesh as they bear no electronic purposes, they simply serve as a manner of connecting two adjacent waveguides / components together. [Original work]

tered in the manufacturing stage, not least of which is that each device must be simulated and tested after manufacture owing to the excessive simulation time required by current techniques.

1.1.3 Waveguides

A key component within any RF system is the waveguide. Microwave waveguides are often metallic tubes of various shapes and sizes, typically filled with air or some other dielectric material. At RF frequencies, the hollow metallic tube form of a waveguide is exclusively used. As the name suggests, waveguides are used to guide an incident signal along a path to the receiver or other components within the system. The internal dimensions of a metallic waveguide aperture (shown in figure 1.4) dictate which frequency range and polarisations of electromagnetic waves can propagate through the guide. Figure 1.4 illustrates the key parameters and co-ordinates of a rectangular metallic waveguide. With the origin of the axes placed at the bottom right hand corner of the waveguide aperture, the unit vectors in

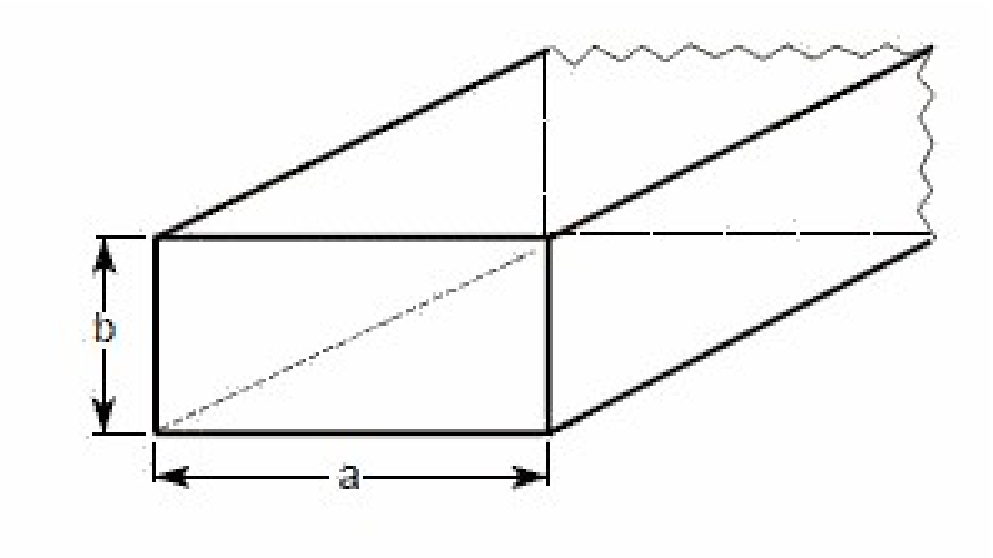

Figure 1.4: A diagram of the key dimensions of the metallic rectangular waveguide. As mentioned, typically the longest dimension, a, lies along the x-axis and the length along the z axis. The quantities a and b are useful for determining the key characteristics of wave propagation through the waveguide (See 2.4.

each of the Cartesian co-ordinates can be seen. The longest dimension of the rectangular waveguide aperture, a, is always placed along the x-axis, with the other key dimension, b, similarly raised along the y-axis. The length of the waveguide is placed along the z-axis.

Similarly, through careful engineering of these internal dimensions of the waveguide, it is possible to limit wave propagation within the waveguide to a single mode (discussed further in section 2.4). Multiple sections of waveguide can be connected together to form the desired path, with sections including obstacles (such as irises, directional filters, inductive posts etc.) frequently inserted to manipulate the signal in some way. Irises are used as filters within the waveguide, limiting the frequency of the wave that can be transmitted. Directional filters, as seen in figure 1.5 are multi-port devices used to both filter the incoming signal and direct the useful signal through a different port, leaving the remaining power to exit the system separately. This is achieved by using a combination of directional couplers (essentially additional parallel waveguides within the system) and

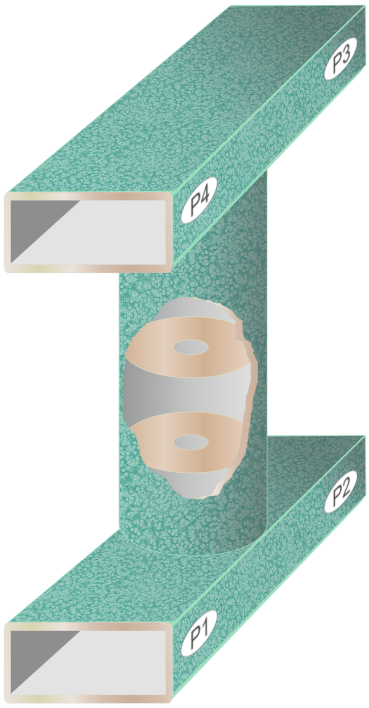

Figure 1.5: An illustration of a 4-port waveguide directional filter. A signal entering the filter through port 1 is filtered, with unwanted signal exiting through port 3 and the remaining power continuing through port 2. Used through creative commons [URL:$https://commons.wikimedia.org/wiki/File:Waveguide_directional_filter.png$]

diplexers (bandpass filters used to separate unwanted signals at a different frequency from wanted signals). In a four port directional filter, one port is always internally terminated, with signal entering port 1 filtered through the diplexer so that unwanted signal exits the system through port 3 and the remaining, desirable power continuing through the system through port 2 [13]. Inductive posts, the obstacle studied most within this research, alone act as a form of filter, but they can also be developed into a protection device with the help of some additional electronic components. This will all be discussed in more detail in section 2.4.

1.2 Motivation for this Research

Computational modelling of modern RF systems, and in particular the response of the receiver protector when exposed to different situations, is a fundamental part of the modern design and manufacture process. The present day modelling of RxP systems faces 3 distinct problems:

1. **Simulations are expensive:**

   With the miniaturisation of modern electronics, detailed models of RxP systems often have 4 orders of magnitude difference in size between the smallest and the largest components. To model these accurately requires large amounts of time, or powerful and expensive computing power.

2. **Small Elements are Replaced:**

   One technique to reduce the requirements is to replace the small elements of the system with an alternative sub-model or circuit (see chapter 6 for more details). Although a useful tool, these alternatives have set behaviour and do not allow detailed analysis of the small element composition, such as the individual layers found in a PiN diode.

3. **Detailed Analysis is Limited:**

   The extended run times and expensive resource requirements mean that simulations with an aim of further understanding the impacts caused by components within the RxP system are often neglected. Instead of allowing the behaviour of the system to be predicted based on previous simulation data, modern manufacture of RxP systems often includes a validation simulation post-manufacture to ensure that the device meets requirements [14]. Producing more suitable and accu-

rate models will allow simulations to become predictive and provide a greater understanding.

With these problems in mind, one aim of this research has been to identify and develop a modelling technique that reduces the resources required to conduct simulations and studies. This will allow more detailed models to evolve which will significantly improve their accuracy and precision, particularly in the diode region. With the reduction in resource requirements, a detailed analysis of the RxP system can be performed, generating a clear picture of how each individual component contributes to the overall operation of the system. A detailed understanding of the system in both the on- and off states, that is the forward-bias and reverse-bias characteristics for the diode, will help to inform future design and fault finding operations, advancing the capabilities of this essential area of modern life.

To allow for the complexity of the problem geometries and the broadband response, time domain numerical modelling methods, such as Finite Difference Time Domain (FDTD) and Transmission Line Matrix Method (TLM) methods [15, 16] are required. Conventional TLM and FDTD methods rely on rectangular meshes and Cartesian co-ordinate systems, which, while useful in large, uniform regions (such as in an empty section of waveguide), result in ultra-fine meshes around curved surfaces and small elements, for example around the inductive post or the connecting ribbons. These ultra-fine meshes significantly increase the computational resources and simulation time required to minimise the discretization and numerical dispersion errors [17]. To overcome this, a time domain TLM method based on a tetrahedral mesh is proposed in [18, 19] to allow arbitrary curved surfaces and complex geometries to be better sampled. This method, known as the unstructured transmission line modelling method (UTLM) along with other, prominent, modelling methods in use today, are

discussed further in chapter 3.

The UTLM software used in this research has been developed at the University of Nottingham by Phil Sewell and Ana Vukovic and is now licensable. The process of simulating electromagnetic wave propagation through a structure is relatively straightforward. Initially, the geometry is coded in C++, using commonly available software such as notepad. This is then passed through the software to create the 3D model. A mesh file is then defined to determine the meshing characteristics of the geometry, including any regions of refinement. The mesh file is combined with the 3D model to complete the unstructured mesh, ready for simulation. Two further files are defined, the simulation file details which boundary conditions and observables are present in the simulation. It also describes the excitation, special feature (such as surface layers) and simulation outputs. The .scl file defines the parameters of the simulation itself, such as the time step size, duration and clustering threshold. The meshed model, .sim file and .scl file are finally combined to run the simulation and produce the desired output files. In this research, the input and output voltages and currents were of most interest, as well as the input and output mode profiles. The voltages and currents were input into a graphical plotting software which allowed calculation of the s-parameters for export and further analysis. The same graphical software provides a visualisation of the current and voltage with time, which allows the minimum required number of time steps to be determined by identifying the point at which these parameters converge to zero and fluctuations cease. Further details of the process can be found in chapter 4.2 or in published literature by Phil and Ana (e.g. [20, 21, 22, 23]).

1.3 Thesis Outline

This thesis principally focusses on developing a comprehensive understanding of an RxP system. To achieve this, thorough investigations have been conducted into each of the constituent parts of the RxP system using the UTLM method and further, more detailed advances in the modelling techniques of specific components have been made. The subsequent thesis is structured as follows: chapters 2 & 3 present the fundamental physics required for a complete understanding of RF systems and RxP devices. Chapter 2 focuses on electromagnetic theory and will introduce Maxwell's equations and wave propagation with particular emphasis on features within the radio frequency band of the EM spectrum. The specifics of waveguides, RF systems and the electronics behind them is also introduced in chapter 2, where topics include wave modes, S-parameters, band structures and cut-off frequencies. Chapter 3 offers a comprehensive review of the more prominent modelling techniques in use today, some of the key results achieved by these techniques in the area of RF systems and other results in literature that are pertinent to this research. The modelling methods themselves will be presented with an overview of how the work, an examination of some of their shortcomings and an indication of some of their successes.

The first significant results are presented in chapter 4. Here, an exploration into the effects of each component within a primitive RxP system are explored. Starting with an empty waveguide, each component of the RxP system is added into the geometry incrementally, with the parameters of each component and their impact on the output of the simulations studied in detail at each stage.

Once a thorough comprehension of the larger components of the RxP system has been established, attention is turned to the smallest and most complex component in the model - the PiN diode. Chapter 5 presents

the physics behind the semiconductors, which drive the response of the diode. An overview of the current modelling techniques for a PiN diode found in literature is presented in chapter 6, including an explanation as to why a new technique is needed and why other models were not selected for use in this project. The model developed in this research is shown in chapter 7. Each stage of the development process is shown in this chapter, starting with a "switching block" - simple block of homogeneous material that is conducting in the on-state and dielectric in the off-state - more detail is added incrementally through 6 distinct stages. The tests, results and analysis, to ensure that the behaviour of the model is appropriate, is displayed in this chapter. Drawing on the results from previous chapters, a full and accurate representation of an RxP system is achieved, with the PiN diode ultimately modelled as 3 distinct layers, allowing the ability to tune the behaviour of the device in incredible detail. Not only are the smallest layers of this device ($\approx 1\mu m$) modelled carefully, but their electronic properties can be altered to reflect differences in the concentration of the dopants, different materials used to dope the layers and the electron/-hole mobilities. This also allows different types of diode (such as GaAs or AlGaAs instead of silicon) to be easily interchanged into the model to explore other performances and opportunities for manufacture, a situation discussed further in chapter 8.

Moreover, an exploration into the response of an RxP system outside of its suggested operating band is documented at the end of chapter 7. These results show that when the incident wave is scattered by the RxP, there is a level of scattering into other modes that can manifest as a loss of power for the signal in the system. If these modes are not considered there is potential for them to propagate through the system, with possible disastrous effects. Any unchecked power transfer is capable of causing damage or interference to the system. Any systems or devices designed to protect

sensitive components need to function in such a way that all hazards are prevented, which is only achievable through comprehension of what these hazards may be.

Chapter 8 shares some final thoughts and possible avenues for future work associated with this project.

The next chapter will discuss Electromagnetic theory, with particular emphasis being placed on RF systems, waveguide theory and Maxwell's Equations.

Chapter 2

The Basic Principles of Electromagnetism, Microwave and Electronic Engineering

This chapter introduces the relevant electromagnetic (EM) theory required to understand the research conducted in this project. Starting with an introduction to Maxwell's equations (2.1.1), this chapter then describes waveguide theory and the propagation of an electromagnetic (EM) wave through a waveguide system (2.4). In section 2.2, the basics of electronic and microwave engineering needed in this research are discussed, before moving on to transmission line theory in section 2.3 and finally microwave analysis (2.5), with additional emphasis on S-parameters, the key form of analysis used in this project 2.5.1).

To properly understand the nature of wave scattering, receiver protection system (RxP), and ultimately the interaction of an electromagnetic (EM) signal with the solid state receiver protector (SSRP), it is necessary to first understand the physics behind electromagnetic (EM) waves, before moving onto the more specific case of wave propagation through a waveguide.

2.1 Electromagnetism

Electromagnetism is the term used to describe everything associated with the electricity and magnetism. These two effects couple to form the fundamental force of nature known as electromagnetism. Both the electric field and magnetic field propagate as components of the same electromagnetic wave, though they appear perpendicular to each other. The electric field is produced by stationary charges, with the magnetic field being produced by moving charges, the behaviour of each is described by Maxwell's equations (see section 2.1.1).

At microwave frequencies, the wave nature of electromagnetic radiation is predominantly observed. Consequently, modern radio frequency (RF) system models consider the propagation of the EM waves through the system of interest and rely on the work of Maxwell to describe how the incident wave will interact with the system of interest.

2.1.1 Maxwell's Equations

The electromagnetic field can be described at any point by Maxwell's equations [12, 24]:

$$\vec{\nabla} \cdot \vec{E} = \frac{\rho}{\epsilon_0} \tag{2.1a}$$

$$\vec{\nabla} \times \vec{E} = \frac{-\partial \vec{B}}{\partial t} \tag{2.1b}$$

$$\vec{\nabla} \cdot \vec{B} = 0 \tag{2.1c}$$

$$c^2 \vec{\nabla} \times \vec{B} = \frac{\partial \vec{E}}{\partial t} + \frac{\vec{j}}{\epsilon_0} \tag{2.1d}$$

where $\vec{E}$ is the electric field at that point in space, $\vec{B}$ is the magnetic field at that point in space, ρ is the electric charge density, the charge per unit volume, $\vec{j}$ is the electric current density.

A quick note on the frequency and wavelength of electromagnetic radiation. Visible light, or the visible spectrum, only comprises a small region in the centre of the full electromagnetic spectrum. Much of the electromagnetic spectrum is invisible to human eyes, and ranges from ionizing radiation such as Gamma rays (γ) to extremely low frequency radio waves.

Photon energy, wavelength and frequency are related through:

$$E = \frac{hc}{\lambda} \tag{2.2}$$

$$= hf \tag{2.3}$$

where c is the speed of light in a vacuum and h is the Planck constant.

The typical frequency range of an radio frequency (RF) system is from around 20kHz to 300 GHz [25]. Within this frequency range, EM radiation exhibits exclusively the wave-type behaviour and the long wavelengths make it ideal for transmitting information of long distances. More-

over, radio technology is based around the emission of electromagnetic waves by electric currents (RF currents) within the RF frequency range.

The common analysis methods in use today are based on one of two processes, either they focus on solving Maxwell's equations or they represent the system as a collective of lumped elements and describe the progress of voltages and currents through the circuit - a process known as circuit theory. The defining factor of which method to use is based on the wavelength of the EM signal being studied. If the wavelength is much bigger than the components, circuit theory is the best choice, however, if the wavelength is comparable to the components, then it is best to use wave theory and solve Maxwell's equations.

2.2 Electronic and Microwave Engineering

Equation 2.1a introduces the concept of permittivity through the inclusion of the ϵ_0 term - the permittivity of free space. Permittivity, ϵ, is the tendency of the electric charges within a material to polarize when exposed to an external electric field. Polarization is the creation of an electric dipole moment - a measure of the separation of the positive and negative charges within a medium - through the distortion of the charge distribution of that material from its normal shape by an external electric field [26]. In other words, when an external electric field is applied across a medium, the permittivity is a measure of how easily the charge distribution inside that material (such as the electron cloud of an atom or molecule) aligns with the applied field and separates into two distinct, opposing poles on either side of the medium:

$$\mathbf{D} = \epsilon\mathbf{E} \tag{2.4}$$

The electric displacement field, **D**, indicates how the charges are distributed in the medium when the electric field, **E** is applied. The permittivity of a medium in general depends on a variety of external factors, such as the parameters of the applied electric field, atmospheric conditions (e.g. temperature and humidity), and cannot be considered constant for the entire medium, rather only at the given point in the medium. It is possible, however, to define a constant permittivity for free space ϵ_0. This is simply the ratio of the displacement field to the applied electric field in free space ($^{\mathbf{D}}/_{\mathbf{E}}$).

For a dielectric medium that is isotropic, it is possible to define the relative permittivity of that material. The relative permittivity, ϵ_r, is a measure of how easily an EM wave can propagate through the medium. The terms relative permittivity and dielectric constant can be used interchangeably. ϵ_0 is the permittivity of free space. Some typical dielectric constants of common materials or materials of interest are shown in table 2.1 below:

2.3 Transmission Lines

Before discussing waveguides in general, including the propagation of an electromagnetic wave through a waveguide, it is first worth considering transmission line theory, one of the key tools in the analysis of RF and microwave systems. Until now, the theory presented in this chapter has either focused on the propagation of waves and fields, as defined by Maxwell's equations, or on the flow of electrons through a circuit by considering the concepts of electronic engineering associated with circuit elements. Transmission line theory bridges the gap between field analysis and basic circuit theory. Transmission line theory draws the analogy between fields propa-

Dielectric Constants, ϵ_r	
Material	$\epsilon_\mathbf{r}$
Ceramic (A-35)	5.60
Fused Quartz	3.78
Gallium Arsenide	13.0
Glass	$5 \sim 10$
Neoprene	6.7
Polytetrafluoroethylene (PTFE)	$1.3 \sim 2.02$
Semiconductor Silicon	12
Teflon	2.1
Titanium Oxide	$86 \sim 133$
Water	80.4

Table 2.1: The dielectric constants of a selection of materials are presented in this table in ascending order. [24, 27, 28].

gating through microwave components and the analogous currents passing through wires. In fact, transmission lines are often depicted schematically as a two-wire line, since transmission lines for transverse electromagnetic wave propagation always have at least two conductors [24].

The distinguishing factor between circuit theory and transmission line theory is electrical size. Comparing the physical size of the network with the electrical wavelength, the domain of circuit theory lies where the dimensions of the network are appreciably smaller than the electrical wavelength. However, transmission lines can be a considerable fraction of a wavelength or many wavelengths in size, allowing transmission line theory to handle significantly larger networks.

Wave propagation on transmission lines can be approached in 2 distinct fashions: an extension of circuit theory or from a specialization of Maxwell's equations. When considering the circuit analysis approach, it is observable that the voltages and currents can vary in magnitude and

phase along the length of the line, meaning that a transmission line is a distributed parameter network. Conversely, in an ordinary circuit the voltage and current do not vary noticeably over the physical dimensions of the lumped elements found in circuit analysis [24]. However, it is possible to model the transmission line as lumped elements through breaking the line down into pieces of infinitesimal length and transforming the general quantities R (series resistance), L (series inductance), G (shunt conductance) and C (shunt capacitance) into per-unit-length quantities. Through careful manipulation, and the use of Kirchoff's voltage and current laws, as seen in chapter 2 of *Microwave Engineering (4th Edition)* by David M. Pozar [24], the time domain forms of the transmission line equations are found to be:

$$\frac{\partial v(z,t)}{\partial z} = -Ri(z,t) - L\frac{\partial i(z,t)}{\partial t} \tag{2.5a}$$

$$\frac{\partial i(z,t)}{\partial z} = -Gv(z,t) - C\frac{\partial v(z,t)}{\partial t} \tag{2.5b}$$

These are also known as the telegrapher's equations. In certain conditions, such as the sinusoidal steady-state condition - where every voltage and current in the system varies sinusoidally with angular frequency ω - with cosine based phasors (the complex number that represents the amplitude and phase of the sinusoidal signal), the telegrapher's equations (2.5) can simplify to:

$$\frac{\partial v(z,t)}{\partial z} = -(R + j\omega L)I(z) \tag{2.6}$$

$$\frac{\partial i(z,t)}{\partial z} = -(G + j\omega C)V(z) \tag{2.7}$$

which bear a striking resemblance in form to Maxwell's curl equations derived in the next section (equations 2.23).

In the previous discussion, the equivalent circuit parameters (L,C,G,R)

were found using circuit theory. In practice, this approach is only truly useful for relatively simple transmission lines and for more complex lines, it is possible to derive the propagation constant, characteristic impedance and attenuation of most transmission lines directly from field theory and Maxwell's equations. This example does illustrate, however, how a transmission line relates to its equivalent circuit model [24].

A waveguide is a canonical example of a transmission line. Rectangular waveguides were one of the earliest types of transmission lines used to transport microwave signals. Despite the trend towards miniaturization and integration, they still find use today in many applications, including high power systems, millimetre wave applications and satellite systems. The next section will consider waveguide theory.

2.4 Waveguide Theory

A fundamental component in microwave technology is the waveguide. As discussed previously (see chapter 1.1.3), waveguides are metallic tubes of a variety of shapes and sizes that facilitate the propagation and manipulation of an incoming EM wave, resulting in detection, signal processing and data transmission. Rectangular waveguides were one of the earliest types of transmission lines used to transmit microwave signals, and they are still used for many applications today. Their usefulness stems from their low-loss transmission of power at high frequencies and their precisely defined EM modes of propagation. [24].

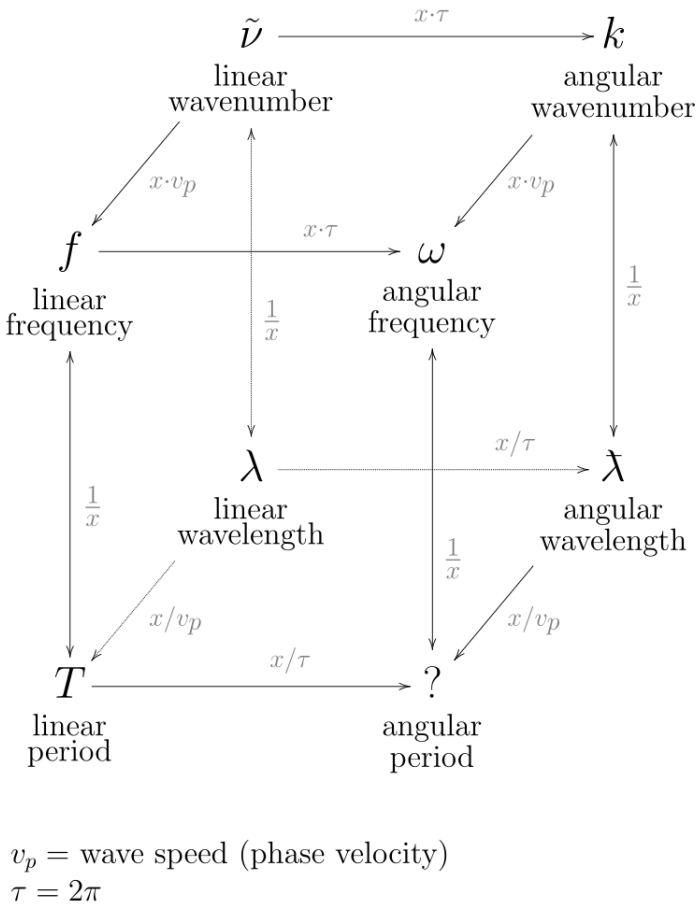

Figure 2.1: A diagram showing the commutative relationship between the harmonic properties of an oscillating wave. In this way, the wave number discussed can be linked to any of the other properties, such as the frequency, by following the mathematical procedure along each arm [29].

2.4.1 Anatomy of a Rectangular Waveguide

Waveguides can be used to confine the incoming wave in one or two dimensions, with the function of the waveguide heavily influencing its geometry. As the wave propagates through the waveguides, it is reflected off the walls, though the signal doesn't travel along the walls, since metal is a near-perfect conductor and the wall is grounded. In order to be transmitted by a waveguide, the frequency of the electromagnetic wave must be above the cut-off frequency of the waveguide. The cut-off frequency is determined by the dimensions and shape of the waveguide. Consider, as is the case throughout

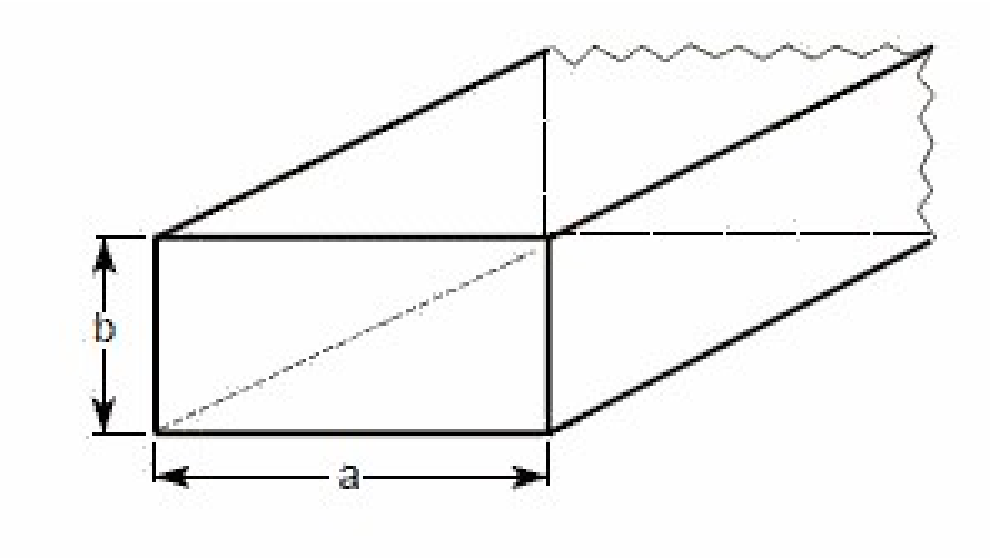

Figure 2.2: A definition of the dimensions of a rectangular waveguide in Cartesian co-ordinates, including the directions of the components of the electric and magnetic fields [30].

this research, a rectangular waveguide, illustrated in figure 1.4 and again in this chapter (figure 2.2). It is standard convention to have the longest side of the waveguide along the x-axis, so that $a > b$. Waves can only propagate along the length of the waveguide, and any electric field within the guide must satisfy Maxwell's equations (eqs (2.1)). Inside the waveguide, only Transverse Electric (TE) and Transverse Magnetic (TM) waves (TM) can propagate, but not Transverse Electromagnetic (TEM) waves since only one conductor (the walls of the waveguide) is present [24].

For rectangular geometries. waves are usually simple harmonic functions of the form $sin(k_x)$[12]. For these waves to propagate down the length of the waveguide, in the z-direction, the field will need to oscillate between positive and negative values along the z-axis, with the oscillations travelling along the guide with velocity, v. If the frequency of the oscillations is ω, the variation of the wave in z may be described by $e^{j(\omega t - k_z z)}$. This

results in the wave in the waveguide being of the form:

$$\mathbf{E_y} = \mathbf{E_0} sin(k_x) e^{j(\omega t - k_z z)} \tag{2.8}$$

where $\mathbf{E_0}$ is the initial strength of the electric field at the source, k_x and k_z are the wave numbers in the x- and z- directions respectively. The wave number is the number of cycles that the wave completes per unit distance, it is a measure of the spatial frequency of the wave. It is related to the frequency of the wave by multiplying by 2π times the phase velocity (discussed in equation (2.15)). The commutative relationship between the properties of a harmonic wave are shown in figure 2.1.

Since the currents and charges in a conductor always adjust themselves so that there is no tangential component of the electric field at the surface of the conductor, to satisfy the field equations, it is necessary for one half a cycle of $sin(k_x x)$ to fit within the width of the waveguide, that is:

$$k_x a = \pi \tag{2.9}$$

Or more generally, for any integer value of π:

$$k_x a = n\pi \tag{2.10}$$

with the width of the waveguide represent by a [12], as shown in figure 2.2.

As there are no charges present inside the waveguide, thus the electric charge density is zero, the divergence of the electric field, $\vec{\nabla} \cdot \vec{E} = 0$, must be zero. This is to satisfy equation (2.1a). Given that the field in this scenario only has a y-component, and it doesn't change with y, this is satisfied.

Finally, in order for the rest of Maxwell's equations to be satisfied, the field must satisfy the wave equation (2.11):

$$\frac{\partial^2 \vec{E_y}}{\partial x^2} + \frac{\partial^2 \vec{E_y}}{\partial y^2} + \frac{\partial^2 \vec{E_y}}{\partial z^2} - \frac{1}{c^2}\frac{\partial^2 \vec{E_y}}{\partial t^2} = 0 \tag{2.11}$$

This becomes:

$$k_x^2 \vec{E_y} + k_z^2 \vec{E_y} - \frac{\omega^2}{c^2} = 0 \tag{2.12}$$

Unless $\mathbf{E_y}$ is zero everywhere, this equation is correct if:

$$k_x^2 + k_z^2 - \frac{\omega^2}{c^2} = 0 \tag{2.13}$$

This leads to a relationship between k_z and the oscillation frequency ω of:

$$k_z = \sqrt{\left(\frac{\omega^2}{c^2}\right) - \left(\frac{\pi^2}{a^2}\right)} \tag{2.14}$$

The wave number, k_z, describes the speed with which nodes of the wave propagate down the waveguide for a given frequency, ω. This is known as the phase velocity, v and is given by:

$$v = \frac{\omega}{k_z} \tag{2.15}$$

Combining this with the wavelength, λ, of a travelling wave:

$$\lambda = \frac{2\pi v}{\omega} \tag{2.16}$$

It can be seen that another definition for k_z is:

$$k_z = \frac{2\pi}{\lambda_g} \tag{2.17}$$

where λ_g is the wavelength of the oscillations along the z-direction, also known as the guide wavelength. By restricting the physical space in which the travelling wave can oscillate, the wavelength of the oscillations has been changed from that of propagation through free-space. As with the wave number, the guide wavelength is also influenced by the dimensions of the waveguide. If the wavelength of a travelling wave through free-space is given by λ_0, then the guide wavelength can be calculated by:

$$\lambda_g = \frac{\lambda_0}{\sqrt{1 - \left(\frac{\lambda_0}{2a}\right)^2}} \tag{2.18}$$

Consequently, the larger the dimensions of the waveguide (in the x-direction), the closer the guide wavelength becomes to that of propagation through free space.

2.4.2 Modes

By carefully considering the dimensions of the waveguide, it is possible to greatly impact the propagation of the travelling wave through the waveguide. Another consequence of these waveguide dimensions is the cut-off frequency of the guide. This is the frequency below which, a travelling wave cannot propagate through the guide. For a rectangular waveguide whose opening is defined by two lengths, a and b, with the longest side a, placed along the x-axis, the cut-off frequency, f_c can be calculated using

the following equation:

$$f_c = \frac{k_c}{2\pi\sqrt{\mu\epsilon}} \tag{2.19}$$

where the cut-off wave number for any given mode is defined as:

$$k_c = \sqrt{\left(\frac{m\pi}{a}\right)^2 + \left(\frac{n\pi}{b}\right)^2} \tag{2.20}$$

where m, n are integers corresponding to the waveguide mode. To get the cut-off frequency of the waveguide itself, we simply need to minimise k_c, by setting m = 1, n = 0, as this relates to the lowest possible mode that will propagate through the guide. The $TE_{00}, TM_{00}, TM_{01}$ and TM_{10} modes would cause the **E-** and **H-**field expressions to become zero and therefore these modes do not exist. The mode with the lowest cut0ff frequency that can propagate is called the dominant mode [24].

For the applications discussed in this thesis, TE Modes are of greater importance than TM Modes, thus they will be now be discussed in more detail. It is worth noting though that due to the close relationship between electricity and magnetism, the constituents of the bipartite electromagnetic wave, the characteristics of TM modes are largely identical to TE modes, so similar calculations can be applied.

TE modes within a waveguide, and transverse electric waves (also referred to as H-waves) more generally, are characterized by fields with $E_z = 0$.

2.4.2.1 General Solutions to Maxwell's Equations for TE and TM Waves

Considering Maxwell's equations (equations (2.1)) and assuming time-harmonic fields with an $e^{j\omega t}$ dependence, propagating along the z-axis, the electric and magnetic fields can be written as:

$$\vec{E}(x,y,z) = [\vec{e}(x,y) + \hat{z}e_z(x,y)]\, e^{-j\beta z} \tag{2.21a}$$

$$\vec{H}(x,y,z) = \left[\vec{h}(x,y) + \hat{z}h_z(x,y)\right] e^{-j\beta z} \tag{2.21b}$$

where $e_z(x,y)$ and $h_z(x,y)$ represent the transverse $(\hat{x},\hat{y})$ electric and magnetic field components. The longitudinal electric and magnetic field components are given by e_z and h_z respectively. The magnetic field intensity, $\vec{H}$, is related to the magnetic field $\vec{B}$ by:

$$\vec{B} = \mu_0\vec{H} \tag{2.22}$$

As usual, μ_0 denotes the permeability of free-space, $\mu_0 = 4\pi \times 10^{-7}$ henry/m.

Inserting the H-field introduced in place of the B-field, Maxwell's equations for a source free transmission line or waveguide simplify to:

$$\nabla \times \vec{E} = -j\omega\mu\vec{H} \tag{2.23a}$$

$$\nabla \times \vec{H} = j\omega\epsilon\vec{E} \tag{2.23b}$$

Using the cut-off wave number, k_c, from above and solving, the four transverse field components in terms of E_z and H_z can be found to be:

Magnetic H-Field:

$$H_x = \frac{j}{k_c^2}\left(\omega\epsilon\frac{\partial E_z}{\partial y} - \beta\frac{\partial H_z}{\partial x}\right) \tag{2.24a}$$

$$H_y = -\frac{j}{k_c^2}\left(\omega\epsilon\frac{\partial E_z}{\partial x} - \beta\frac{\partial H_z}{\partial y}\right) \tag{2.24b}$$

Electric E-Field:

$$E_x = -\frac{j}{k_c^2}\left(\beta\frac{\partial E_z}{\partial x} + \omega\mu\frac{\partial H_z}{\partial y}\right) \tag{2.24c}$$

$$E_y = \frac{j}{k_c^2}\left(\beta\frac{\partial E_z}{\partial y} + \omega\mu\frac{\partial H_z}{\partial x}\right) \tag{2.24d}$$

2.4.2.2 Transverse Electric (TE) Waves and Modes

Transverse electric (TE) waves, also known as H-waves, only have z-components of the H-field ($E_z = 0$, and $H_z \neq 0$). Equations (2.24) simplify to:

$$H_x = \frac{-j\beta}{k_c^2}\frac{\partial H_z}{\partial x} \tag{2.25a}$$

$$H_y = \frac{-j\beta}{k_c^2}\frac{\partial H_z}{\partial y} \tag{2.25b}$$

$$E_x = \frac{-j\omega\mu}{k_c^2}\frac{\partial H_z}{\partial y} \tag{2.25c}$$

$$E_y = \frac{j\omega\mu}{k_c^2}\frac{\partial H_z}{\partial x} \tag{2.25d}$$

Equations (2.24) and (2.25) introduce a factor β known as the propagation constant. For TE and TM waves, the propagation constant is generally a function of the frequency and the geometry of the line or guide when $k_c \neq 0$ [24] and is given by:

$$\beta = \sqrt{k^2 - k_c^2} \tag{2.26}$$

Using the Helmholtz wave equation 2.27 to find H_z and reducing to a two dimensional wave equation for h_z yields:

$$\left(\frac{\partial^2}{\partial x^2} + \frac{\partial^2}{\partial y^2} + \frac{\partial^2}{\partial z^2} + k^2\right) H_z = 0 \tag{2.27}$$

Since $H_z(x, y, z) = h_z(x, y)e^{-j\beta z}$, this reduces to:

$$\left(\frac{\partial^2}{\partial x^2} + \frac{\partial^2}{\partial y^2} + k^2\right) h_z = 0 \tag{2.28}$$

This equation must be solved subject to the boundary conditions of the specific guide geometry [24].

For completeness, from this, the TE wave impedance can be found as:

$$Z_{TE} = \frac{E_x}{H_y} \tag{2.29a}$$

$$= \frac{-E_y}{H_x} \tag{2.29b}$$

$$= \frac{\omega\mu}{\beta} \tag{2.29c}$$

$$= \frac{k\eta}{\beta} \tag{2.29d}$$

where

$$\eta = \sqrt{\frac{\mu}{\epsilon}} \tag{2.29e}$$

which is seen to be frequency dependent. The significance of this is that it shows that TE waves can be supported between two or more conductors as well as inside closed conductors [24].

For a rectangular waveguide, equation (2.27) can be solved using

the standard separation of variables method by letting:

$$h_z(x, y) = X(x)Y(y) \tag{2.30}$$

Which, through substituting into (2.27) leads to:

$$\frac{1}{X}\frac{d^2X}{dx^2} = \frac{1}{Y}\frac{d^2Y}{dy^2} + k_c^2 = 0 \tag{2.31}$$

Following the usual separation of variables arguments:

$$\frac{d^2X}{dx^2} + k_x^2 = 0 \tag{2.32a}$$

$$\frac{d^2Y}{dy^2} + k_y^2 = 0 \tag{2.32b}$$

$$k_x^2 + k_y^2 = 0 \tag{2.32c}$$

The constants k_x, k_y are introduced because each of the terms in (2.31) must be equal to a constant.

The transverse field components of any TE mode can be found by using equations (2.25) and a solution for H_z. Following the derivation found in chapter 3 of Microwave Engineering by Pozar [24], the general solution for h_z can be written, introducing the constants from above (2.32), as:

$$h_z(x, y) = [Acos(k_x x) + Bsin(k_x x)][Ccos(k_y y) + Dsin(k_y y)] \tag{2.33}$$

Introducing the boundary conditions imposed by the waveguide geometry (fig. 2.2) on the electric field components tangential to the waveguide walls, namely:

$$e_x(x, y) = 0 \qquad \text{at } y = 0, b \tag{2.34a}$$

$$e_y(x, y) = 0 \qquad \text{at } x = 0, a \tag{2.34b}$$

Since these boundary conditions do not explicitly apply to h_z, it is imperative to calculate e_x and e_y from h_z using equations (2.25c & d) to find:

$$e_x = \frac{-j\omega\mu}{k_c^2} k_y [A cos(k_x x) + B sin(k_x x)][-C cos(k_y y) + D sin(k_y y)] \quad (2.35a)$$

$$e_y = \frac{-j\omega\mu}{k_c^2} k_x [-A cos(k_x x) + B sin(k_x x)][C cos(k_y y) + D sin(k_y y)] \quad (2.35b)$$

Next, imposing the boundary conditions (2.34), yields:

$$D = 0 \qquad k_y = \frac{n\pi}{b} \qquad for n = 0, 1, 2... \quad (2.36a)$$

$$B = 0 \qquad k_x = \frac{m\pi}{a} \qquad for m = 0, 1, 2... \quad (2.36b)$$

The final solution for H_z is then:

$$H_z(x, y, z) = A_{m,n} cos\left(\frac{m\pi x}{a}\right) cos\left(\frac{n\pi y}{b}\right) e^{-j\beta z} \quad (2.37)$$

Which, when combined with equations (2.25) yields the transverse field components of the $TE_{m,n}$ modes:

$$E_x = \frac{j\omega\mu n\pi}{k_c^2 b} A_{m,n} cos\left(\frac{m\pi x}{a}\right) sin\left(\frac{n\pi y}{b}\right) e^{-j\beta z} \quad (2.38a)$$

$$E_y = \frac{-j\omega\mu m\pi}{k_c^2 a} A_{m,n} sin\left(\frac{m\pi x}{a}\right) cos\left(\frac{n\pi y}{b}\right) e^{-j\beta z} \quad (2.38b)$$

$$H_x = \frac{j\beta m\pi}{k_c^2 a} A_{m,n} sin\left(\frac{m\pi x}{a}\right) cos\left(\frac{n\pi y}{b}\right) e^{-j\beta z} \quad (2.38c)$$

$$H_y = \frac{j\beta n\pi}{k_c^2 b} A_{m,n} cos\left(\frac{m\pi x}{a}\right) sin\left(\frac{n\pi y}{b}\right) e^{-j\beta z} \quad (2.38d)$$

As above, the propagation constant, β is given by:

$$\beta = \sqrt{k^2 - k_c^2} \quad (2.39a)$$

$$= \sqrt{k^2 - \left(\frac{m\pi}{a}\right)^2 - \left(\frac{n\pi}{b}\right)^2} \quad (2.39b)$$

Which is real, and therefore corresponds to a propagating mode, when:

$$k > k_c = \sqrt{\left(\frac{m\pi}{a}\right)^2 + \left(\frac{n\pi}{b}\right)^2} \tag{2.39c}$$

The cutoff frequency for each mode, $f_{c_{m,n}}$, that is each combination of m and n, is calculated using equation (2.19) above. The dominant TE mode in a rectangular waveguide is the TE_{10} mode.

For a mode to propagate through the waveguide, the cutoff frequency of that mode must be above the operating frequency, f. Otherwise, the propagation constant is imaginary, and all field components will decay exponentially away from the source of excitation [24]. Modes whose cutoff frequency are below the frequency of operation are referred to as evanescent or cutoff modes and decay exponentially away from the source.

Typically, the dimensions of the waveguide and the operating frequency are chosen so that only the dominant TE_{10} mode can propagate. However, it is possible, if the choice of operating frequency or guide dimensions are not made appropriately, that more than one mode may propagate through the guide at a given time. In this case, the guide is said to be overmoded[24]. An overmoded waveguide is not necessarily detrimental, often oversized, and therefore overmoded, waveguides are used for high RF power transfer in the X-Band. However, great care must be taken to ensure that losses due to parasitic mode coupling are minimised or avoided [31].

2.4.2.3 Transverse Magnetic (TM) Waves and Modes

The process for finding the wave impedance and 2D wave equation for Transverse Magnetic (TM) waves is broadly similar to that of TE waves. TM waves, also known as E-Waves, are characterized by $E_z \neq 0$, and $H_z = 0$. As before, it is possible to reduce the x- and y- components of the

electric and magnetic fields to:

$$H_x = \frac{j\omega\epsilon}{k_c^2}\frac{\partial E_z}{\partial y} \tag{2.40a}$$

$$H_y = \frac{-j\omega\epsilon}{k_c^2}\frac{\partial E_z}{\partial x} \tag{2.40b}$$

$$E_x = \frac{-j\beta}{k_c^2}\frac{\partial E_z}{\partial x} \tag{2.40c}$$

$$E_y = \frac{-j\beta}{k_c^2}\frac{\partial E_z}{\partial y} \tag{2.40d}$$

Again, as in the TE case, $k_c \neq 0$ and the propagation constant $\beta = \sqrt{k^2 - k_c^2}$ is a function of the frequency and the geometry of the guide or line. The Helmholtz wave equation is once more used to find E_z:

$$\left(\frac{\partial^2}{\partial x^2} + \frac{\partial^2}{\partial y^2} + \frac{\partial^2}{\partial z^2} + k^2\right) E_z = 0 \tag{2.41}$$

Since $E_z(x, y, z) = e_z(x, y)e^{-j\beta z}$, this reduces to:

$$\left(\frac{\partial^2}{\partial x^2} + \frac{\partial^2}{\partial y^2} + k^2\right) e_z = 0 \tag{2.42}$$

TM waves can also be supported inside closed conductors as well as between two or more conductors, with the TM wave impedance found by:

$$Z_{TM} = \frac{E_x}{H_y} \tag{2.43a}$$

$$= \frac{-E_y}{H_x} \tag{2.43b}$$

$$= \frac{\beta}{\omega\epsilon} \tag{2.43c}$$

$$= \frac{\beta\eta}{k} \tag{2.43d}$$

Implementing the boundary conditions introduced by propagation through a rectangular waveguide, it is possible to compute the transverse field components for the TM_{mn} modes. Following the derivation found in Microwave

Engineering [24] once more, the separation of variables technique, outlined above for TE modes, is used to find that the general solution for e_z that satisfies the reduced wave equation (2.41) has the form:

$$e_z(x,y) = [Acos(k_x x) + Bsin(k_x x)]\,[Ccos(k_y y) + Dsin(k_y y)] \tag{2.44}$$

In this case, the boundary conditions imposed by the waveguide can be applied directly to e_z:

$$e_z(x,y) = 0 \qquad \text{at } x = 0, a \tag{2.45a}$$

$$e_z(x,y) = 0 \qquad \text{at } y = 0, b \tag{2.45b}$$

Satisfying these boundary conditions for e_z will also lead to them being satisfied for e_x and e_y. Applying the boundary conditions (2.45) shows that:

$$A = 0 \qquad k_x = \frac{m\pi}{a} \qquad for n = 0, 1, 2... \tag{2.46a}$$

$$C = 0 \qquad k_y = \frac{n\pi}{b} \qquad for m = 0, 1, 2... \tag{2.46b}$$

Reducing the solution of E_z to:

$$E_z(x,y,z) = B_{m,n} sin\left(\frac{m\pi x}{a}\right) sin\left(\frac{n\pi y}{b}\right) e^{-j\beta z} \tag{2.47}$$

Which, when combined with equations (2.25) yields the transverse field components of the $TM_{m,n}$ modes:

$$E_x = \frac{-j\beta m\pi}{ak_c^2} B_{m,n} cos\left(\frac{m\pi x}{a}\right) sin\left(\frac{n\pi y}{b}\right) e^{-j\beta z} \tag{2.48a}$$

$$E_y = \frac{-j\beta n\pi}{bk_c^2} B_{m,n} sin\left(\frac{m\pi x}{a}\right) cos\left(\frac{n\pi y}{b}\right) e^{-j\beta z} \tag{2.48b}$$

$$H_x = \frac{j\omega\epsilon n\pi}{bk_c^2} B_{m,n} sin\left(\frac{m\pi x}{a}\right) cos\left(\frac{n\pi y}{b}\right) e^{-j\beta z} \tag{2.48c}$$

$$H_y = \frac{-j\omega\epsilon m\pi}{ak_c^2} B_{m,n} cos\left(\frac{m\pi x}{a}\right) sin\left(\frac{n\pi y}{b}\right) e^{-j\beta z} \tag{2.48d}$$

The propagation constant and cutoff frequencies are calculated in the same manner for TM modes as for TE modes, though the lowest order TM mode that can propagate is the TM_{11} mode.

2.4.2.4 Mode Calculations

When designing an RF system that uses waveguide for a specific application, equations 2.19 and 2.20 above can inform the key aspects of the design. Through careful consideration of the above equations, the waveguide can be made in such a way that only one chosen TE-mode can propagate through the system. This is achieved by ensuring that the dimensions of the waveguide are such that the cut-off frequency of the desired mode is above the minimum frequency allowed by the guide, but that the operating band of the guide is below the cut-off frequency of the next mode.

Knowledge of the cutoff frequencies of other TE and TM modes within the RF system can be imperative in the analysis. Although careful design can ensure that only one mode propagates into the waveguide, scattering caused by discontinuities may result in other modes becoming present in the system. Awareness of the cutoff frequency of these modes, in addition to those of the evanescent modes, can facilitate a deeper com-

f_c, TE Modes		n										
		0	**1**	**2**	**3**	**4**	**5**	**6**	**7**	**8**	**9**	**10**
m	**0**	0.00	14.754	29.507	44.261	59.015	73.769	88.522	103.276	118.030	132.784	147.537
	1	6.557	16.145	30.227	44.744	59.378	74.060	88.765	103.484	118.212	132.945	147.683
	2	13.114	19.740	32.291	46.163	60.455	74.925	89.489	104.105	118.756	133.430	148.119
	3	19.672	24.590	35.464	48.436	62.207	76.347	90.682	105.133	119.658	134.233	148.843
	4	26.229	30.093	39.480	51.449	64.581	78.293	92.326	106.555	120.909	135.349	149.851
	5	32.786	35.953	44.109	55.082	67.511	80.726	94.399	108.355	122.499	136.771	151.136
	6	39.343	42.019	49.179	59.219	70.927	83.604	96.872	110.516	124.414	138.490	152.693
	7	45.901	48.213	54.567	63.764	74.764	86.883	99.715	113.017	126.641	140.493	154.512
	8	52.458	54.493	60.187	68.636	78.959	90.519	102.898	115.835	129.162	142.770	156.586
	9	59.015	60.831	65.981	73.769	83.460	94.470	106.391	118.948	131.961	145.307	158.903
	10	65.572	67.211	71.905	79.112	88.218	98.699	110.163	122.334	135.021	148.092	161.453

Table 2.2: The cut-off frequencies of the first 121 TE-Modes for a rectangular waveguide, given in GHz. Although only one mode can propagate through a well designed waveguide, if scattering occurs within the system, it is possible for other modes to be excited, therefore knowing their cutoff frequencies can be advantageous in understanding what effects the scattering is having.

prehension of the data, since one explanation for artefacts observed at these frequencies could be scattering into these modes. Table 2.2 presents the cutoff frequency for the first 120 TE modes for the rectangular WG16 waveguide modelled in this research.

Power loss within the system is of significant concern. One way in which power may be perceived as lost is if it is scattered into another mode, one that is not being observed in the output plane. A clear identifier of this is if the power is observed to drop sharply around the cutoff frequency of another mode, something illuminated by the cutoff frequencies tabulated above. A further consequence of scattering into other modes is the potential for the guide to become overmoded, that is to have more than one mode propagating through. This can lead to power loss due to attenuation, which needs to be identified in order to be corrected in future applications.

2.4.3 Attenuation

In many practical applications, perfect conductors are difficult to achieve, but with careful consideration and engineering, good conductors may be adequate for the application. Attenuation is present in good conductors, with most metals categorized as good conductors. A good conductor is one where the conductive current is much greater than the displacement

current, i.e. $\sigma >> \omega\epsilon$. [24] In a good conductor, the attenuation, skin depth and complex propagation constant are all linked.

The complex propagation constant (γ) for a medium is a complex term that describes the propagation of a wave through a medium. For the general plane wave solution, it is made up of two parts, the attenuation constant, α that describes the decrease in the magnitude of the field as it passes through the medium, and the phase constant, β:

$$\gamma = \alpha + j\beta \tag{2.49}$$

$$= j\omega\sqrt{\mu\epsilon}\sqrt{1 - j\frac{\sigma}{\omega\epsilon}} \tag{2.50}$$

where the complex permeability of the medium is written as μ, ϵ defines the complex permittivity of the medium, ω is the frequency, and σ is the conductivity of the medium. Considering the main focus of this research, propagation through a waveguide (along a transmission line), this becomes [32]:

$$\gamma = \sqrt{k_c^2 - k^2} \tag{2.51}$$

From this general form, it is possible to extract the (non-complex) propagation constant for TE modes found in equations 2.39 above. Similarly, the intrinsic impedance of the medium, η, can be defined from the propagation constant as:

$$\eta = \frac{\omega\mu}{k} \tag{2.52}$$

$$= \sqrt{\frac{\mu}{\epsilon}} \tag{2.53}$$

The ratio of the $\vec{E}$ and $\vec{H}$ field components is known as the wave impedance, and, for a plane wave is equal to the intrinsic impedance of the medium.

In free-space, the intrinsic impedance is:

$$\eta_0 = \sqrt{\frac{\mu_0}{\epsilon_0}} \tag{2.54}$$

$$= 377\Omega \tag{2.55}$$

As previously mentioned, the attenuation is a measure of the reduction in output power of the wave as it passes through a medium. This attenuation can be caused by a number of factors, including the intrinsic impedance of the medium, losses within the system itself, or some form of dielectric. For a plane wave travelling through a good conductor, the attenuation constant can be written as:

$$\alpha = Re\{\gamma\} \tag{2.56}$$

$$= \sqrt{\frac{\omega\mu\sigma}{2}} \tag{2.57}$$

2.5 Microwave Analysis

Until now, the discussion of wave propagation has been centred around an empty waveguide, through which the signal can pass relatively uninhibited. Although useful for transmitting electromagnetic signals to the receiver, empty waveguides alone are limited in their uses. The true diversity in their usefulness, and a contributing factor to their longevity and continued use today, is the diverse array of applications that can be achieved using a waveguide and a selection of inserted obstacles. As previously discussed, irises, filters, and inductive post are all well used examples of such obstacles, but in order to study their effectiveness, it is important to consider how the incident signal is reflected, transmitted and perturbed when it encounters an obstacle.

Microwave Network analysis intends to extend the basic circuit and network concepts from low frequency analysis to handle many microwave analysis and design problems. The main reason for doing this is that it is far simpler to apply the simple and intuitive ideas of circuit analysis to a microwave problem than it is to solve Maxwell's equations for the same problem. Solving Maxwell's equations gives details of the electromagnetic field at all points in space, which often is too much information as the main considerations are of the voltage or current at a set of terminals, the power flow through a device, or some other property that is evaluated at either end of the system - a "terminal" quantity [24]. Microwave network analysis provides a number of useful techniques for understanding the behaviour of an EM wave and it's interaction with obstacles within the RF system. These include:

- **Admittance matrices** - relate the voltages and currents of an n-port microwave network using matrix representation. Each port in the network relates to any type of transmission line or transmission line equivalent of a single propagating waveguide mode. An admittance matrix in an $n \times n$ matrix that links the current to the voltage of the network in matrix form as $[I] = [Y][V]$ with each element of the Y matrix found to be:

$$Y_{i,j} = \left.\frac{I_i}{V_j}\right|_{V_k = 0 \text{ for } k \neq j} \tag{2.58}$$

  Any element $Y_{i,j}$ can be determined by driving port j with voltage V_j, short circuiting all other ports and measuring the short-circuited current at port i [24].

- **Impedance matrices** - Similarly to admittance matrices, these relate the voltages and currents of an n-port microwave network using

matrix representation in the form $[V] = [Z]\,[I]$, with each element of the Z matrix ($Z_{i,j}$) found by driving port j with the current I_j, open-circuiting all other ports and measuring the open-circuit voltage at port i:

$$Z_{i,j} = \left.\frac{V_i}{I_j}\right|_{I_k = 0 \text{ for } k \neq j} \tag{2.59}$$

The admittance and impedance matrices are inverses of each other [24].

- **Scattering matrices** - For an N-port network, the scattering matrix gives complete representation of the network as seen at its N ports. Unlike impedance or admittance matrices, the scattering matrix describes the network in terms of reflected and transmitted waves, instead of voltages and currents. It achieves this by relating the voltage waves incident on the ports to those reflected from the ports. For some components and circuits, a vector network analyzer (VNA) can be used to measure the scattering parameters directly, whereas for others they need to be calculated using network analysis techniques. In matrix form, the scattering matrix is represented as $[V^-] = [S]\,[V^+]$. The amplitude of the voltage incident on port n is given by V_n^+, with the amplitude of the voltage wave reflected from the same port being given by V_n^-. thus each component of the scattering matrix is given by:

$$S_{i,j} = \left.\frac{V_i^-}{V_j^+}\right|_{V_k^+ = 0 \text{ for } k \neq j} \tag{2.60}$$

Therefore, the scattering element $S_{i,j}$ is found by driving port j with an incident wave of voltage V_j^+ and measuring the reflected wave amplitude V_i^- coming out of port i. All ports except the jth port

should be terminated with matched loads to avoid reflections and therefore have incident waves set to zero [24].

- **Transmission (ABCD) matrices** - In practice many microwave networks are a cascade connection of two or more two-port networks, allowing the definition of a 2×2 transmission (or ABCD) matrix for each two port network. In terms of the total voltages and currents, the ABCD matrix of a 2 port network is defined as follows:

$$V_1 = AV_2 + BI_2 \tag{2.61}$$

$$I_1 = CV_2 + DI_2 \tag{2.62}$$

or in matrix form as :

$$\begin{bmatrix} V_1 \\ I_1 \end{bmatrix} = \begin{bmatrix} A & B \\ C & D \end{bmatrix} \begin{bmatrix} V_2 \\ I_2 \end{bmatrix} \tag{2.63}$$

The usefulness of the ABCD representation lies in the library of ABCD matrices for elementary two-port networks that can be built up. This library allows more complicated networks to be analysed by cascading the different ABCD matrix representations of the components in the network and using matrix algebra to find the solution to the problem. [24]

Care must be taken to ensure that this form of analysis is appropriate, since in some situations, circuit analysis techniques would be an oversimplification and there would be a necessity to resort to field analysis techniques. For a rectangular waveguide, circuit theory is applicable and the effects of the introduction of obstacles within the waveguide are easily distinguishable when considering the s-parameters of the system, which are derived

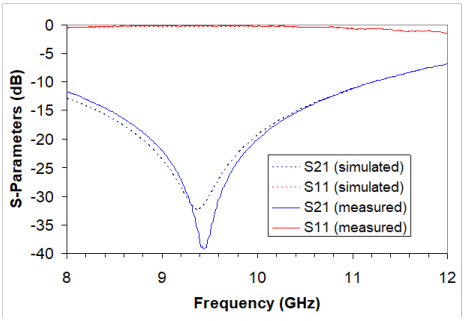

(a) Region of reflection illustrated by S_{11} (the reflection coefficient) being a maximum ($\approx 0dB$) and S_{21} being a minimum, with the peak reflection occurring at around 9.4 GHz, where the insertion loss is $\approx 0.01\%$ of the peak power.

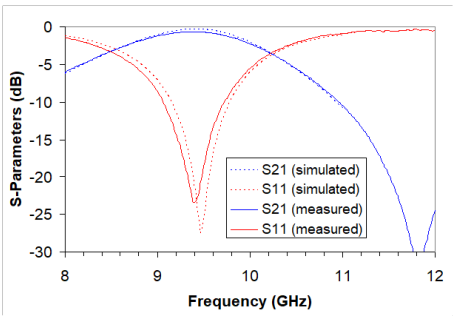

(b) A region of transmission can be observed in the frequency range $\approx 8.8 - 10.2$ GHz. This is illustrated by S_{21} (the transmission coefficient) being a maximum ($\leq -3dB$) and S_{11} being a minimum, with the peak transmission occurring at around 9.4 GHz, where the return loss is $\approx 0.5\%$ of the peak power.

Figure 2.3: Two simple graphs showing regions of reflection and transmission respectively. Taken from the work of Farrington et al. [6], these figures present both the simulated and measured in band response from an RxP system. In their work, Farrington et al. use the common nomenclature of referring to the insertion loss as S_{21} and the return loss as S_{11}. As the system is designed to do, the peak reflection observed in figure 2.3a occurs when the diode is in the on-state, protecting the receiver, and the region of transmission observed in figure 2.3b corresponding to the off-state of the diode, allowing the signal to pass through to the receiver uninhibited.

from the scattering matrix.

2.5.1 S-Parameters

The abbreviation S in the term S-parameters has been derived from the word scattering [33], owing to the fact that the S-parameters are derived from the scattering matrix mentioned above. Put simply, the s-parameters describe how the incident voltage wave is "scattered" (that is reflection and transmission of the wave) by any discontinuity, junction or object within the RF network. For high frequencies, it is often beneficial to consider power waves or voltage waves, rather than voltages or currents, which facilitates the use of circuit theory to solve electromagnetic wave propagation problems. The s-parameters allow a relation to be seen between the power of the wave travelling towards the port and the power of the wave travelling away from the port [33].

The scattering matrix itself and the s-parameters can provide a lot of useful information simply from inspection. For example, a network that is lossless (that is no power is lost or dissipated as the wave travels through the network) if its scattering matrix is unitary, i.e.$[S]\,[S^*]^T = [U]$ [24, 33]. More specifically, for a two port network with the scattering matrix:

$$[S] = \begin{bmatrix} S_{11} & S_{12} \\ S_{21} & S_{22} \end{bmatrix} \tag{2.64}$$

the following generic descriptions are true:

- S_{11} is the input port voltage reflection coefficient (the amount of power that has been reflected back out of port 1 after having entered port 1)
- S_{12} is the reverse voltage gain - that is the ratio of the voltage that exited port 1 after entering port 2
- S_{21} is the forward voltage gain - the ratio of voltage exiting port 2 after entering port 1, i.e. the transmitted power
- S_{22} is the output port voltage reflection coefficient (the amount of power that has been reflected back out of port 2 after having entered port 2)

Furthermore, for power entering the system is conserved (i.e. the system is lossless) if:

$$|S_{11}|^2 + |S_{21}|^2 = 1 \tag{2.65a}$$

$$|S_{12}|^2 + |S_{22}|^2 = 1 \tag{2.65b}$$

$$S_{11}^* S_{12} + S_{21}^* S_{22} = 0 \tag{2.65c}$$

though it is quite common to split the network in such a manner that the wave only enters through one port, simplifying the problem significantly.

If the 2 port network is only excited in one direction, as is often the case in many waveguide applications, it is possible to define 2 useful quantities, the reflection and transmission coefficients, also known as the insertion loss and return loss.

Insertion loss results from the insertion of a device in a transmission line, most commonly in this research the inductive post and ultimately the SSRPs and is defined as the reduction in signal power caused by this. It is a ratio of the signal level with and without the insertion of the device.[24, 34] Return loss is the loss in power of the signal returned or reflected by a discontinuity in the transmission line (again the inductive post or SSRP)[35].

The insertion and return losses, measured in Decibels (dB) are calculated by [24, 34],

$$\text{Insertion Loss} = -20log_{10}(|S_{21}|) \tag{2.66}$$

$$\text{(Input) Return Loss} = -20log_{10}(|S_{11}|) \tag{2.67}$$

Somewhat confusingly, these losses are commonly presented as the negative of the quantities above, however, strictly speaking, owing to the definition of loss, this is incorrect [36].

A more useful representation of the insertion and return losses is to plot them graphically. By definition (see 2.65), the maxima and minima of these quantities must oppose each other. Figures 2.3a and 2.3b show the two conditions of reflection and transmission for an X-band receiver protector respectively. In figure 2.3a, the return loss can be seen to be at a maximum (approximately 0 dB) in the centre of the band, whilst the insertions loss is at a minimum. This illustrates a region of total reflection, that the incident voltage wave is being reflected back to the source, either

by some obstacle or a mismatched terminal.

Conversely, a region of complete transmission occurs when the insertion loss is at a maximum and the return loss is at a minimum (as shown in figure 2.3b). Rather confusingly, even though the signal is transmitted unhindered through this region of the network, the term "loss" is still used to describe the transmission owing to the fact that the power is "lost" out of the opposite port, i.e. it enters through port 1 but is "lost" (transmitted) out of port 2.

As consequence of the insertion loss depending solely on S_{21} and the return loss depending solely on S_{11}, it is not uncommon in RF engineering for abbreviations to be made.

In the next chapter, the modelling methods that are prominently in ue to model waveguides and RF systems are presented. The chapter starts with an overview of modelling RF systems in general, before selecting some of the more common methods and introducing their key features and weaknesses, including a presentation of Unstructured Transmission Line Modelling Method (UTLM), the method used for this research. After this, some of the key simulation results from literature are discussed before an analytical model of a post discontinuity within a waveguide is derived.

Chapter 3

Modelling Microwave Waveguides and RxP Components

This chapter will explore the techniques in use today for modelling the transmission of EM waves through different structures, with particular emphasis on modelling the propagation of EM waves through a rectangular waveguide. This chapter will start with an overview of why modelling is required and an introduction to some of the fundamental differences between modelling methods (see section 3.1). In section 3.2, a spotlight is shone on some of the more common methods, illustrating some of the relevant key works, strengths and weaknesses of the model and which applications it is most applicable to. The Unstructured Transmission Line Modelling Method (UTLM) is introduced in section 3.3, the primary method used in this research and an advancement on the more common Transmission Line Matrix Method (TLM) method. In this section, the theory behind UTLM will be explained, before an explanation of the process of implementing

UTLM to simulate geometries is provided. Finally, a derivation of the analytical model for wave propagation through a) an empty waveguide and b) a waveguide with a post discontinuity is provided in section 3.5.

3.1 Overview

In scientific and technical fields, where a detailed quantitative response is required, models need to be detailed to account for a multitude of inputs, and to develop detailed quantitative results. In the field of electromagnetics, these models are often analytical, e.g. Ohm's law relating potential difference and current across a resistor, or Maxwell's equations detailing electromagnetic fields and their propagation, and may reside in algorithms embedded in computer software [16].

Maxwell's equations (see equations 2.1) are an excellent tool for describing the electromagnetic field at any point in space. However, calculating the field at every point in space for a propagating wave, even within a restricted domain such as a waveguide, commonly proves impractical and unwieldy. The resources and time required to perform these calculations are prohibitive. For this reason it is often sensible to use approximations and generate models that accurately describe the system and phenomena that are to be studied. A variety of numerical techniques are employed within the discipline of modelling RF systems which are conventionally classified according to the domain of the operator and the variable. In modelling electromagnetic wave propagation, the variables are commonly either in the Time Domain (TD) or Frequency Domain (FD). Methods that use Frequency Domain (FD) operators, such as the Method of Moments (MoM), are better suited to problems involving steady-state narrow band applications. Alternatively, if the problem is non-linear in nature or has

wide-band applications, employing a technique that operates in the Time Domain (TD), such as Transmission Line Matrix Method (TLM) or the Finite Difference Time Domain (FDTD) is preferable [16].

Each of the domains, Time Domain (TD) and Frequency Domain (FD), contribute significantly to the solving of electromagnetic wave propagation problems, with full wave analysis present in most methods in each domain. Although powerful, great care needs to be taken when interpreting the results of numerical methods to ensure that their outputs correspond to the real physics of the problem [37]. Section 3.2 below describes some of the more common methods employed in solving electromagnetic problems today, highlighting some of their strengths and weaknesses alongside a presentation of some relevant works where the method has been successfully applied.

3.2 Common EM Modelling Techniques

As mentioned above, the numerical methods used to solve these problems can broadly be divided into the Time Domain (TD) and the Frequency Domain (FD). This section, will focus on 4 of the more common techniques in use today, 2 from each domain. Method of Moments (MoM) and Finite Element Analysis (FEA / FEM) each operate in the frequency domain, with FEA in particular demonstrating a promising transitional implementation of a method commonly used in solving problems in other fields, such as materials engineering. The Time Domain (TD) methods of Finite Difference Time Domain (FDTD) and Transmission Line Matrix Method (TLM) both use a cubic discretization of the problem space to illustrate the propagation of the EM field through the problem space with time. Indeed, one commonality across all of the methods discussed in this section is the discretization

of the problem space using a grid or 3D mesh. This allows the fields to be calculated at a multitude of points within the geometry simultaneously, with the resolution of the field being determined by the density of points described by the mesh. Time domain techniques are considered to have the highest suitability for most waveguide analysis, but success has also been achieved using frequency domain techniques for certain problems.

3.2.1 Method of Moments (MoM)

The Method of Moments (MoM) is one of the most powerful techniques in the frequency domain [38]. It is a technique that attempts to solve complex integral equations by reducing them to a system of linear equations and applying weighted residuals (method of moments). Primarily, an integral equation is obtained for the problem using Green's functions, before the MoM is applied. This technique begins by establishing a set of trial solutions with one or more variable parameters and using a best fit algorithm to minimise the residuals, the measure of the difference between the trial and true solutions. MoM techniques are often applied to problems that include conductors only, homogeneous dielectrics only or some very specific configurations that combine both materials, dictated by the form of the integral equation. MoM techniques are particularly efficient at modelling wire antennae or wires attached to large conductive surfaces, but this efficiency breaks down when complex geometries or inhomogeneous dielectrics are included within the configuration.

Although MoM techniques do an excellent job of analysing a variety of three-dimensional radiation and scattering problems, some of the major limitations in the Method of Moments (MoM) techniques include diffraction effects and that the discretization of the problem space to obtain the

solutions in an MoM technique frequently require a large number of segments to be involved [37].

Despite these limitations, MoM techniques have successfully been applied to solve some waveguide problems. In 2011, Lai et al. [39] used an MoM technique to analyse the edge slot array for a rectangular waveguide with finite wall thickness. Using this technique, they were able to efficiently analyse the interior region of the system, finding the equivalent magnetic and electric currents, and accurately model the slot cavity region and waveguide exterior when excited at 10GHz. Similarly, by combining MoM with mode-matching (MM) - where the electric field distributions are matched to waveguide modes, Aydogan et al. [40], studied dielectric discontinuities within a rectangular waveguide. These discontinuities formed an inhomogeneous structure across the width (x-direction) and longitudinal length (z-direction) of the waveguide. The hybrid method outlined in the paper provides an accurate and fast method for the frequency of E-Plane type dielectric loaded metallic waveguides. Although very efficient for cuboidal structures, the author does note that the method is less competent for structures that are more curved in nature.

Another hybridisation of MoM is with FEA/FEM methods, particularly in antenna applications. One relevant example of this hybridisation to waveguides is the work of Sangster et al. [41], which uses a hybrid MoM/FEA technique to analyse the coupling and radiating apertures in a rectangular waveguide. An advantage of this approach is that it ensures the convergence of the resultant admittance matrix elements without the need of resorting to any assumptions about the field distribution on the apertures.

3.2.2 Finite Element Analysis (FEA / FEM)

Most EM problems involve either partial differential equations or integral equations. The MoM techniques, described above, are frequently used to solve the integral equations in the frequency domain, but the partial differential equations are solved using finite difference / element analysis / method. Finite Element Analysis (FEA / FEM), sometimes referred to as the Finite Element Method (FEM) or the Finite Difference Method (FDM), has its origin in the field of structural analysis [42]. Derived mathematically originally in 1943 by Courant [43], it wouldn't gain traction until the late 1960s. Analysis of any problem using the FEA method involves four key steps:

1. **Discretization**

   The solution region is divided into a number of subregions or elements. Each of these regions or elements are non-overlapping and the vertices where each of the elements meet form nodes. Therefore, in order to describe a characteristic of the region as a whole, an approximation is made for each element, then, ensuring continuity across element boundaries, the approximate characteristic is given by the sum of the characteristic for each element. As an example, consider the voltage, V(x,y), across a component divided into N elements. To find an approximation for the voltage across the component as a whole, first an approximation of the voltage within each element must be found, $V_e(x, y)$. These voltage distributions must be continuous across inter-element boundaries, leading to an approximate solution for the component of:

$$V(x, y) = \sum_{e=1}^{N} V_e(x, y) \tag{3.1}$$

2. **Element Coefficient Matrix Definition**

   The equations that govern a typical element are identified. These are regarded as the equations that describe the coupling between two nodes. In the above example of considering the voltage across a component, in finding the coupling equations it is also possible to find a set of equations that describe the voltage at any point within the element. The equations are then combined into a matrix $\left[C^{(e)}\right]$, usually called the element coefficient matrix (analogous to the "Stiffness Matrix in structural analysis"), where each element $C_{i,j}$ describes the coupling between nodes i and j. This element coefficient matrix is specific to each element.

3. **Assembly**

   All the elements in the solution region are assembled together, that is the element coefficient matrices for each element are combined into one "global coefficient matrix". Nodes that are adjacent to two or more elements will have matrix contributions from each element, and any elements that refer to nodes that are not directly adjacent will necessarily be zero. For example, when considering two triangles adjoined to form a kite, with each vertex forming a node numbered clockwise from 1 to 4, the elements of the global coefficient matrix

would be as follows:

$$[C] = \begin{bmatrix} C_{11} & C_{12} & C_{13} & C_{14} \\ C_{21} & C_{22} & C_{23} & C_{24} \\ C_{31} & C_{32} & C_{33} & C_{34} \\ C_{41} & C_{42} & C_{43} & C_{44} \end{bmatrix} \tag{3.2}$$

Since there is no direct link or coupling between nodes 1 and 3, those coefficients are 0:

$$= \begin{bmatrix} C_{11} & C_{12} & 0 & C_{14} \\ C_{21} & C_{22} & C_{23} & C_{24} \\ 0 & C_{32} & C_{33} & C_{34} \\ C_{41} & C_{42} & C_{43} & C_{44} \end{bmatrix} \tag{3.3}$$

The remaining coefficients are found by considering the contribution to that position from all elements containing those nodes. For example, both elements in the kite example (labelled 1 and 2) have node 2 in common, hence the coefficient C_{22} will have contributions from both element 1 and element 2.

Additionally, the energy associated with assembling the elements must also be considered, to ensure that the solution is satisfies Laplace's equation.

4. **Solving**

   Laplace's equation is satisfied when the total energy in the solution region is a minimum. Therefore, the partial derivatives of the assembly energy with respect to each nodal value must be zero. This allows a set of simultaneous equations to be found that can then be solved either through an iterative process or matrix algebra to find the solution of the problem.

The division of the solution space into arbitrarily shaped elements has the advantage over the cubic meshes found in other methods of allowing curved boundaries to be represented without the staircasing error that is often introduced. Furthermore, complex structures and inhomogeneous materials can be accounted for accurately [44].

Success has been achieved in using the FEA to describe the scattering of an incident wave by dielectric media within a waveguide. The 3 dimensional approach taken by Ise et al. in [45] was able to determine the magnetic field scattering by the dielectric medium in a rectangular waveguide. In a similar fashion, Soleimani et al. were able to determine the scattering characteristics (S-parameters) of a sample of PTFE placed in a rectangular waveguide by considering the electric field intensity [46]. By implementing an FEM technique, they were able to calculate the magnitudes of the S-parameters of 2 thicknesses of PTFE dielectric material. By comparing their calculations with the known values from literature, it was possible to confirm that this form of FEA can be used in similar investigations in future.

3.2.3 Finite Difference Time Domain (FDTD)

The Finite Difference Time Domain (FDTD) method has some similarities with FEA in so far as the solution is found through solving the partial derivatives of the time-dependent Maxwell' equations in an iterative process. The FDTD method was first proposed by Kane S. Yee [47] as a method of obtaining solutions to the time-dependent Maxwell's equations. The discretization of the problem space into a cubic grid is a crucial part of this technique. The grid points for the E-field and H-field are chosen in such a way that the tangential components of the E-field and the normal

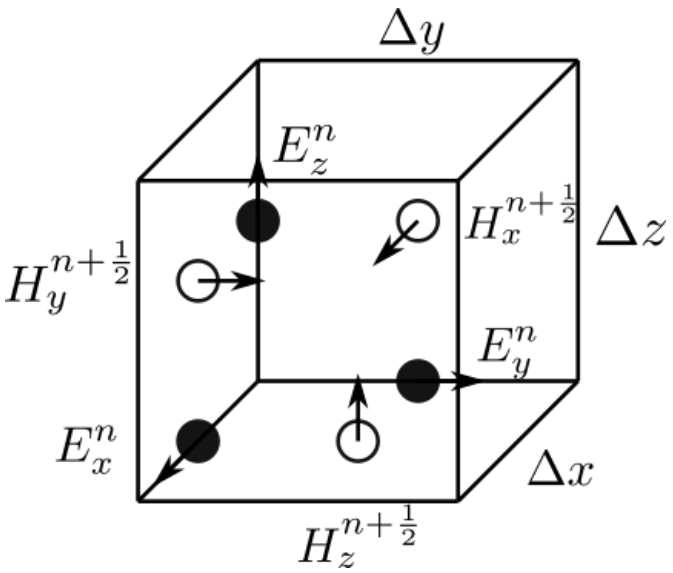

Figure 3.1: A Yee Cell [47].

components of the H-field vanish at the surfaces found at the boundaries of the problem space, for example at the surfaces of the walls of the waveguide. This definition allows each cube in the lattice to be represented by a "Yee cell" shown in figure 3.1.

The Yee cell vastly simplifies and expedites the calculations of the propagating fields and has been a prominent modelling tool in electromagnetism and numerical electromagnetism for many years [48, 49, 50]. FDTD has been implemented across all areas of RF engineering and electromagnetics, with notable advancements in the study of waveguides, metamaterials and optical waveguides achieved through the use of this method [51, 52, 53].

3.2.4 Transmission Line Matrix Method (TLM)

In electromagnetics, there are two overarching regimes that can be employed to provide the solution to the EM phenomena or problems that are being modelled. Determining whether the regime of network theory of field work is most applicable is highly dependent on the problem being solved, and will help identify which modelling technique will be most applicable.

Network theory, a subset of graph theory where the edges and vertices of the graph possess certain attributes, such as voltages, currents, and coupling parameters. Field theory focuses on defining the electric and magnetic fields using Maxwell's equations and the propagation of the wave through the field. Network theory is far more straightforward to employ than field work, but cannot be applied indiscriminately. Which regime would be best suited to solving the problem depends on the electrical size of the circuit. A circuit that is electrically large (size of the circuit is comparable to the wavelength of the highest frequency of interest) in all 3 dimensions, then the field paradigm is best. If electrically large in only one dimensions, network based techniques, which include transmission line theory, are well suited and for electrically small circuits (circuits whose physical size is much smaller than the wavelength of the highest frequency of interest), the lumped components lumped components and quantities such as voltage and current flow aid understanding the most.

The Transmission Line Modelling (TLM) Method draws on the similarities between electrical circuits, EM fields and wave propagation. In a sense, TLM is a bridge between the two regimes of network theory and field work [16]. The main focus of this method is to generate an electrical network analogy to the physical environment, allowing familiar tools, such as Kirchoff's laws, to inform the process of finding the solution.

3.2.4.1 TLM in Two Dimensions

Like many other methods to model wave propagation through a system, the problem space is discretised, commonly based upon a rectangular grid. Formed of connected transmission lines, this grid can then be transformed into a network of series and shunt nodes, through which the wave propagation can be modelled. The series and shunt nodes used in TLM (shown

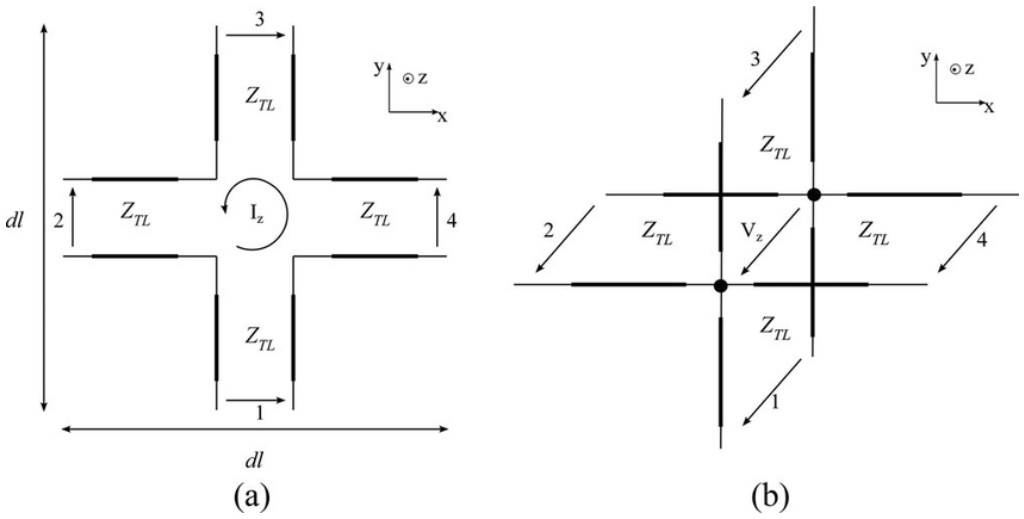

Figure 3.2: (a) A series node in TLM, (b) a shunt node in TLM. Each of these nodes is used to form free space in 2D TLM or combined to generate the expanded TLM node used for TLM modelling in 3 dimensional space. This allows all 6 of the field components to be realised [54].

in figure 3.2) are used individually to model 2D space, or can be combined together to realise 3D objects and systems (more on detail in section 3.2.4.2). The composition of the nodes allows all 6 field components to be determined, providing a complete picture of the propagation of the EM wave.

TLM introduces two types of node in the mesh (scattering network) - the shunt node, which often reprsent TM modes in 2D TLM, and series nodes. In two dimensions, the propagation of the wave through a shunt node, that is the scattering and connection of the incident voltages and currents, is analogous to propagation through a series node. Thus series nodes will be addressed explicitly here, with the scattering and connection processes described, and shunt nodes will have their differences mentioned for completeness.

Following the processes described in *The Transmission-Line Modeling Method in Electromagnetics* [16], it is assumed that the mesh is discretized in a way such that $\Delta x = \Delta y = dl$, where l is the incremental length of the transmission line. The quantity dl is chosen to achieve the

desired spatial resolution, based upon the shortest wavelength of interest. For accuracy, dl is often chosen such that $dl < \frac{\lambda}{10}$. It is also assumed that all transmission lines have the same characteristic impedance, Z_{TL}, which depends on the medium through which the propagation of the EM wave takes place.

The power and beauty of TLM lies in its simplicity. The universal principle of the TLM process is that, at each node and at each time step, there will be four incident pulses that are scattered by the node and propagate away to form the incident pulses for the connected neighbouring nodes at the next time step. This process then repeats.

Using a Thevenin equivalent circuit model, the voltages and currents propagating into and out of the series node in figure 3.2(a) can be computed. Starting with the loop current at time step k, ${}_kI_z$, and evaluating at node (x, y, z) it is shown that:

$$ {}_kI_z = \frac{2_kV_1^i + 2_kV_4^i - 2_kV_3^i - 2_kV_2^i}{4Z_{TL}} \tag{3.4} $$

Subsequently, the various voltages across each port can be calculated. Consider port 1, the total voltage across port 1 is given by:

$$ {}_kV_1 = 2_kV_1^i -_k I_z Z_{TL} \tag{3.5} $$

With the reflected voltage at port 1, in terms of the incident voltage on the other 4 ports, given by:

$$ {}_kV_1^r =_k V_1 -_k V_1^i \tag{3.6} $$

$$ =_k V_1^i -_k I_z Z_{TL} \tag{3.7} $$

$$ = 0.5({}_kV_1^i +_k V_2^i -_k V_3^i -_k V_4^i) \tag{3.8} $$

Similar expressions can be obtained for the reflected voltage at the other ports, consequently, the scattering process can be expressed simply with the definition of a scattering matrix, $\mathbf{S}$:

$$ {}_k\mathbf{V}^r = \mathbf{S}_k\mathbf{V}^i \tag{3.9} $$

where the incident and reflected voltages are defined by the following transpose matrices:

$$ {}_k\mathbf{V}^i = \left\{ {}_kV_1^i \quad {}_kV_2^i \quad {}_kV_3^i \quad {}_kV_4^i \right\}^T \tag{3.10} $$

$$ {}_k\mathbf{V}^r = \left\{ {}_kV_1^r \quad {}_kV_2^r \quad {}_kV_3^r \quad {}_kV_4^r \right\}^T \tag{3.11} $$

with the scattering matrix expressed as:

$$ \mathbf{S} = 0.5 \begin{Bmatrix} 1 & 1 & 1 & -1 \\ 1 & 1 & -1 & 1 \\ 1 & -1 & 1 & 1 \\ -1 & 1 & 1 & 1 \end{Bmatrix} \tag{3.12} $$

The newly calculated incident voltages are then passed to each of the neighbouring nodes through the use of a connection matrix, $\mathbf{C}$. Quite simply this matrix exchanges the pulses with the immediate neighbours of the node in the following fashion:

$$ {}_{k+1}\mathbf{V}^i = C_k\mathbf{V}^r \tag{3.13} $$

$$ {}_{k+1}V_1^i(x,y,z) =_k V_3^r(x,y-1,z) \tag{3.14} $$

$$ {}_{k+1}V_2^i(x,y,z) =_k V_4^r(x-1,y,z) \tag{3.15} $$

$$ {}_{k+1}V_3^i(x,y,z) =_k V_1^r(x,y+1,z) \tag{3.16} $$

$$ {}_{k+1}V_4^i(x,y,z) =_k V_2^r(x+1,y,z) \tag{3.17} $$

Scattering can then be repeated for each subsequent time step for as long as is required. The process described above, determining initial incident voltages, scattering at all nodes, and calculating the incident voltages at all nodes for the subsequent time step, is the fundamental treatment of propagation in TLM.

For shunt nodes (which are generally applicable to propagating TM modes) the process is the same, but the voltages across the node and scattering matrix are defined as follows:

Total Voltage:

$$ {}_kV_Z = \frac{1}{2}\left[{}_kV_1^i + {}_k\,V_2^i + {}_k\,V_3^i + {}_k\,V_4^i\right] \tag{3.18} $$

Voltage reflected from port 1:

$$ {}_kV_1^r = {}_k\,V_Z - {}_k\,V_1^i \tag{3.19} $$

$$ = \frac{1}{2}\left[-{}_kV_1^i + {}_k\,V_2^i + {}_k\,V_3^i + {}_k\,V_4^i\right] \tag{3.20} $$

with the scattering matrix given by:

$$ \mathbf{S} = \frac{1}{2}\begin{Bmatrix} -1 & 1 & 1 & 1 \\ 1 & -1 & 1 & 1 \\ 1 & 1 & -1 & 1 \\ 1 & 1 & 1 & -1 \end{Bmatrix} \tag{3.21} $$

3.2.4.2 3 Dimensional TLM

Expanding upon the concepts and methods of TLM in two dimensions, 3D-TLM can be used to describe electromagnetic signal propagation in all three dimensions. Similarly to 2D TLM, the electromagnetic behaviour in a cell of dimensions $\Delta x \times \Delta y \times \Delta z$ is sought to be represented using an analogy with a 3D network.

The symmetrical condensed node (SCN - Figure 3.3) is the most universally used structure in 3D TLM. Consisting of a network of interconnected lines, each face of the cell hosts 2 ports that are orthogonal to one another. Closer examination of the structure of an SCN reveals its constituents to be the previously studied series and shunt nodes (see figure 3.2). This allows for all polarizations to be accounted for [16]. Simple cubic SCNs are mainly used to describe air-filled cells, though impedances, stubs and other modifications can be made to describe different materials and terminations.

Despite the simple equivalent circuit of an SCN being a quantity that cannot be derived, the excitation, scattering, connection, and output still need to be calculated along with the treatment of boundaries, just like in 2D TLM. Fortunately, it is possible to find the scattering properties of an SCN by relying on more general principles. The fundamental principles enforced that are paramount to obtaining the scattering matrix are:

- Conservation of electric charge
- Conservation of magnetic flux
- Electric field continuity
- Magnetic field continuity

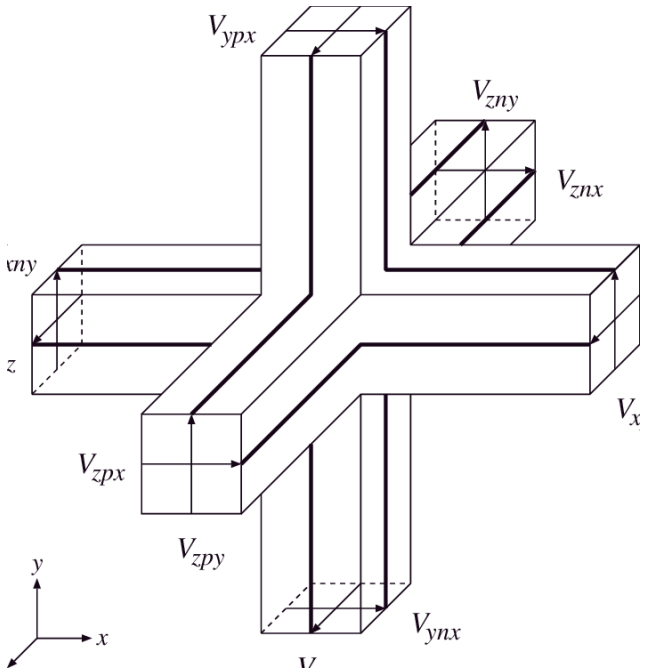

Figure 3.3: A Symmetrical Condensed Node, used in 3D TLM to calculate and propagate the electromagnetic field components in space [55].

Christopoulos et al [16] describe a robust derivation for the voltages and currents at each of the 12 ports of the SCN, which are then used to define the scattering matrix below. Similarly to the 2D case, the reflected and incident voltages across each port are related by:

$$_k\mathbf{V}^r = \mathbf{S}_k\mathbf{V}^i \tag{3.22}$$

However, in three dimensions, the 12 port scattering matrix is found to

be:

$$\mathbf{S} = \frac{1}{2}\begin{Bmatrix} 0 & 1 & 1 & 0 & 0 & 0 & 0 & 0 & 1 & 0 & -1 & 0 \\ 1 & 0 & 0 & 0 & 0 & 1 & 0 & 0 & 0 & -1 & 0 & 1 \\ 1 & 0 & 0 & 1 & 0 & 0 & 0 & 1 & 0 & 0 & 0 & -1 \\ 0 & 0 & 1 & 0 & 1 & 0 & -1 & 0 & 0 & 0 & 1 & 0 \\ 0 & 0 & 0 & 1 & 0 & 1 & 0 & -1 & 0 & 1 & 0 & 0 \\ 0 & 1 & 0 & 0 & 1 & 0 & 1 & 0 & -1 & 0 & 0 & 0 \\ 0 & 0 & 0 & -1 & 0 & 1 & 0 & 1 & 0 & 1 & 0 & 0 \\ 0 & 0 & 1 & 0 & -1 & 0 & 1 & 0 & 0 & 0 & 1 & 0 \\ 1 & 0 & 0 & 0 & 0 & -1 & 0 & 0 & 0 & 1 & 0 & 1 \\ 0 & -1 & 0 & 0 & 1 & 0 & 1 & 0 & 1 & 0 & 0 & 0 \\ -1 & 0 & 0 & 1 & 0 & 0 & 0 & 1 & 0 & 0 & 0 & 1 \\ 0 & 1 & -1 & 0 & 0 & 0 & 0 & 0 & 1 & 0 & 1 & 0 \end{Bmatrix} \tag{3.23}$$

Understandably, the size of the scattering matrix commonly makes it unwieldy to use when programming or computing scattering. Calculating the reflected voltages from the equations below directly often proves a simpler

undertaking:

$$V^r_{ynx} = \frac{1}{2}\left(V^i_{znx} + V^i_{zpy} + V^i_{xny} - V^i_{xpy}\right) \tag{3.24}$$

$$V^r_{ypx} = \frac{1}{2}\left(V^i_{zny} + V^i_{xpy} + V^i_{xny} - V^i_{xpy}\right) \tag{3.25}$$

$$V^r_{znx} = \frac{1}{2}\left(V^i_{ynx} + V^i_{ypx} + V^i_{xnz} - V^i_{xpz}\right) \tag{3.26}$$

$$V^r_{zpx} = \frac{1}{2}\left(V^i_{ynx} + V^i_{ypx} + V^i_{xpz} - V^i_{xnz}\right) \tag{3.27}$$

$$V^r_{zny} = \frac{1}{2}\left(V^i_{xny} + V^i_{xpy} + V^i_{ynz} - V^i_{ypz}\right) \tag{3.28}$$

$$V^r_{zpy} = \frac{1}{2}\left(V^i_{xny} + V^i_{xpy} + V^i_{ypz} - V^i_{ynz}\right) \tag{3.29}$$

$$V^r_{xny} = \frac{1}{2}\left(V^i_{zny} + V^i_{zpy} + V^i_{ynx} - V^i_{ypx}\right) \tag{3.30}$$

$$V^r_{xpy} = \frac{1}{2}\left(V^i_{zny} + V^i_{zpy} + V^i_{ypx} - V^i_{ynx}\right) \tag{3.31}$$

$$V^r_{xnz} = \frac{1}{2}\left(V^i_{ynz} + V^i_{ypz} + V^i_{znx} - V^i_{zpx}\right) \tag{3.32}$$

$$V^r_{xpz} = \frac{1}{2}\left(V^i_{ynz} + V^i_{ypz} + V^i_{zpx} - V^i_{znx}\right) \tag{3.33}$$

$$V^r_{ynz} = \frac{1}{2}\left(V^i_{xnz} + V^i_{xpz} + V^i_{zny} - V^i_{zpy}\right) \tag{3.34}$$

$$V^r_{ypz} = \frac{1}{2}\left(V^i_{xnz} + V^i_{xpz} + V^i_{zpy} - V^i_{zny}\right) \tag{3.35}$$

The above scattering equations, like many other modelling techniques, are based on a cubic cell (with dimensions of $\Delta x = \Delta y = \Delta z = \Delta l$) and, as with the 2D case, all the link lines have the same characteristic impedance ($Z_0 = \sqrt{L/C}$). As before, combining this relation with the expression for the time interval ($\Delta t = \sqrt{LC}$) yields expressions for the capacitance and inductance of:

$$C = \frac{\Delta t}{Z_0} \tag{3.36}$$

$$L = \Delta t Z_0 \tag{3.37}$$

Using these expressions and adding in the material properties of the medium through which the wave passes, it is possible to establish the required time

step for this block of medium. The capacitance and inductance, necessarily must correspond to those of the cell which they describe. This cell represents the block of medium with material parameters ϵ, μ. Considering the capacitance in the x-direction first of all, the four half lines with fields polarised in the x-direction describe a capacitance for that cell of:

$$\epsilon \frac{\Delta y \Delta z}{\Delta x} = \epsilon \Delta l \tag{3.38}$$

$$= 4 \frac{\Delta t/2}{Z_0} \tag{3.39}$$

$$= \frac{2\Delta t}{Z_0} \tag{3.40}$$

Similarly, the inductance represented by the four half lines in the same manner is:

$$\mu \frac{\Delta y \Delta z}{\Delta x} = \mu \Delta l \tag{3.41}$$

$$= f \frac{\Delta t/2}{2} Z_0 \tag{3.42}$$

$$= 2\Delta t Z_0 \tag{3.43}$$

If Z_0 is eliminated by multiplying equation 3.40 with equation 3.43, and make the substitution $u = 1/\sqrt{\epsilon\mu}$, the result is the required time step to represent this block of medium:

$$\Delta t = \frac{\Delta l}{2u} \tag{3.44}$$

The minimum required time step is a key parameter within all computational simulations. It governs the feasibility of all studies as if it is small, simulation durations could become prohibitively large. The size of the minimum required time step depends largely on the smallest feature in the geometry because this dictates the smallest region in the mesh, and therefore the shortest link lines, that need to be solved for. Similarly to the

other modelling methods discussed above, 3D TLM discretises the problem space into a Cartesian grid, with each cell representing a cube in the problem space. This can cause difficulties to arise when considering non-cubic shapes and edges, such as curves (see section 3.2.5 below). Frequently, non-cubic regions, that is regions that do not fit uniformly on the Cartesian grid, lead to ultra fine meshes around them. The short link lines and mesh dimensions in these regions drastically reduce the required time step, significantly increasing simulation run times and therefore are often avoided in favour of approximations, such as a uniform block with a behaviour defined by an equivalent circuit (see Chapter 6 for further information).

3.2.5 Staircasing

A common feature among the methods mentioned above is the requirement of the problem space to be discretised, often into a rectangular or Cartesian grid. Naturally, this has many advantages, not least the ability to break the problem down into smaller, more manageable parts, solving them initially before considering the interconnection between those parts. Despite the logical and practical nature of this process, discretisation frequently introduces an artefact that can increase the requirements for solving the problem and potentially even reduce the accuracy of the output - staircasing.

Staircasing most commonly occurs when trying to solve for a curved surface using a rectangular grid. As can be seen in figure 3.4, the rectangular grid does not properly fit the curve of the circle, thus any curved region is approximated to a jagged edge that resembles a staircase, hence the name. Consequently, when considering scattering off of such a surface, errors are introduced as a result of this approximation.

In order to minimise the errors introduced to the scattering by the

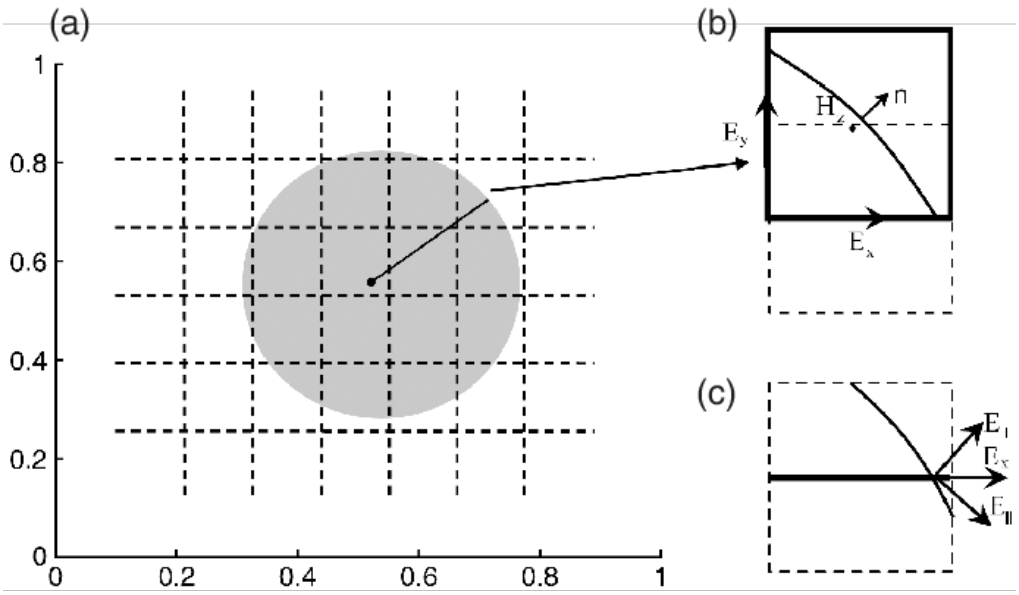

Figure 3.4: A diagram illustrating how representing a curved surface in a rectangular grid can lead to the staircasing error. [56].

grid, a more precise definition of the curve is required. One solution to this is to reduce the size of the mesh or grid to minimise the differences between the surface and the grid. However, reducing the size of the mesh does not eliminate the staircasing error entirely and can significantly increase simulation resource requirements.

Another approach aimed at eliminating the staircasing approximation, explored in FDTD domains, is to introduce regions of effective permittivity and local conformity. Success has been achieved in some microwave and optical simulations ([57, 58, 59, 60]).

An alternative solution to the staircasing issue, with an additional aim of improving the overall accuracy of the simulations, is the unstructured transmission line modelling method, explored in the next section.

3.3 The Unstructured Transmission Line Modelling Method (UTLM)

Built upon the foundations of the transmission line modelling method, the unstructured transmission line modelling method (UTLM) uses an arbitrary tetrahedral mesh instead of the traditional Cartesian grid. UTLM was formulated by Sewell et al. (see [18, 61, 19]) and has seen great success in a variety of RF applications.

The Unstructured Transmission Line Modelling (UTLM) method exploits the analogy between the electromagnetic field solutions of the 3D Maxwell's equations and the voltages and currents found on a network of transmission lines. The nature of UTLM is one of an explicit time stepping algorithm for electromagnetic fields, with the problem being discretised into a set of discrete non-overlapping tetrahedral cells that form a Delaunay mesh [19, 62]. The network of transmission lines is then formed by a dual Voronoi mesh, which connects the circumcentres of neighbouring tetrahedral cells. The quality of the tetrahedral mesh, which is related to the minimum distance between the circumcentres of neighbouring tetrahedral cells (i.e. the minimum length of any transmission line within the problem), dictates the maximum permissible time step in UTLM. Often geometries contain some very small cells that can cause unrealistically small time-steps as a result of the infinitesimal distance between cell circumcentres. However, by clustering these smaller adjacent cells into groups, controlled by a threshold length, the time-step can be raised significantly without compromising the accuracy of the simulation. In practice, the cluster size is restricted to ≤ 200 tetrahedra to prevent the requirement of a substantial pre-processing time. This limit can be overcome by deploying a complexity reduction technique for the treatment of large clusters which combines

Figure 3.5: A primitive mesh constructed using the UTLM algorithm of an inductive cylindrical post discontinuity within a rectangular waveguide. Features of note in this mesh include the tetrahedral shape of the mesh cells and the fine regions around the cylindrical post discontinuity that are clustered together to form larger cells for solving, simultaneously improving the accuracy of the post definition and maximising the timestep size required, reducing the overall simulation time.

SVD (singular value decomposition) techniques, with physically grounded approximations and a hierarchical approach and significantly reduces this pre-processing time [17, 21].

In addition, the tetrahedra allow a more accurate description of any curved surfaces in the geometry, generating a truer reflection of the system being simulated and minimising the effects of the aforementioned staircasing errors that are commonly found when using a mesh to discretize the problem space. Since the main focus of this research is centred around modelling the receiver protection system within a waveguide, which consists of a cylindrical inductive post, cylindrical PiN diode package and arbitrarily curved bonding ribbons to name but a few features, this ability to better describe curved surfaces with minimal increase in simulation time is crucial to making the models explored in this research achievable and a realistic proposition.

The UTLM algorithm has been demonstrated to be second order accurate with respect to wavelength [19] and provide both smooth boundary and good graded mesh capabilities [20]. The UTLM method is also able to deal with lossy dielectrics and magnetic materials as well as carbon-fibre composite (CFC) materials [23, 63, 64]. More recently, UTLM has been

successfully applied to model advanced photonic structures [22] and has been expanded to include a solver for two-dimensional thermal diffusion equations [65].

3.4 Receiver Protectors (RxPs) in Literature

Possibly owing to their sensitivity both commercially and in their application, models and discussions of full receiver protection system (RxP) systems in literature are very rare. One discussion of the simulation of a single stage within a receiver protection systems RxP system is provided in the conference paper by Farrington et al [6]. Their discussion centres around the presentation of a computational electromagnetic model for a single stage of an RxP system. Although present, the discussion of the finer details of the RxP system modelled, including the device parameters, remains understandably vague or absent. However, results from the computational models are presented, show good agreement with experimental results and demonstrate the expected "switching" behaviour between the "off-" and "on-" states of the diode in the system. The results from this paper will be used to qualitatively verify those obtained in this research later in this thesis.

Whilst literature on full RxP systems may be scarce, numerous papers considering the constituent parts of the RxP system are abundant. By breaking down the RxP system into components of waveguide, obstacle / discontinuity, PiN diode, and beyond, detailed studies can be found on almost every individual aspect of the system without the system itself being interrogated. Notably, the effects and behaviour of each shape and

size of waveguide on the propagation of the wave through it, along with the associated analytical models and waveguide theory, can easily be uncovered (see for example [34, 32, 51, 66, 46, 30]).

Similar levels of success have been found in describing the behaviour of the propagating wave after inserting an obstacle or discontinuity into the waveguide. These can take the form of slits, irises or other radiating apertures (see [41, 39]) or a physical obstacle itself, such as an inductive post (as found in [67] for example). Analytically, the works of Leviatan [68] and Beyer [69] were ground-breaking when it came to producing models of the post discontinuity in a waveguide.

Using a combination of method of moments (MoM) and finite element analysis (FEA), Beyer et al [69] perform a modal analysis of waveguide filters and other mode coupling elements. They showed that their method was an efficient way of modelling a variety of waveguide filters, using multiple rectangular post-like obstacles/irises to couple waveguide modes. Initial analysis of only two of these structures produced results in excellent agreement with measurements and when extended to higher numbers of rectangular poles, with asymmetrically positioned irises, coupling was achieved for the four pole filter. Again this was verified, with excellent agreement with measurements.

Leviatan et al [68] introduce a numerical solution to the problem of a single inductive post positioned within a rectangular waveguide. Their rapidly converging solution illustrated an analytical model for this discontinuity and used the Method of Moments (MoM) to extend the earlier work of Marcuvitz et al [32]. Their data showed that it was possible to describe the behaviour of a narrow broadband filter constructed of large single posts. This technique can be extended further to provide a simple yet effective way of modelling and solving for a plethora of microwave filters, including posts of arbitrary shape and irises of different thicknesses.

3.5 Analytical Waveguide Models

The works of Pozar [24], Collin [34], Leviatan [68], and Beyer [69] provide a fundamental basis through which to develop an analytical model of (a) a simple rectangular waveguide and (b) a single inductive post discontinuity within the waveguide system. As the following discussion presents, this can often prove to be unwieldy in an analytical sense and more complex systems, such as an RxP, prove to be prohibitive. Thus, in practice, computer modelling and simulation techniques are used to solve these problems, often with assumptions made along the way.

3.5.1 Empty Rectangular Waveguide

According to transmission line theory, any lossless transmission line (such as a waveguide) can be defined by two properties, the phase constant β and the characteristic impedance of the guide, Z_0, as shown in Figure 3.6. These can be found using electromagnetic field theory and are dependent on the media involved. It is also possible to determine the voltage and current at any point along the line using transmission line theory. These are defined as:

$$V(z) = V^+ e^{-j\beta z} + V^- e^{j\beta z} \tag{3.45}$$

$$I(z) = I^+ e^{-j\beta z} - I^- e^{j\beta z} \tag{3.46}$$

$$I(z) = \frac{1}{Z_0}(V^+ e^{-j\beta z} - V^- e^{j\beta z}) \tag{3.47}$$

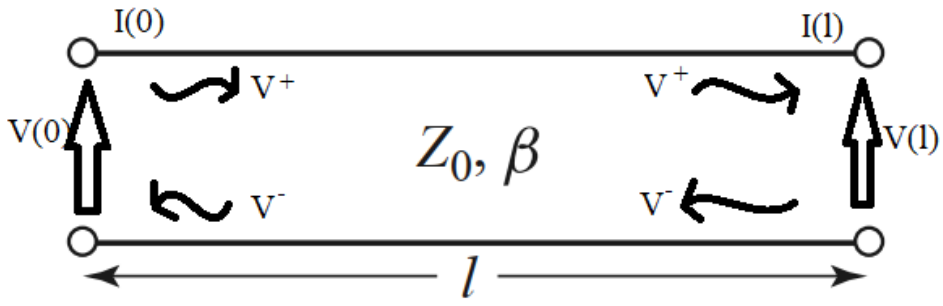

Figure 3.6: A lossless transmission line can be defined by only β and Z_0 (adapted from [24])

3.5.1.1 Phase Constant

The phase constant (β) can be combined with the attenuation constant (α) to form the propagation constant, and is largely dependent upon the frequency and mode of excitation. The general form of the propagation constant (γ) is given by,

$$\gamma = \alpha + j\beta \tag{3.48}$$

For a lossless transmission line, $\alpha = 0$, and so the propagation constant relates only to the phase constant, β. This is quantified as the relationship between the wave number and the frequency dependent cutoff wave number as,

$$\beta = \sqrt{k^2 - k_c^2} \tag{3.49}$$

where k is the wave number and k_c is the cutoff wave number of the exciting mode. k_c is dependent on the dimensions of the waveguide in question and can be calculated by:

$$k_c = \sqrt{\left(\frac{m\pi}{a}\right)^2 + \left(\frac{n\pi}{b}\right)^2} \tag{3.50}$$

where a is the width of the waveguide and b is the height of the waveguide, as shown in figure 2.2. The mode dependence in the cutoff wave number manifests itself in the m, n mode numbers.

The wave number, k, is a combination of the angular frequency, permeability and permittivity of the medium filling the waveguide, in the form,

$$k = \omega\sqrt{\mu\epsilon} \tag{3.51}$$

In general, μ and ϵ are given by:

$$\mu = \mu_r\mu_0 \tag{3.52}$$

$$\epsilon = \epsilon_r\epsilon_0 \tag{3.53}$$

When considering an air filled waveguide, $\mu_r = \epsilon_r = 1$, the permittivity and permeability become their free space counterparts, $\mu = \mu_0$ and $\epsilon = \epsilon_0$

3.5.1.2 Characteristic Impedance

The characteristic impedance of the waveguide is found by considering two components of the electromagnetic field, the electric and the perpendicular component of the magnetic field,

$$Z_0 = \frac{E_x}{H_y} \tag{3.54}$$

$$= \frac{V^+}{I^+} = -\frac{V^-}{I^-} \tag{3.55}$$

These components can be found for a general case by solving Maxwell's and Helmholtz equations. Alternatively, if the transmission line is considered to be a lossless line, it is possibly to use a simple inductance/capacitance relation to find the same quantity [24],

$$Z_0 = \sqrt{\frac{L}{C}} \tag{3.56}$$

For a metal waveguide, we can define a modal impedance for each of the electric and magnetic modes which propagate through the waveguide as[24],

$$Z_{n,m}(TE) = \frac{k_0}{\beta_{n,m}} Z_0 \tag{3.57}$$

$$Z_{n,m}(TM) = \frac{\beta_{n,m}}{k_0} Z_0 \tag{3.58}$$

$$\tag{3.59}$$

This then leads to a definition of the characteristic impedance of,

$$Z_0 = \sqrt{\frac{\mu}{\epsilon}} \tag{3.60}$$

Again, when considering an air filled waveguide, $\mu_r = \epsilon_r = 1$, thus the permittivity and permeability can simple be replaced by their free space counterparts, $\mu = \mu_0$ and $\epsilon = \epsilon_0$

Once armed with β and Z_0, we can substitute them into the transmission (ABCD) matrix [24] to find the voltage and current at the end of the transmission line. The ABCD matrix defines the relationship between the voltage and current at the input and output of the transmission line as,

$$\begin{Bmatrix} V(0) \\ I(0) \end{Bmatrix} = \begin{Bmatrix} cos(\beta l) & jZ_0 sin(\beta l) \\ j\frac{sin(\beta l)}{Z_0} & cos(\beta l) \end{Bmatrix} \begin{Bmatrix} V(l) \\ I(l) \end{Bmatrix} = \begin{Bmatrix} A & B \\ C & D \end{Bmatrix} \begin{Bmatrix} V(l) \\ I(l) \end{Bmatrix} \tag{3.61}$$

Where V(0) and I(0) are the input port voltages and currents and V(l) and I(l) are the output port voltages and currents as shown in figure 3.6. From the ABCD matrix we can obtain the appropriate scattering parameters (S-Parameters). The most useful of these are the reflection coefficient (S_{11}) and the transmission coefficient (S_{21}). These can be found using the

formulae below,

$$S_{11} = \frac{A + \frac{B}{Z_0} - CZ_0 - D}{A + \frac{B}{Z_0} + CZ_0 + D} \tag{3.62}$$

$$S_{21} = \frac{2}{A + \frac{B}{Z_0} + CZ_0 + D} \tag{3.63}$$

For an infinite waveguide, which is an example of a lossless transmission line, these S-Parameters simplify to,

$$S_{11} = 0 \tag{3.64}$$

$$S_{21} = e^{-j\beta l} \tag{3.65}$$

$$= cos(\beta l) - jsin(\beta l) \tag{3.66}$$

For an infinite waveguide, there is a symmetric relation between the S-Parameters that can be used:

$$S_{11} = S_{22} = 0 \tag{3.67}$$

$$S_{12} = S_{21} \neq 0 \tag{3.68}$$

3.5.2 Waveguide with an Inductive Post

Introducing an inductive post into the network will have an impact on its behaviour. The inductive post placed within a waveguide is considered as an example of a discontinuity in the waveguide, which changes the impedance of the network. It can be represented by an equivalent circuit consisting of an inductor and two capacitors, as shown in Figure 3.7 The reactances X_b and X_a can be calculated using a variational method [32] for a post centred in the middle of the waveguide (where $x = \frac{a}{2}$), with the help

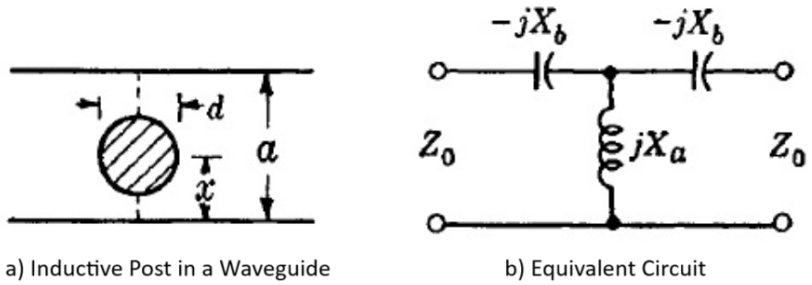

Figure 3.7: The Marcuvitz equivalent circuit for an inductive post in a waveguide. On the left, in panel a) of this illustration, d is the diameter of the post, a is the width of the waveguide and x is the position of the centre of the inductive post from the waveguide wall. In the right hand section, panel b), X_a and X_b are reactances associated with the capacitive and inductive components of the equivalent circuit. [32]

of 2 convergent terms, S_0 and S_2,

$$S_0 = ln\left(\frac{4a}{\pi d}\right) - 2 + 2\sum_{n=3,5,\ldots}^{\infty}\left[\frac{1}{\sqrt{n^2 - \left(\frac{2a}{\lambda}\right)^2}} - \frac{1}{n}\right] \tag{3.69}$$

$$S_2 = ln\left(\frac{4a}{\pi d}\right) - \frac{5}{2} + \frac{11}{3}\left(\frac{\lambda}{2a}\right)^2 - \left(\frac{\lambda}{a}\right)^2\sum_{n=3,5,\ldots}^{\infty}\left[\frac{1}{\sqrt{n^2 - \left(\frac{2a}{\lambda}\right)^2}} - n + \frac{2}{n}\left(\frac{a}{\lambda}\right)^2\right] \tag{3.70}$$

where λ is the wavelength of the incoming signal, which varies with frequency, and a is the width of the waveguide, as above. Using S_0 and S_2, we can calculate the reactances,

$$\frac{X_b}{Z_0} = \frac{4a}{\lambda_G}\left[\frac{\left(\frac{\pi d}{a}\right)^2}{1 + \frac{1}{2}\left(\frac{\pi d}{\lambda}\right)^2\left(S_2 + \frac{3}{4}\right)}\right] \tag{3.71}$$

$$\frac{X_a}{Z_0} - \frac{X_b}{2Z_0} = \frac{a}{2\lambda_G}\left[S_0 - \left(\frac{\pi d}{2\lambda}\right)^2 - \frac{5}{8}\left(\frac{\pi d}{2\lambda}\right)^4 - 2\left(\frac{\pi d}{2\lambda}\right)^4\left(S_2 - 2S_0\frac{\lambda^2}{\lambda_G^2}\right)^2\right] \tag{3.72}$$

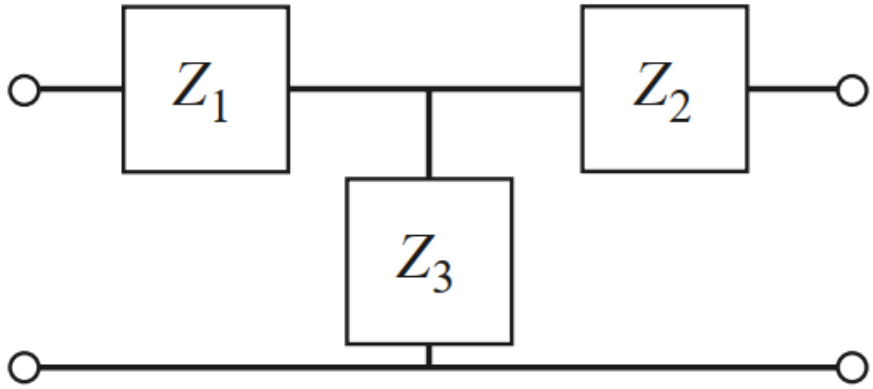

Figure 3.8: The T-Shape equivalent network for a general discontinuity in a waveguide [24]

where λ_G is the guide wavelength and Z_0 is the characteristic impedance.

When analysing the overall behaviour of the waveguide, we can consider the inductive post as one stage sandwiched between two empty waveguide stages. This uses the ABCD matrix above (equation 2.17) and creates a product of 3 matrices,

$$\begin{Bmatrix} A_{tot} & B_{tot} \\ C_{tot} & D_{tot} \end{Bmatrix} = \begin{Bmatrix} A_0 & B_0 \\ C_0 & D_0 \end{Bmatrix} \begin{Bmatrix} A_{Dis} & B_{Dis} \\ C_{Dis} & D_{Dis} \end{Bmatrix} \begin{Bmatrix} A_0 & B_0 \\ C_0 & D_0 \end{Bmatrix} \tag{3.73}$$

Where the subscript 0 refers to an empty waveguide stage (i.e. the ABCD matrix of equation 3.61), the subscript *Dis* refers to the discontinuity stage with *tot* used to refer to the entire waveguide-post network.

In order to find the ABCD matrix for the discontinuity region, it is useful to transform the equivalent circuit into a T-shaped set of equivalent impedances as shown in Figure 3.8 above.

From the equivalent circuit in Figure 3.7, we can see that $Z_1 = Z_2$, simplifying the complexity slightly thus we can write the ABCD matrix for

this stage as [24],

$$\begin{Bmatrix} A_{Dis} & B_{Dis} \\ C_{Dis} & D_{Dis} \end{Bmatrix} = \begin{Bmatrix} 1 + \frac{Z_1}{Z_3} & 2Z_1 + \frac{Z_1^2}{Z_3} \\ \frac{1}{Z_3} & 1 + \frac{Z_1}{Z_3} \end{Bmatrix} \tag{3.74}$$

.

When we compare the impedance equivalent circuit in Figure 3.8 with the Marcuvitz equivalent circuit in Figure 3.7, we can see that $Z_1 = -jX_b$, $Z_2 = -jX_b$ and $Z_3 = jX_a$. Substituting these into the matrix in equation 3.74 we find:

$$\begin{Bmatrix} A_{Dis} & B_{Dis} \\ C_{Dis} & D_{Dis} \end{Bmatrix} = \begin{Bmatrix} 1 - \frac{X_b}{X_a} & -2jX_b - \frac{X_b^2}{jX_a} \\ \frac{1}{jX_a} & 1 - \frac{X_b}{X_a} \end{Bmatrix} \tag{3.75}$$

Finally, to obtain the S-parameters for the network, we first need to combine the ABCD Matrices for all 3 stages of the transmission line into one total ABCD matrix, as illustrated in equation 2.29. Substituting in the values from the matrices in equations 2.17 and 2.31 we obtain:

$$\begin{Bmatrix} V(0) \\ I(0) \end{Bmatrix} = \begin{Bmatrix} cos(\beta l) & jZ_0 sin(\beta l) \\ j\frac{sin(\beta l)}{Z_0} & cos(\beta l) \end{Bmatrix} \cdot \begin{Bmatrix} 1 - \frac{X_b}{X_a} & -2jX_b - \frac{X_b^2}{jX_a} \\ \frac{1}{jX_a} & 1 - \frac{X_b}{X_a} \end{Bmatrix} \cdot \begin{Bmatrix} cos(\beta l) & jZ_0 sin(\beta l) \\ j\frac{sin(\beta l)}{Z_0} & cos(\beta l) \end{Bmatrix} \begin{Bmatrix} V(l) \\ I(l) \end{Bmatrix} \tag{3.76}$$

Completing the matrix algebra we can arrive at the final ABCD

matrix for the complete cascaded network of:

$$\begin{Bmatrix} A_{tot} & B_{tot} \\ C_{tot} & D_{tot} \end{Bmatrix} = \begin{Bmatrix} \frac{sin(\beta l)}{Z_0}\left[cos(\beta l)\left(2X_b - \frac{X_b^2}{X_a}\right) + Z_0 sin(\beta l)\left(\frac{X_b}{X_a} - 1\right)\right] & jZ_0 sin(\beta l)\left[cos(\beta l)\left(\frac{X_b}{X_a} - 1\right) - \frac{Z_0 sin(\beta l)}{X_a}\right] \\ -cos(\beta l)\left[cos(\beta l)\left(\frac{X_b}{X_a} - 1\right) - \frac{Z_0 sin(\beta l)}{X_a}\right] & -jcos(\beta l)\left[cos(\beta l)\left(2X_b - \frac{X_b^2}{X_a}\right)\right] \\ -jcos(\beta l)\left[\frac{cos(\beta l)}{X_a} + \frac{sin(\beta l)\left(\frac{X_b}{X_a} - 1\right)}{Z_0}\right] & Z_0 sin(\beta l)\left[\frac{cos(\beta l)}{X_a} + \frac{sin(\beta l)\left(\frac{X_b}{X_a} - 1\right)}{Z_0}\right] \\ -\frac{jsin(\beta l)}{Z_0}\left[cos(\beta l)\left(\frac{X_b}{X_a} - 1\right) - \frac{sin(\beta l)}{Z_0}\left(2X_b - \frac{X_b^2}{X_a}\right)\right] & -cos(\beta l)\left[cos(\beta l)\left(\frac{X_b}{X_a} - 1\right) - \frac{sin(\beta l)}{Z_0}\left(2X_b - \frac{X_b^2}{X_a}\right)\right] \end{Bmatrix} \tag{3.77}$$

Now that we have the complete ABCD Matrix for the entire Cascaded Network of a waveguide with an inductive post, we can calculate the S-parameters using equations 3.62 and 3.63:

$$S_{11} = -j\frac{(sin(\beta l) + jcos(\beta l))^2 (Z_0 + jX_b)\left(-4{X_a}^2 X_b + 4X_a {X_b}^2 - 2jX_a X_b Z_0 + 2X_a {Z_0}^2 - {X_b}^3 + j{X_b}^2 Z_0 - X_b {Z_0}^2 + j{Z_0}^3\right)}{\left(cos(\beta l)^2 + sin(\beta l)^2\right)\left({X_b}^2 + {Z_0}^2\right)\left(4{X_a}^2 - 4X_a X_b + {X_b}^2 + {Z_0}^2\right)} \tag{3.78}$$

$$S_{21} = -\frac{2X_a Z_0}{(cos(\beta l) + jsin(\beta l),)^2 (X_b + jZ_0)(Z_0 + 2jX_a - jX_b)} \tag{3.79}$$

3.5.3 Waveguide with Multiple Posts

When considering a waveguide with multiple posts, the cascaded network would have a larger ABCD network, obtained by multiplying the matrix in equation 3.73 by another sequence of the matrix in equation 3.75 (for the post), henceforth referred to as matrix B, and the matrix in equation 3.61 (for an empty waveguide), henceforth referred to as matrix A. This can be illustrated as,

$$\begin{Bmatrix} A_{MultiPost} & B_{MultiPost} \\ C_{MultiPost} & D_{MultiPost} \end{Bmatrix} = A(BA)^n \tag{3.80}$$

where n is the number of posts in the system and that the posts are equally spaced and are symmetric with respect to the input and output ports.

Insertion loss results from the insertion of a device in a transmission line, most commonly in this research the inductive post and ultimately the SSRPs and is defined as the reduction in signal power caused by this. It is a ratio of the signal level with and without the insertion of the device.[24, 34] Return loss is the loss in power of the signal returned or reflected by a discontinuity in the transmission line (again the inductive post or SSRP)[35].

The insertion and return losses are calculated by [24, 34],

$$\text{Insertion Loss} = 20log_{10}(|S_{21}|) \tag{3.81}$$

$$\text{Return Loss} = 20log_{10}(|S_{11}|) \tag{3.82}$$

Although the analytical models provide a good representation of the underlying physics of the problem, they also include approximations and assumptions. In the case of the above model of discontinuities within a waveguide, one assumption is that no power is lost in the system ($|S_{11}|^2 + |S_{21}|^2 = 1$). In practical systems, some power is dissipated through scattering, whilst more, although minute amounts, is lost through absorption of the walls and other components.

In the next chapter, the first set of simulation results will be presented. Using the UTLM modelling method discussed in this chapter, a selection of the individual components of an RxP system will be thoroughly investigated to establish their impact on the S-Parameters of the system. Starting with an empty waveguide geometry, UTLM will be used to solve for the S-Parameters before additional components are added in a piecewise fashion and their parameters modified and simulated to provide a deeper understanding.

Chapter 4

Piecewise Analysis of an RxP

This chapter presents the first simulation results achieved in this research. The focus of the investigation detailed here is to investigate the change in s-parameters exhibited by the RxP system as each new component is added in a piecewise manner. The constructions of the RxP system begins with an empty WG16 - WR90 rectangular waveguide. To this, an inductive post, threaded boss, and resonant cavity are added, with their various parameters, such as diameter and depth, explored along the way. The process of constructing and simulating in UTLM is outlined in (4.2). The first results are presented in section 4.4, where the simulation of an empty rectangular waveguide is presented for completeness and verification. The inductive post is added into the system in section 4.5. To minimise requirements, the first of these results focuses on the number of sides required on the polyhedron used to represent the post. The second results investigate how the diameter of the post impacts the s-parameters. In a similar way, section 4.6 studies the effects of including the threaded boss at the top of the post, understanding how the thickness and depth of that changes the system response. Section 4.7 looks at how the diameter of the resonant

cavity below the post, and so the length of the post, changes the behaviour of the system. Finally, a brief discussion of the other components of an RxP system is included in 4.8, along with an explanation of their uses.

4.1 Introduction

The anatomy of a receiver protector device (RxP) can be easily divided into two distinct regions. The PiN diode is encapsulated within a dielectric package with metallic contacts at either end. The analysis of the PiN diode in this research will be introduced and studied in detail in a later chapter (see chapter 7).

This chapter will present an exploration into the addition of specific key components into the RxP system. Starting with an empty waveguide, the RxP will be built "from the ground up" by adding an inductive post, upper boss, and lower cavity one by one, with their impact on the s-parameters of the system analysed. To gain an understand of how these components interact with the incident wave, their parameters, such as depth and diameter, will be varied and studied.

4.2 Method

The process of simulating a geometry in UTLM is relatively straightforward and can be broken down into three distinct sections, **Geometry Creation, Simulation,** and **Analysis**, as displayed in figure 4.1.

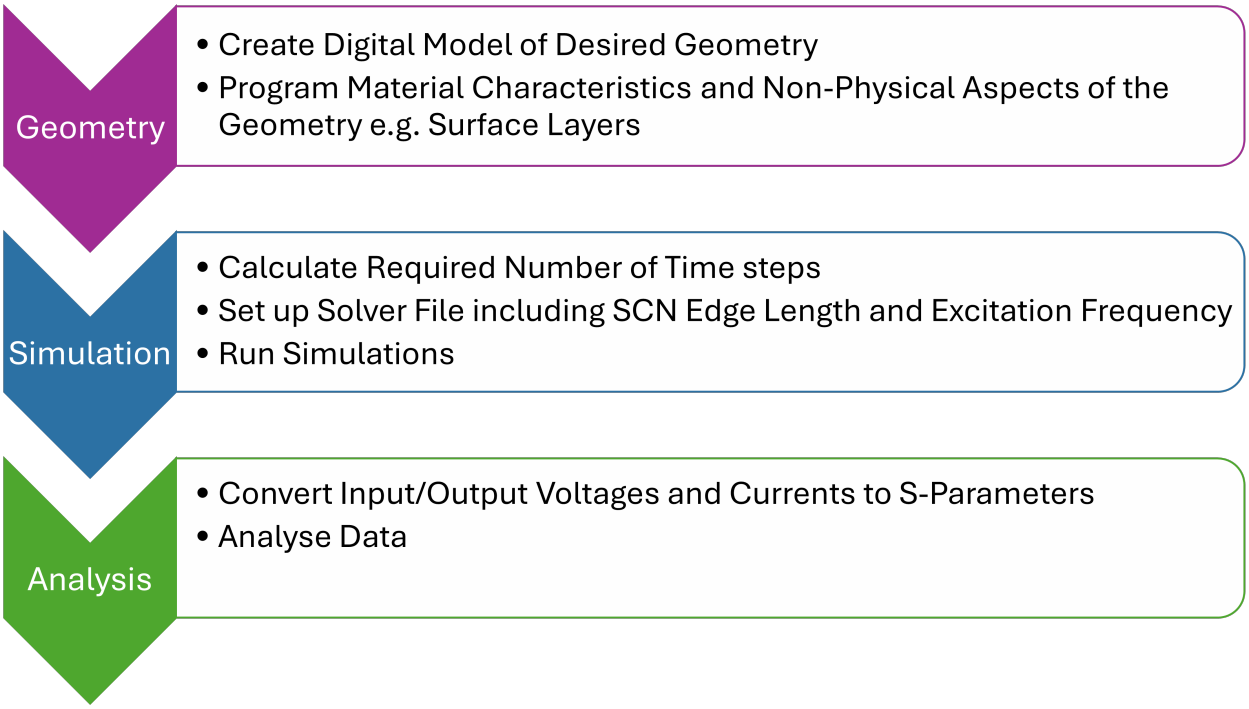

Figure 4.1: A chart showing the steps completed in each phase of the diode modelling investigation.

4.2.1 Geometry Creation

The first step in the process is to design the digital model of the geometry. This process needs to ensure that the model is a true reflection of the physical device and ensure that the device is modelled in as much detail as possible. If there are small elements in the geometry that may cause an ultra fine mesh, these features can either be replaced by an approximation or have a special region of mesh refinement defined for them. The mesh refinement details areas where the mesh size has been reduced by a factor. This finer mesh is seamlessly integrated in the bulk mesh and minimises the requirements for the simulation. Similarly, some surfaces, such as the metallic post, can have their volume excluded from the mesh, since the incident wave will not propagate into these regions.

Once the mesh has been created, the last details of the geometry can be encoded in the simulation set-up, including the material properties of the components, surface layers, simulation observables and electronic

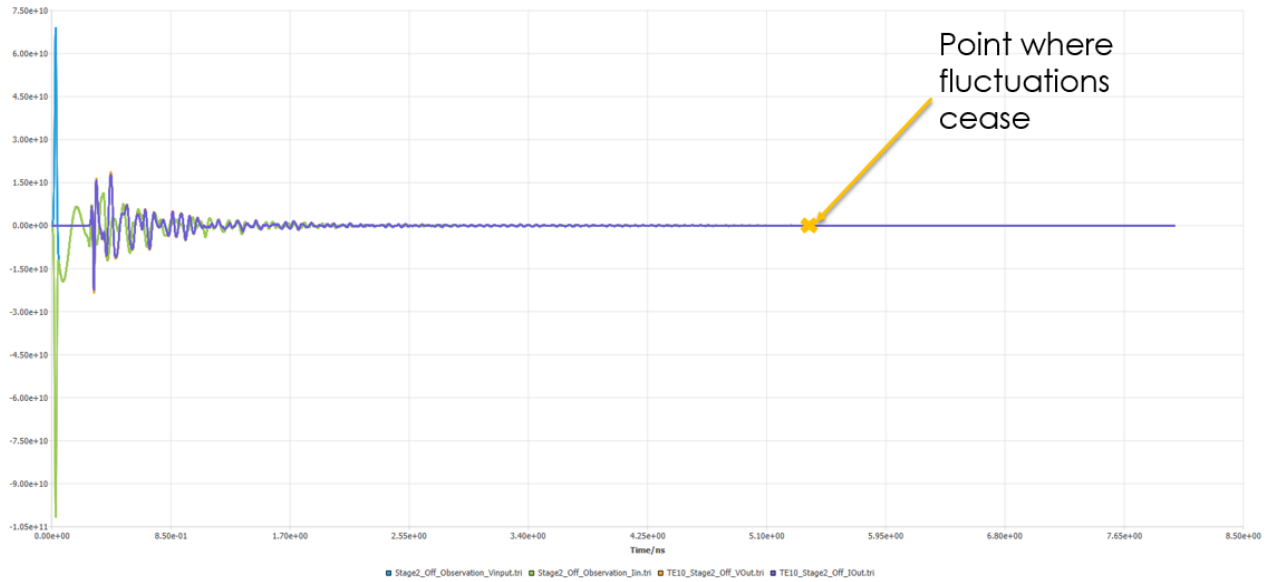

Figure 4.2: The data from a test simulation plotted in the time domain. from this graph it is possible to work out the minimum number of required time steps by (a) identifying the point at which the time domain fluctuations in the data cease and reading off the time, (b) using this time and dividing it by the equivalent SCN edge length to generate the minimum number of time steps required to have a good resolution on the S-Parameter graphs.

properties. The most useful for this research were the surface layers, conductivity and dielectric constant.

4.2.2 Simulation

The simulation phase defines the key parameters to run the simulation. The first step is to determine the number of time steps required and the clustering threshold. The clustering threshold is the circumcentre separation below which adjacent tetrahedra are clustered together t form larger, arbitrary shapes [20]. A trial simulation is used to achieve this. The trial is terminated after the initial set up to read the smallest symmetrically condensed node (SCN) edge length. Setting the clustering threshold to at least twice this value, the simulation is then run again to determine the minimum number of time steps. By observing the point in the time domain where the oscillations cease, as shown in figure 4.2, the time duration

at that point is then divided by the time step size to give the minimum number of time steps. The simulation can now be run and the output data analysed.

4.2.3 Analysis

From the simulation, the input and output voltages and currents can be combined to yield the s-parameters using the relations found in equations 3.62 and 3.63. Visualisations of the input and output modes, E- fields and H-fields can also be studied. The s-parameters can be combined to study the power conservation of the system using equation 2.65a or they can be used to define the reflection and transmission coefficients. As their names suggest, the reflection and transmission coefficients are a measure of how well the incident signal is reflected or transmitted through the geometry.

Finally, plotting S_{11} and S_{21} on a frequency / attenuation axis provides an insight into the signal propagation at a given frequency. Frequency bands of transmission and reflection can be found by looking for areas where, in the case of transmission $S_{21} \approx 0$ and S_{11} is a minimum. For bands of reflection, the opposite is true.

4.3 Construction of the RxP

The efficacy of an RxP system relies on the interaction between the incident electromagnetic wave and the components that comprise the RxP system, thus the components with significant physical size will have a stronger interaction with the wave. This is reliant on the material of the components being such that they will interact with the incident wave, i.e. conductive, though in all practical RxP system, the post, upper boss, and internal coat-

ing of the waveguide and lower cavity are all metallic, and the ceramic and PTFE components that are added principally to tune the response, such as the PTFE tape.

The only other component that may be included in an RxP system that are not related to the diode package are layers of PTFE tape around the lower middle portion of the inductive post. Although common in many practical systems, the use of PTFE tape is to further tune the device. The inclusion of PTFE tape is reasonably well understood and therefore is not explored in this research.

It is worth noting that the presence of the diode generates the switching behaviour by changing from reverse to forward bias. Therefore, since the inclusion of discontinuities wuthin the waveguide serve the purpose of protecting the receiver and obstructing the propagating signal, the geometries explored in this chapter focus solely on the "On-State". The "Off State" exploration becomes possible with the inclusion of the PiN diode and is investigated in the geometries presented in chapter 7. Investigating only the "On-State" has allowed a direct comparison of the scattering behaviour of the physical geometries to be considered that arises from the addition of a diode. As mentioned above, the inclusion of the diode will be explored more in chapter 7, where the model will be advanced from a simple "switching block" geometry to a fully detailed, 3 layer PiN diode.

4.4 Empty Waveguide

The first step of comprehensively understanding the response of the RxP system is the trivial one of an empty waveguide. The dimensions of the waveguide are always chosen to best suit the application, with the dimensions of the aperture of the waveguide dictating the cut-off frequency and

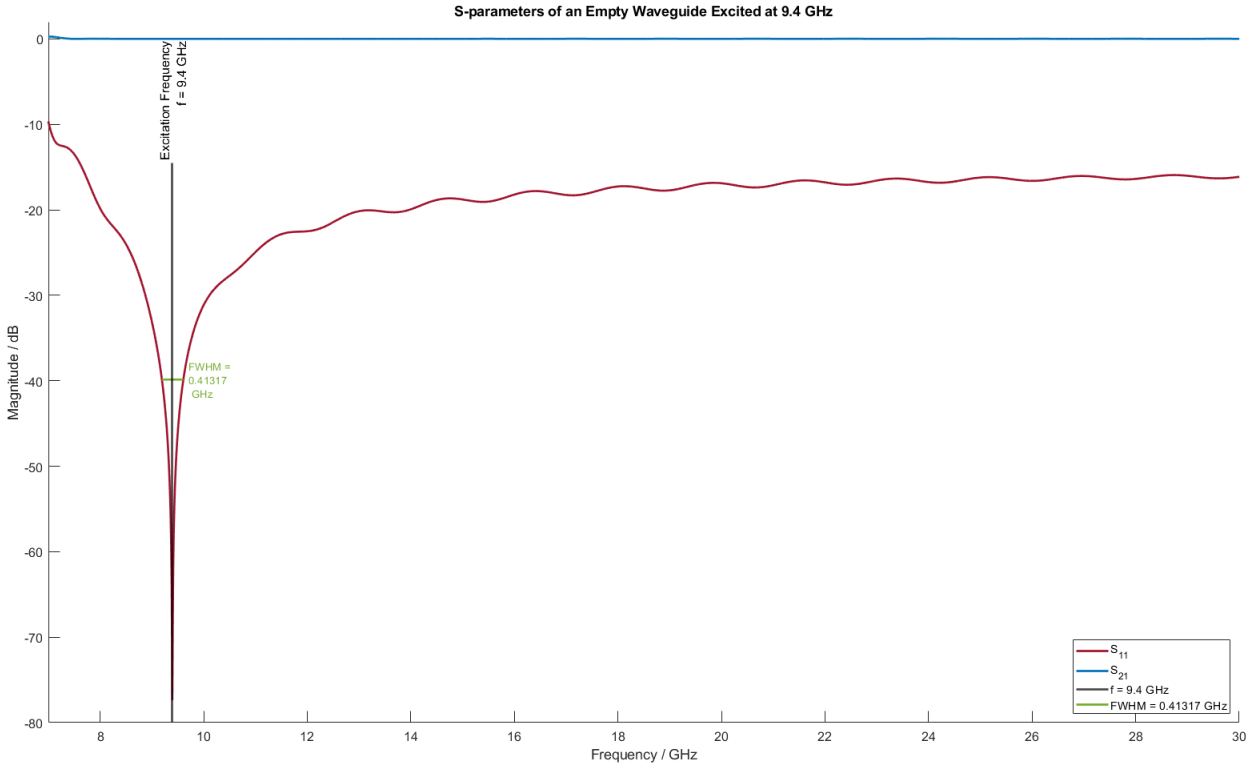

Figure 4.3: The graph above shows the S-parameter response for an empty WG16 waveguide when excited at 9.4 GHz. As predicted by theoretical evaluation, the area of maximum transmission occurs centred around 9.4 GHz, where the signal propagating through the waveguide is at it's strongest.

subsequently the frequency band. For this reason, the dimensions of the waveguide were not studied in this project since a specific application was considered throughout. The empty waveguide simulation presented here was used as a proof of concept.

The signal passed to a waveguide without an obstacle present should pass through unimpeded. This can be modelled using the simple transmission line (as discussed previously in chapter 3), with maximum transmission occurring at the frequency of the incoming signal. For this simulation, the system is excited with a waveguide modal voltage of 1 V at a frequency of 9.4 GHz. This led to an effective refractive index (n_{eff}) of ≈ 0.705.

The waveguide in this model is a WR90-WG16-R100 rectangular waveguide, with a lower cut-off frequency of 6.557 GHz and a recommended frequency band of 8.20 to 12.40 GHz [70]. The excitation was at 9.4 GHz,

and the waveguide itself was meshed with a 1mm mesh throughout, no refinement. This resulted in an equivalent (symmetrically condensed node) SCN edge length of 0.47 mm, a timestep duration, dt, of 0.783876 ps, with the simulation running for a total of 2 million timesteps, taking approximately 20 minutes to complete.

Figure 4.3 shows $S_{21} = 0$dB over all of the frequency range and that S_{11} is a minimum at the excitation frequency but is always at a minimum across the whole frequency range. This suggests that the signal propagates through the empty waveguide unimpeded and that the solver has been correctly configured for this application.

One measure that can be used to characterise resonances in frequency data is the full-width-half-maximum (FWHM). This describes the width of the peak or trough in the data at half the maximum value. For this research, the FWHM has been calculated for the minimum values of S_{11} to explore how the transmission region that arises above the operating band varies and how, by manipulating the configuration of the RxP components, it is possible to alter this region. In essence, the transmission region seen in the empty waveguide at the excitation frequency moves to higher frequencies as the RxP system is introduced. Given that the purpose of an RxP system is to prevent transmission, a region of transmission outside the operating band is not desired behaviour. For the empty waveguide, the FWHM is seen to be 0.41 GHz.

4.5 Adding the Post

As the largest physical component of the RxP system, the inductive post is one of the key driving factors in the system's performance. To the incident wave, the inductive post provides a barrier to propagation that needs to be

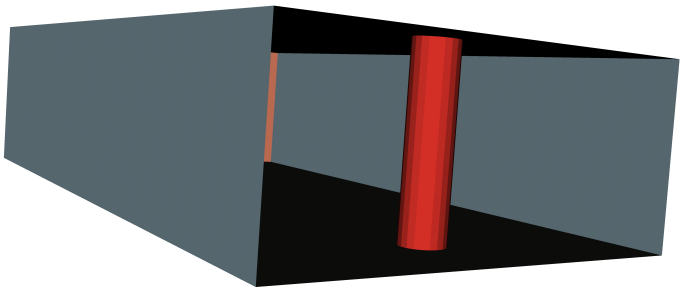

Figure 4.4: It can be seen that the inclusion of the inductive post into the waveguide can represent a significant discontinuity.

carefully designed. If the obstruction is too large, the propagating signal will be unable to pass through, even if the strength is appropriate, rendering the system useless. Conversely, too small and the RxP system will not fully prevent passage of incident damaging signals, having a detrimental effect on the receiver. It is documented that the inclusion of inductive post discontinuities within a waveguide can be used to make a narrow bandpass filter (see chapter 3, for the theory behind the application, specifically the works by Leviatan et al. [68] and Marcuvitz et al.[32]).

Adding the inductive post as a discontinuity within the waveguide causes the incident wave to be scattered by the post. From the aforementioned works, it is visible that the dimensions of the inductive post contribute strongly to this scattering effect, which commonly manifests as a frequency shift in the main transmission/reflection region, creation of additional transmission/reflection regions and further oscillations in both S_{21} and S_{11}.

The post is grounded by directly attaching it at both ends to the top and bottom waveguide walls. This connection is achieved in the models in this chapter by merging the post with the waveguide. As a result is a post that is both physically and electrically connected to the ground structure

within the waveguide cavity.

4.5.1 Post Approximation

The inclusion of the inductive post within the RxP system starts with the definition of the geometry of the post. In practical applications, the post is a perfect cylinder. However, curved surfaces are difficult to simulate and are computationally expensive. Therefore, an approximation to the perfect cylinder needs to be made using a multi-faceted polyhedron. In this investigation, polyhedrons with multiple faces, increasing in number, are simulated. Their s-parameter results are plotted in figure 4.5 to visualise how the approximation to a cylinder improves with increasing side number. Below are the results for posts with 4, 8, 10, 12, 16 and 20 sides.

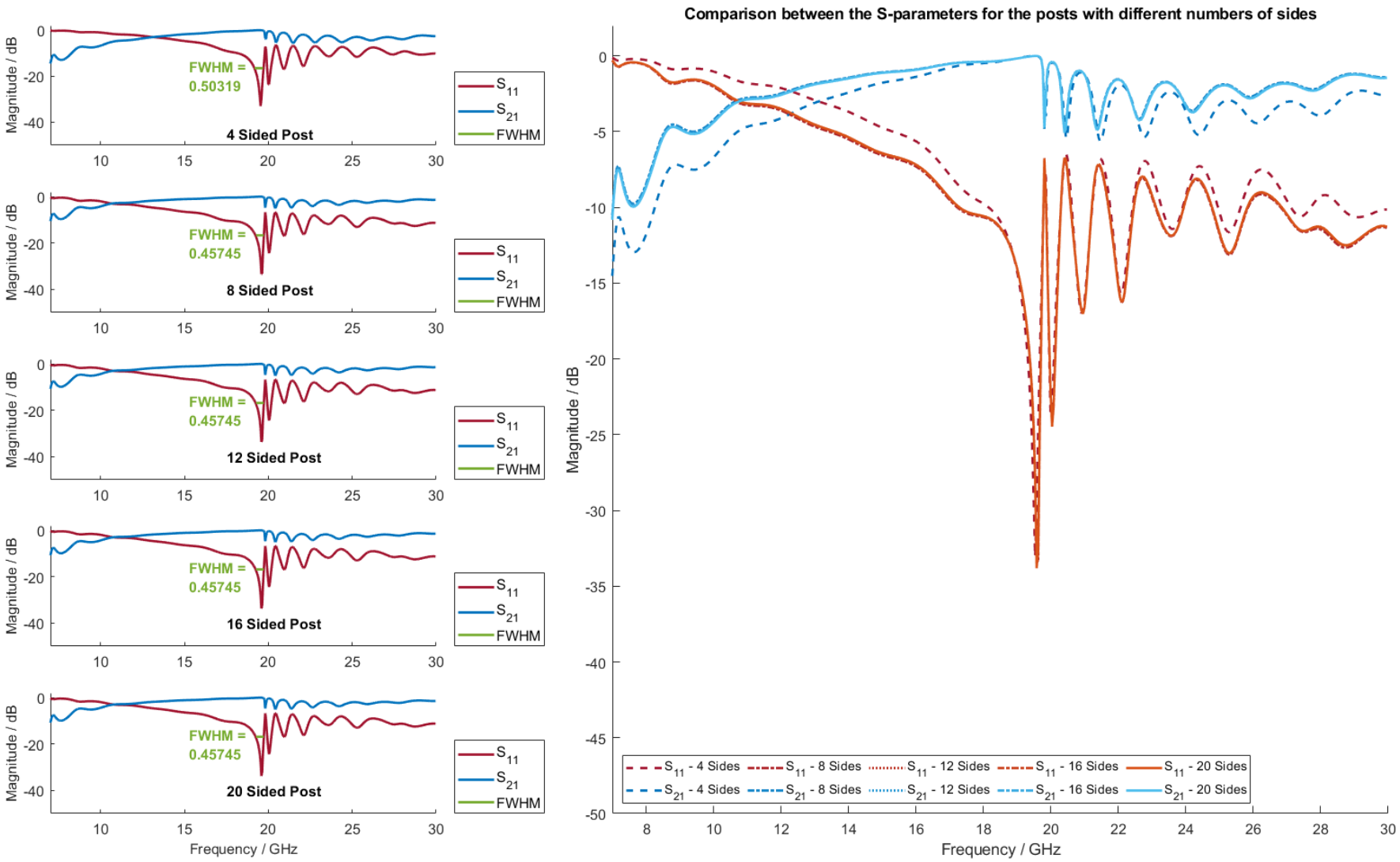

Figure 4.5: A perfect cylinder is effectively a post with an infinite number of sides. The more sides a post has in the geometry, the more expensive it becomes to model.The data from the simulations in this investigation showed that, since the data converges as the number of sides is increased beyond 16, that a 20 sided post will be a good approximation for the inductive post in the geometry. Increasing the number of sides above 20 showed negligible improvements, but increased resource requirements for the simulations.

As can be seen in figure 4.5, as the number of sides increases, the response of the post converges. This is further supported by the FWHM converging to 0.45745 GHz for all polyhedra with 8 or more sides. Given this convergence, it can be suggested that a polyhedron with 20 sides provides a near-perfect approximation to a cylinder. The convergence observed, the traces becoming stacked on top of one another, and the similarity of the FWHM results, particularly between 16 and 20 sides, suggests that above 12 sides should prove a sufficient approximation. Therefore, moving forward in this research, a 16 sided polyhedron was used as an approximation for the post.

4.5.2 Post Diameter Investigation

In this second investigation, change in s-parameters caused by the diameter of the inductive post is explored. For this investigation, the inductive post was placed in the centre of the waveguide at a multiple of $\lambda_g/2$. The geometry was meshed with a 1 mm mesh throughout, no refinement, unless the diameter of the post required a reduced mesh size. The structure of the investigation was in two parts, an initial phase of large variations in post diameter ($\approx 0.5mm$) followed by a second level of finer variations ($\approx 0.1mm$) aimed at refining the relationship between diameter and wave propagation. Each simulation was run for a total of 4 Million time steps, with the SCN equivalent Edge Length and the time step duration, dt, chosen appropriately for the geometry. Figures 4.6,4.7 show a subset of the s-parameter responses with post diameter from this investigation.

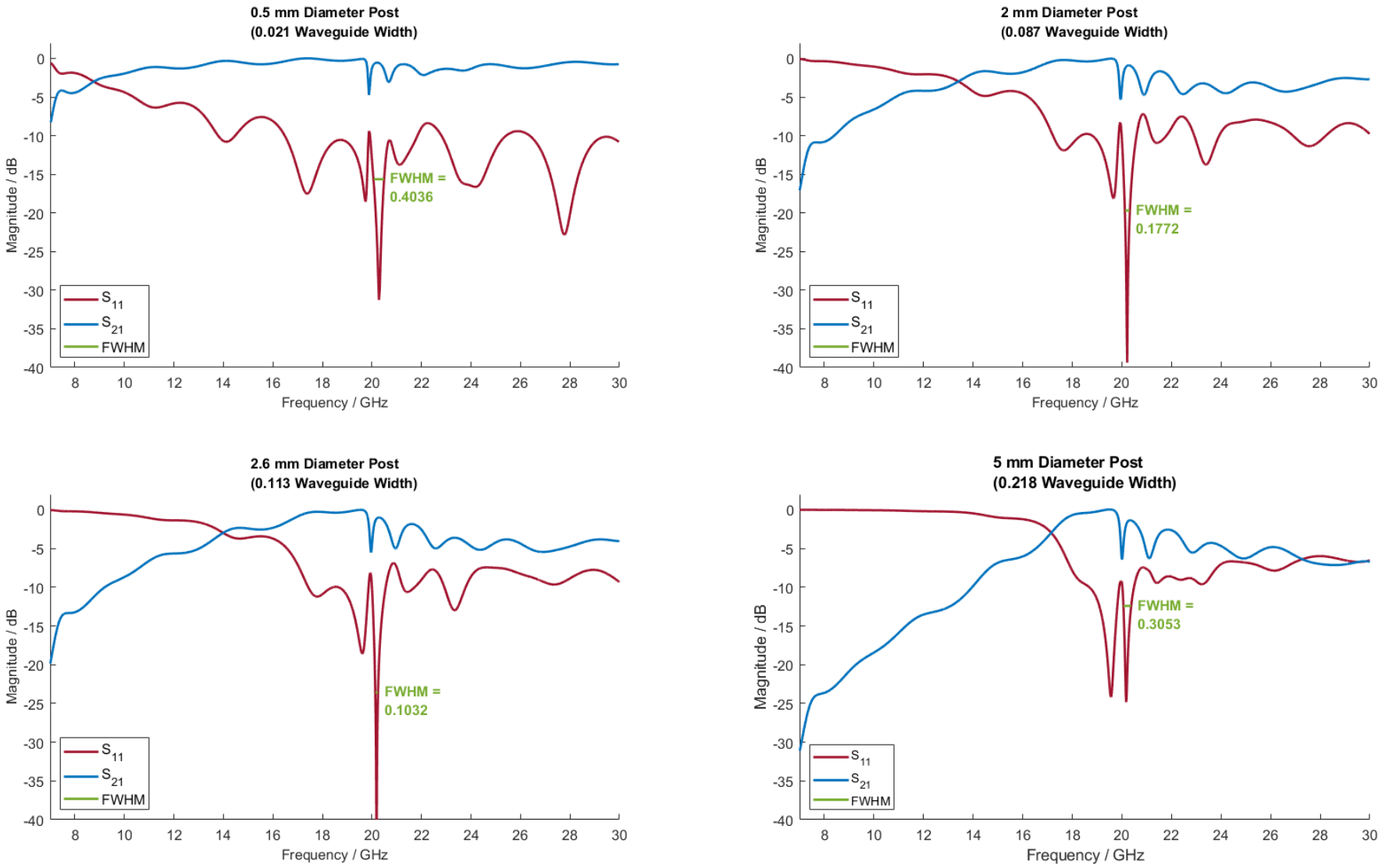

Figure 4.6: A subset of data from the investigation into the diameter of the post. The s-parameters in this panels show that the inclusion of the inductive post generates a region of reflection, which extends to higher frequency as the diameter of the post increases.

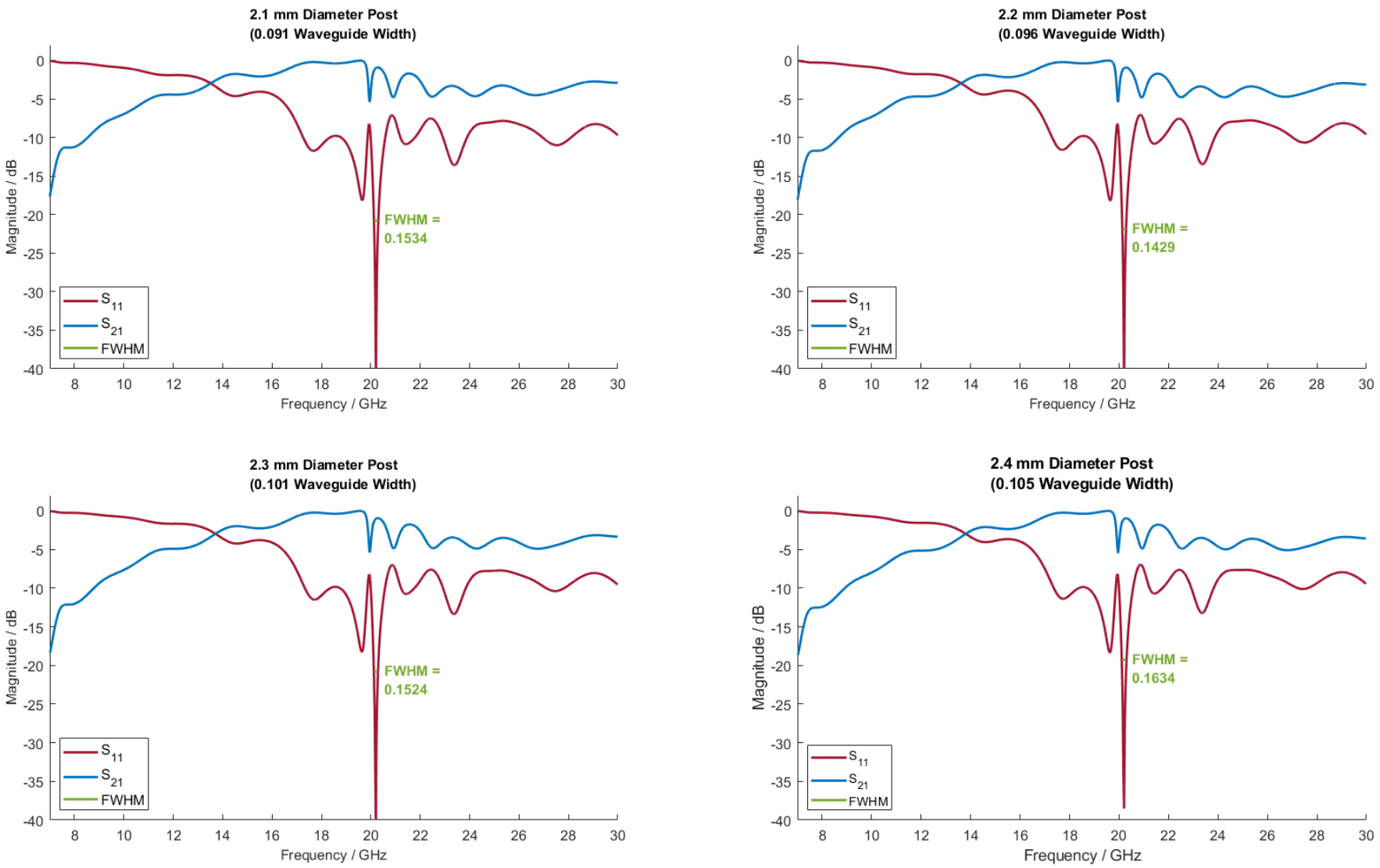

Figure 4.7: The impact of fine variations (0.1 mm) in the diameter of the inductive post on the s-parameters of the RxP system.

Figures 4.6,4.7 display the s-parameter behaviour of the system as the diameter of the inductive post increases. An initial region of reflection, where S_{11} is at a maximum and S_{21} a minimum is seen in each of the graphs, followed by a region of transmission where these characteristics are reversed. The spread of this reflection to higher frequencies increases as the diameter of the post increases.

The FWHM measurements indicate that this region of peak transmission is largest with the smallest diameter post and decreases as diameter increases towards 2.6mm. The 0.5mm diameter post has a FWHM = 0.4036 GHz, which is comparable to the empty waveguide, though the peak transmission region exists at a higher frequency with the post present. The 5mm diameter post causes noticeable scattering effects, with a significant broadening of the initial reflection region. It has also resulted in an increased transmission region following this, with a FWHM = 0.3053 GHz, with another, similar peak adjacent. This is likely due to the significant portion of the waveguide that it fills, with a diameter of $\approx$ 20% of the waveguide. Figure 4.7 suggests that small adjustments to the diameter of the post (0.1mm) do not have a big impact on the behaviour, with a maximum change in FWHM of $\leq$ 0.01 GHz between measurements.

For this research, a diameter of 2.2mm was selected as this exhibited good reflection characteristics in band without added reflection above band.

4.6 Adding the Upper Boss

The second component to be added into the system is the upper threaded boss. Though largely used to tune the system, the boss still has an impact on the scattering of the system due to it's presence within the waveguide

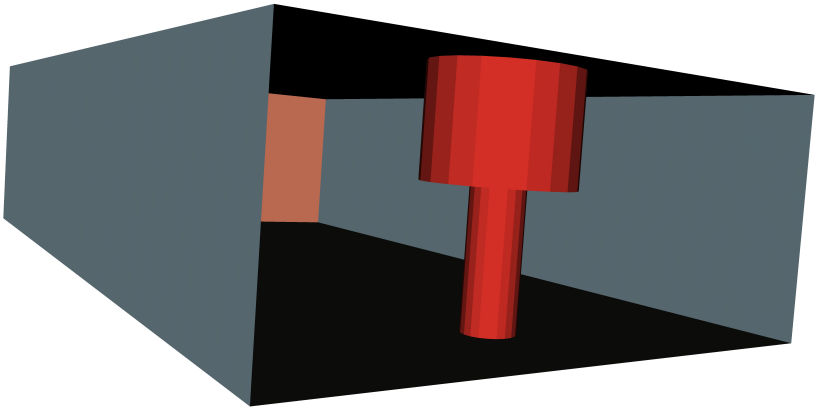

Figure 4.8: The geometry used to study the influence of including an upper boss into the waveguide.

cavity. The threaded boss is thicker in diameter than the inductive post. Similarly, the depth the threaded boss extends into the waveguide will also impact the scattering characteristics, as a larger portion of the vertical space of the waveguide will be filled by the boss.

In this subsection, two investigations will be conducted to fully study the impact of the upper boss. Firstly, the diameter of the boss will be varied in a similar fashion to the inductive post above. The penetration depth of the boss will be kept constant throughout this investigation. The second investigation will consider the insertion depth of the boss. The diameter of the boss will be set from the previous investigation and the proportion of the vertical dimension of the waveguide opening that is filled by the boss will be varied.

4.6.1 Boss Diameter Investigation

The threaded boss was added to the top of the inductive post in the waveguide as seen in figure 4.8. The diameter of the boss must always be larger than the diameter of the post, thus a minimum diameter of 3.5 mm was selected. The diameter of the boss was varied in two ways, similarly to the

post above, with large variations coming in 0.5mm increments and finer changes explored using variations of 0.1 mm. As before the inductive post was placed centrally in the waveguide, with the diameter of the upper 2 mm thickening to generate the upper boss. The meshing parameters have remained constant throughout the simulations run in this chapter.

Figures 4.9,4.10 illustrate the s-parameter response of the system with the inclusion of a boss and varying its diameter.

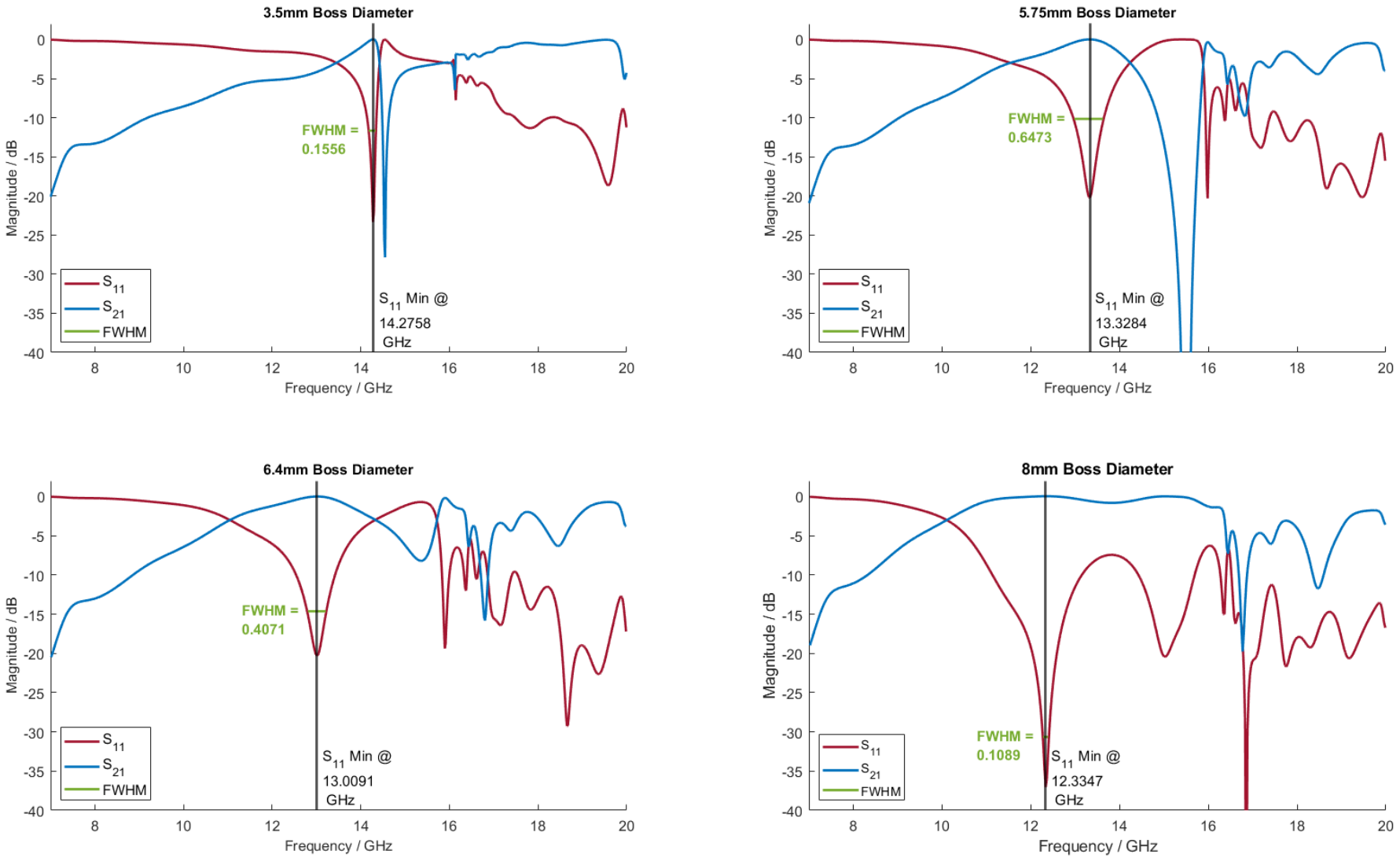

Figure 4.9: The inclusion of the threaded boss into the geometry introduces a second reflection region at 15 GHz. The largest impact comes from the boss with the largest diameter, though smaller diameters are preferable in practice as they obstruct the incident wave less.

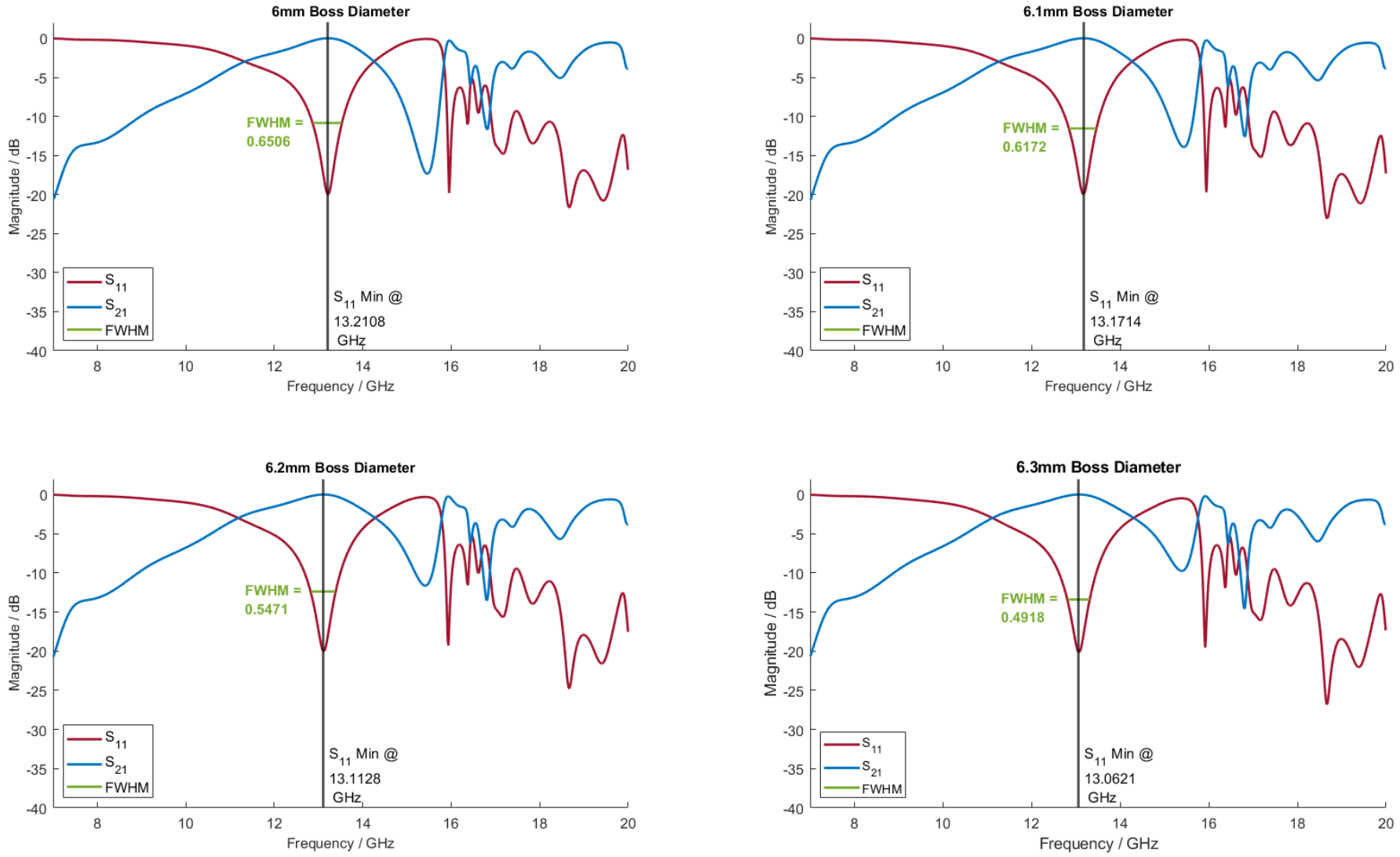

Figure 4.10: The impact on the s-parameters of fine variations in the diameter of the upper boss.

The inclusion of the upper boss introduces a transmission region at between ≈ 12 and 14.5 GHz. As the diameter of the boss increases, so does the frequency span of this region to higher frequencies, with the FWHM increasing from 0.1556 GHz for a 3.5mm diameter boss, to 0.6506 GHz for a 6mm diameter boss. When the boss diameter exceeds the threshold value ≈ 6mm, the spread of this regions starts to diminish again down to 0.1089 GHz for an 8mm diameter boss. It is worth noting that the 8mm diameter boss has another peak reflection region very close to the first (see fig 4.9) which would indicate that the reflection capabilities extend higher.

A second reflection region appears at $\approx 15GHz'$ with the inclusion of the boss. As boss diameter increases and this region broadens, extending to both lower and higher frequencies until the boss passes a threshold diameter of ≈ 6.2mm. Beyond this threshold, the reflection region diminishes again until it vanishes completely when the boss diameter exceed 8mm.

As with the post diameter, the diameter of the boss needs to be balanced to ensure optimum results. The threshold value of 6.2 mm corresponds to ≈ 1/4 waveguide width, further indicating that the dimensions of the waveguide and the components are intrinsically linked. This threshold value of 6.2 mm was selected to be used throughout the rest of this research.

4.6.2 Boss Depth Investigation

The next factor to consider in this exploration of the components within an RxP system is the protrusion of the boss into the waveguide (figure 4.11). Keeping the diameter of the boss at the previously identified value of 6.2 mm, the depth of the boss into the waveguide was explored through expanding this diameter down the length of the inductive post.

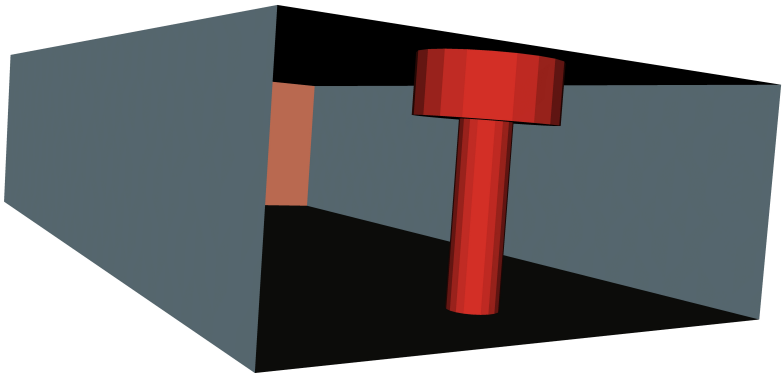

Figure 4.11: The geometry used to study the influence of extending the upper boss into the waveguide

As the boss protrudes downwards into the cavity, the path through which the wave can propagate is manipulated significantly. For small protrusions, the path is not too dissimilar to those identified in section 4.5, owing to the geometrical similarities. However, as the boss protrudes further and further into the waveguide, a greater area of the waveguide's cross-section is obscured, changing the behaviour and increasing the scattering.

The protrusion of the boss was changed in increments of 0.5 mm from 0.5mm to 7.5 mm (filling approximately 75% of the vertical dimension of the waveguide). As before, a finer exploration was conducted using 0.1 mm increments centred around 4.5 mm depth. A selection of the results are shown below in figures 4.12 & 4.13.

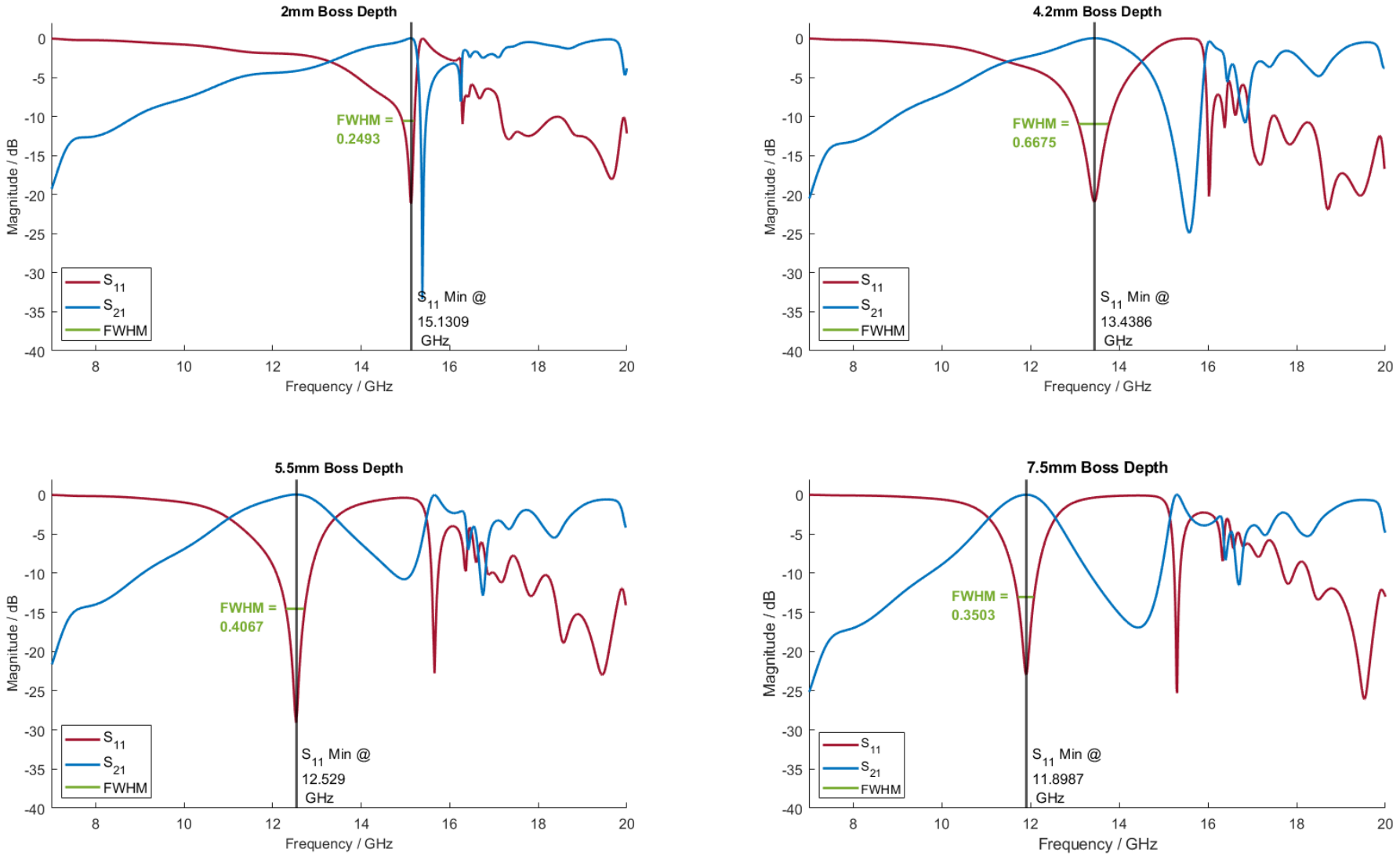

Figure 4.12: A subset of the data from the upper boss depth investigation. As the depth of protrusion increases, the upper boss causes a greater reflection response, inhibiting the propagation of the incident signal.

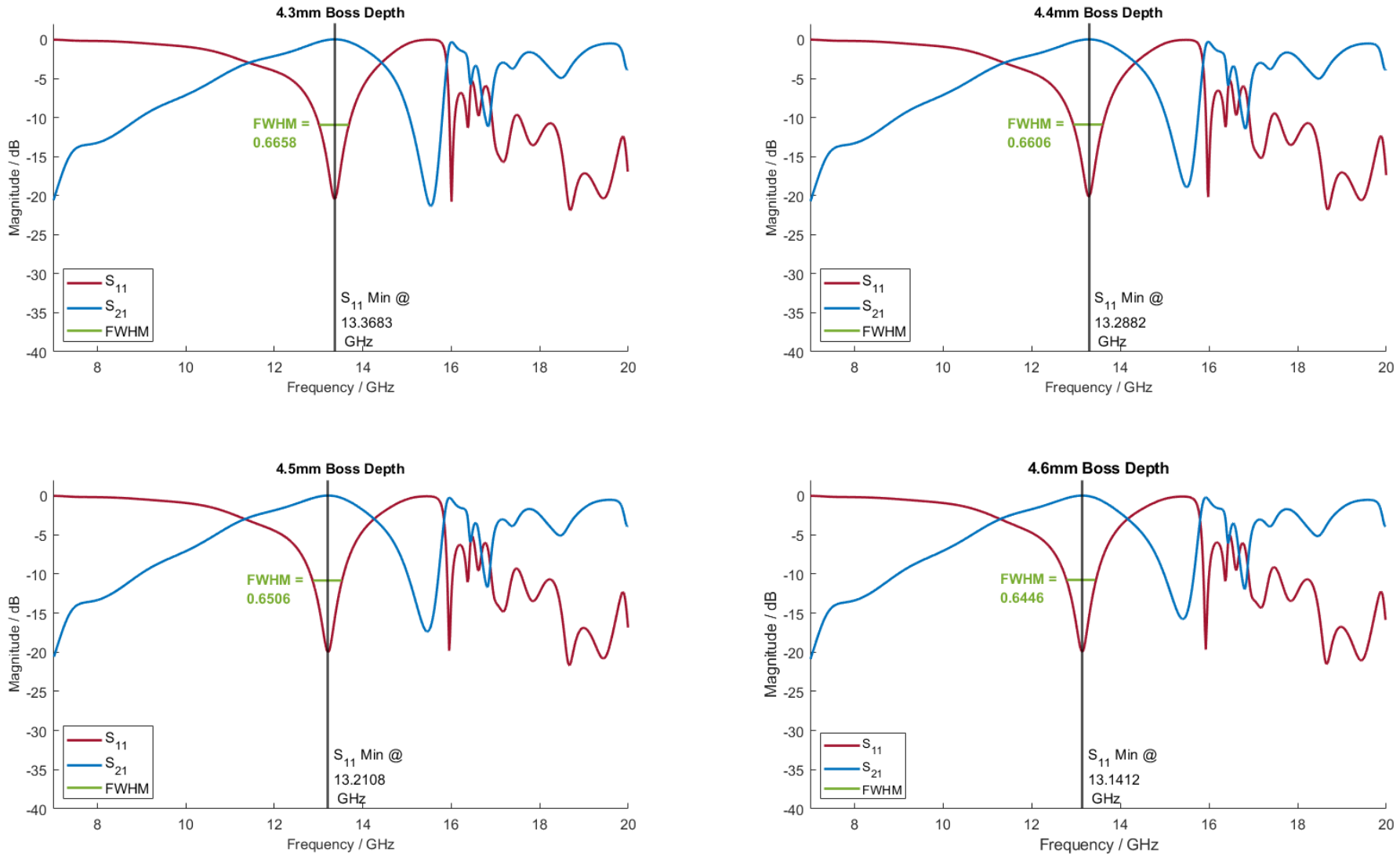

Figure 4.13: S-parameter results from simulations of the upper boss with fine incremental variations in the depth of protrusion.

As shown in figures 4.12 & 4.13, as the depth of protrusion of the boss into the waveguide increases, the frequency spread of a second region of reflection around 15 GHz increases. This region follows a clearly defined region of transmission and extends to higher frequencies as the depth increases. The maximum size of this second transmission region is seen in the largest protrusion (boss depth = $7.5mm$) which corresponds to a protrusion to approximately $^{3a}/_{4}$. This is to be expected as a greater portion of the waveguide is obstructed by the boss.

The transmission region appears between 15 GHz - 11.5 GHz depending on boss depth. The further the boss protrudes into the waveguide, the lower frequency this transmission region is peaks (see figure 4.12). As the depth of protrusion increases, the width of this maximum transmission region increases, indicated by the FWHM result increasing from 0.2493 GHz at 2mm depth to 0.6675 GHz at 4.2mm depth. Beyond the threshold of 4.2mm, the transmission region again begins to diminish, with the FWHM reducing to 0.3503 GHz.

As with the post diameter, an increase in protrusion corresponds to a greater volume of the waveguide being filled and greater scattering. Although desirable in the "On-state" where the post is grounded and the incident signals want to be reflected, such a protrusion will have a detrimental effect in the off state. For this reason, a boss depth of 4.5 mm was selected moving forward.

4.7 Adding the Lower Cavity

The final component to be investigated in this chapter is the addition of a lower cavity to the waveguide, as seen in figure 4.14. This has the double effect of allowing a longer inductive post and, when considering the threaded

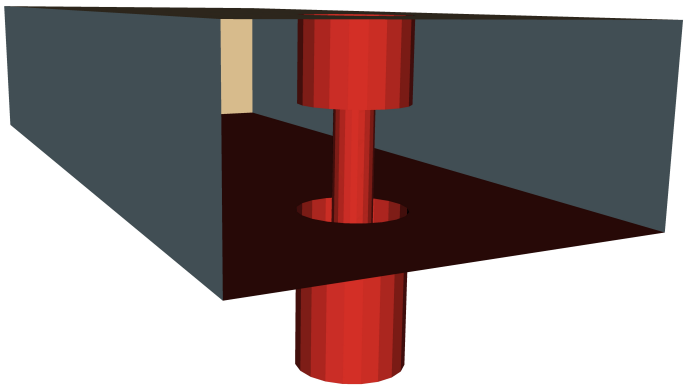

Figure 4.14: A diagram showing the geometry explored in the investigation into the addition of the lower cavity, the protrusion out of the bottom of the waveguide which houses the extended post.

boss in tandem, provides and elongated path for the incident signal to travel though. The increased path length provides a greater probability of the electromagnetic wave scattering off the RxP system.

The diameter of the cavity dictates how much free space there is around the inductive post that the wave can pass through. If the diameter of the cavity is insufficient, the wave will simply pass over the cavity, without the path length being elongated at all. This will force the wave to interact with the inductive post and could cause useful signals to be scattered, whereas these signals should pass through uninhibited. Too large a diameter and the wave will no longer be forced to interact with the inductive post, reducing the chances of scattering by the post and having a detrimental effect on the operation of the RxP system. Similarly, the deeper the cavity, the more the chances of interaction with the inductive post should increase as there is a greater surface area of the post present to the incident wave.

4.7.1 Lower Cavity Diameter Investigation

For these simulations, the depth of the cavity was varied between 3 mm and 9 mm in 1 mm increments, with finer explorations using 0.5 mm increments. The choice to deviate from the previously used 0.5 mm and 0.1 mm increments seen before is due to the presence, and diameter, of the inductive post. 0.1 mm increments correspond to increasing the diameter of the cavity by 5% of the post width and it was unlikely to see any significant behavioural shift. Similarly, increasing the diameter of the cavity by approximately $a/10$ for each incremental change will allow a full exploration into how the cavity affects the behaviour and how design can play a key role in the performance of the system.

The depth of the cavity was arbitrarily set at 5.75 mm, with the post and boss dimensions the same as outlined above and the meshing parameters remaining constant throughout this chapter. Figures 4.154.16 ,shows a subset of the simulation data from this study. It aims to encapsulate the differences observed when using the coarse and fine increments as well as demonstrate the behaviour of the system as the cavity diameter increases.

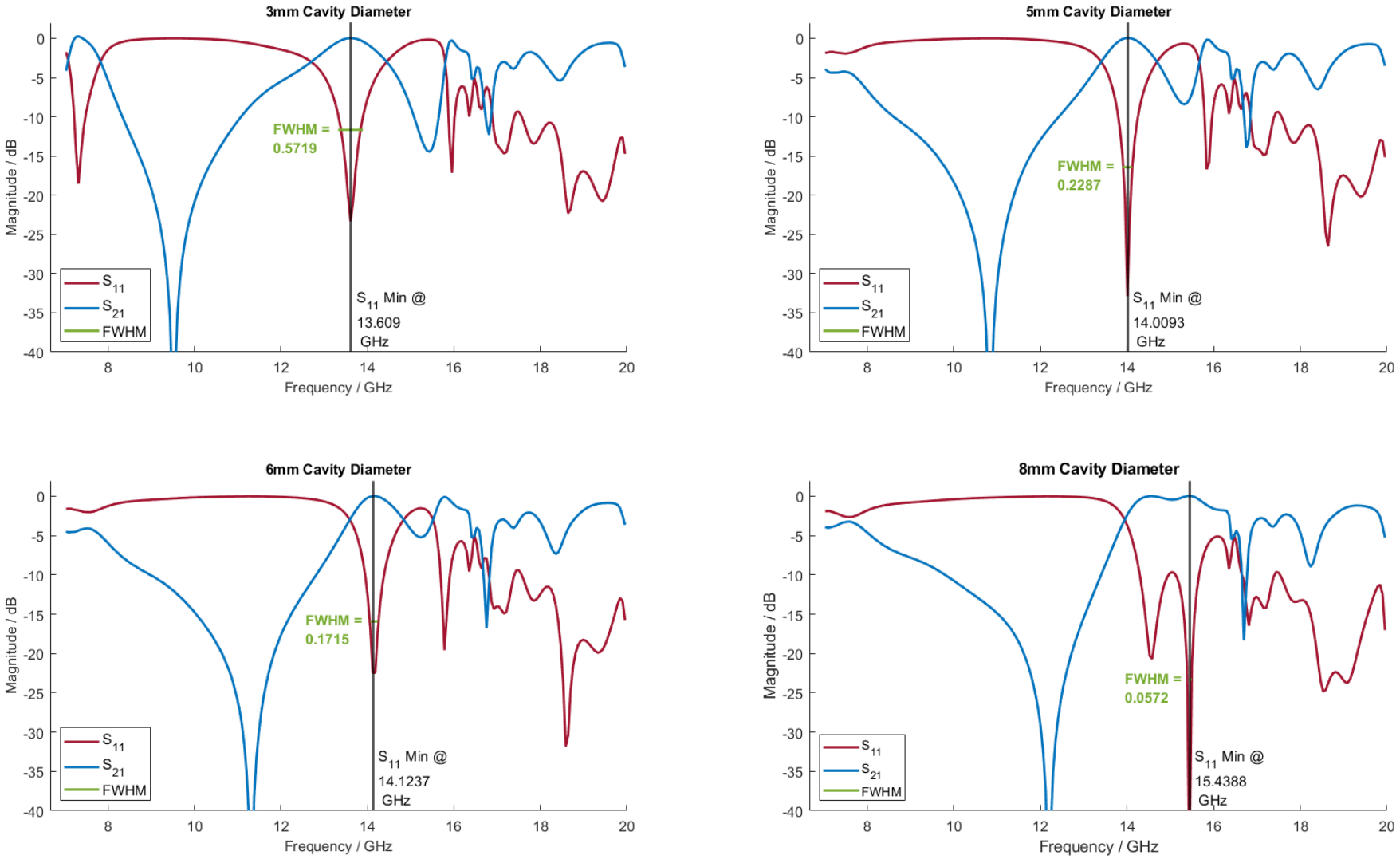

Figure 4.15: A subset of the simulation data following the introduction of the lower cavity. The primary reflection region can be seen to broaden with increasing cavity diameter and extend to higher frequencies. The initial transmission region, seen at 14.5 GHz for the smallest cavity, progresses with increasing cavity diameter to higher frequency.

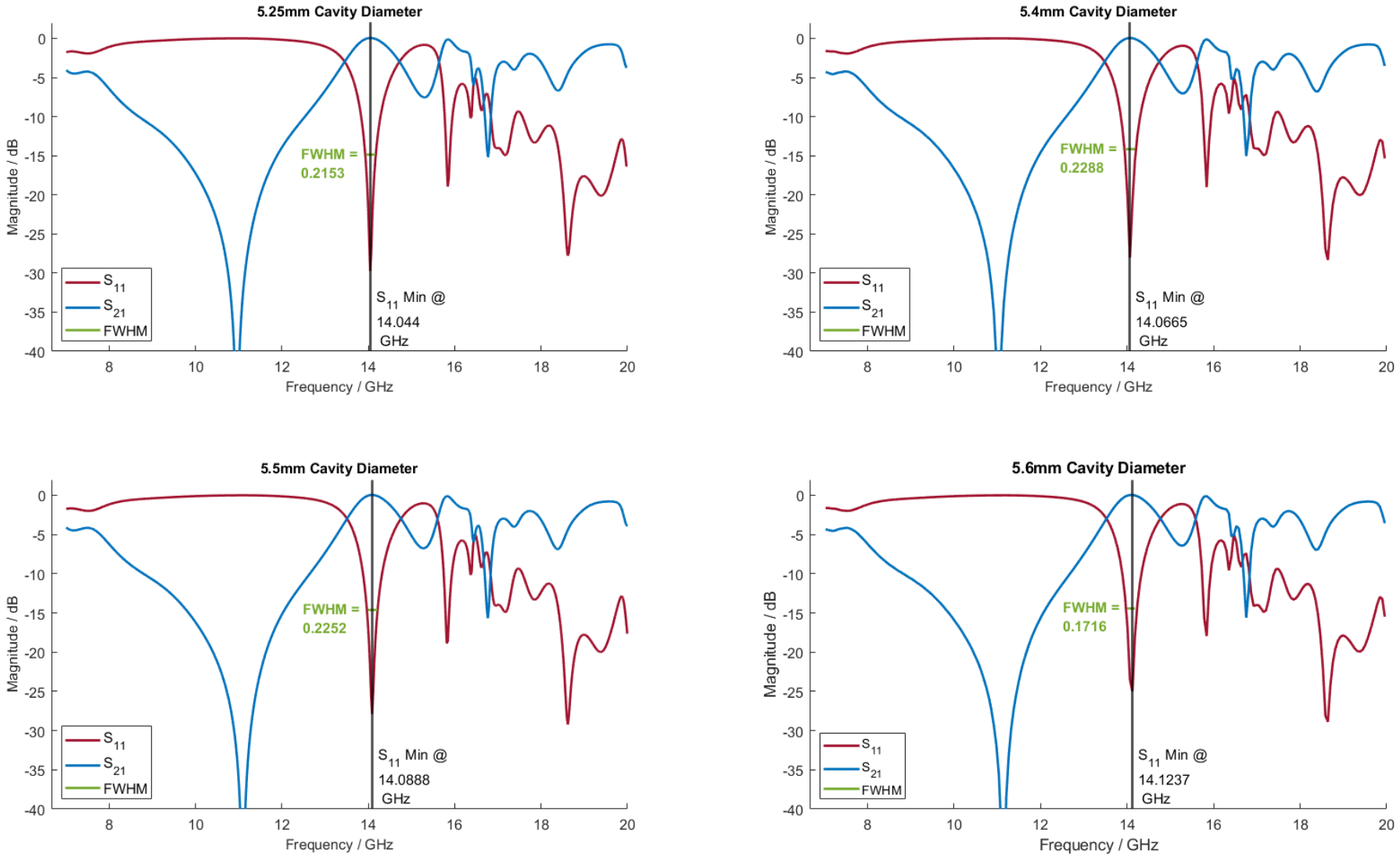

Figure 4.16: Variations in the s-parameters when the diameter of the cavity is changed by a fine increment (0.1 mm). Small variations can be observed in the broadening of the reflection region and the procession of the initial transmission region to higher frequency

Figures 4.15,4.16 show that the inclusion of the cavity, increases the cross-section of the interaction between the post and the propagating wave. It does this in two ways, initially by increasing the path length of the wave so that it interacts with more of the post, and secondly by creating a well where, through repeated reflection off of the cavity walls, repeat interaction and scattering can occur. This can be seen by the broadening of the initial reflection region to higher frequencies as the cavity diameter increases.

As the cavity diameter increases from 3mm, the FWHM of the transmission region begins to reduce from 0.5719 GHz to 0.1715 GHz with 6mm diameter. The transmission region remains within $\approx$ 0.5 GHZ across all diameters in this range. As the diameter of the cavity is increased to 8mm, the transmission region broadens again. Although the FWHM of the peak region reduces further (to 0.0572 GHz), figure 4.15 shows that there is a second peak adjacent to the largest, broadening the transmission response. This increased transmission response is likely due to the cavity being > 3 times wider than the inductive post, creating a clearer, unimpeded path for the incident wave. Figures 4.16, 4.15 suggest that the width of the maximum transmission region is minimised with a cavity diameter between 5.6mm and 6mm. For the remainder of this research the cavity diameter was selected to be 5.5mm.

4.8 Other Components

As mentioned in previous pages, the RxP system is an intricate combination of many components working in unison to provide a desirable response to incoming electromagnetic waves. Aside from the components discussed here, there is often also the inclusion of layers of PTFE tape. This tape is not always present as it is used to tune the final device so that the response

of the system is optimised at the frequencies of interest. For this reason, it has not been included in this research.

The inclusion of the PiN diode and the associated diode package, bonding ribbons and mounts is discussed further in chapter 7. The presence of the diode fixed to the end of the inductive post provides the RxP system with the switching behaviour that is crucial for it's operation.

The results of this chapter provide an insight to how the behaviour of the RxP system can be impacted by the presence and dimensions of a few key components. The next chapter will delve into the basics of semiconductor physics with a particular focus on PiN diodes. This will aim to provide the foundational knowledge required to better understand how the PiN diode modelled in this research works, why it is important that it is modelled correctly and what causes the effects observed in practical systems.

Before implementing the model of the semiconductor PiN diode, it is advantageous to revisit the theory behind semiconductors and PiN diodes and discuss current modelling techniques for PiN diodes. Chapter 5 introduces the required semiconductor physics, whilst chapter 6 discusses current diode modelling techniques and aims to place the need for this model development in the wider RF modelling environment.

Chapter 5

Semiconductor Physics and PiN Diodes

This chapter will address the physics behind semiconductor devices, with a particular emphasis on the PiN diode for RF applications. It will start by presenting the physics behind semiconductors and PiN diodes before entering into more detail around the constituent parts of a PiN diode. The properties of each of the P, I and N layers will be considered, including doping levels, band structure and mobility, where the electrical conductivity will be calculated from the electron and hole mobility. Finally, a discussion of the different uses and applications of PiN diodes will be presented, with consideration also being given to the significance of other materials within the PiN structure.

5.1 Semiconductor Physics Basics

Semiconductors are of enormous technological importance in the modern world. By exploiting the electron energy levels within the atomic struc-

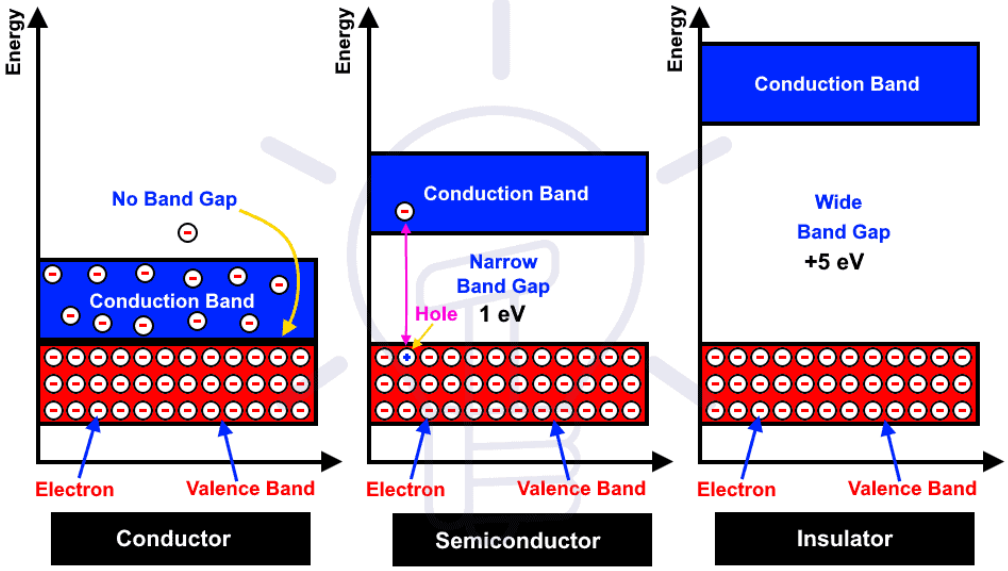

Figure 5.1: An illustration showing the valence and conduction bands within a semiconductor, along with the energy gap (bandgap) which electrons must be excited across for the semiconductor to exhibit conductive behaviour. In addition to the band structure of a semiconductor, the image also shows the band structure of conductors (left) and insulators (right) giving some insight to how the band structure of these materials determine their electronic behaviour, with the smaller band gap facilitating easier electron flow [71].

ture, it has been possible to find and create materials that are not fully conducting, nor fully dielectric in certain conditions.

At room temperature, semiconductors have an electrical conductivity between a dielectric and a metal. The nature of this behaviour stems from the energy gap between the bands in the atomic structure. Metals have partially filled bands of electron states, allowing current (the flow of electrons) to pass easily through them. Dielectrics, on the other hand, have filled bands and the energy gap, E_g, between the highest energy filled band (the valence band) and the next highest energy band that is empty (the conduction band) is large, large enough that electrons typically do not have sufficient energy to traverse the gap, as shown in figure 5.1. In a semiconductor, this energy gap is relatively small, so despite having completely filled bands, if the electrons are adequately excited, they can cross the gap, manifesting a current flow through the semiconductor.

There are two main types of semiconductor - intrinsic and extrinsic. intrinsic semiconductors (also known as pure semiconductors) are behave in the same way as a dielectric material at zero temperature. But as the temperature increases and the electrons in the valence band are excited, they cross the relatively small bandgap. This results in the conductivity of intrinsic semiconductors increasing rapidly with temperature, unlike metals where the conductivity typically decreases with increasing temperature (due to the phonon interaction caused by electrons scattering off of the vibrating lattice).

Extrinsic semiconductors have been modified in a controlled manner to alter their behaviour to make them more useful in their given application. Using a process called doping, impurities are added into the semiconductor to change the dominant charge carrier of the semiconductors conductivity. By adding donor impurities into the material, the excess of electrons in the material causes the conductivity to be dominated by electrons occupying states near the bottom of the conduction band, forming an n-type semiconductor. Similarly, p-type semiconductors have an excess of holes, provided by the addition of acceptor impurities in the material, thus the conductivity of p-type semiconductors is dominated by holes occupying states near the top of the valence band.

The inclusion of these dopants can have a significant effect on the behaviour of the semiconductor. One of the more prominent and useful applications of doping is to practically remove the temperature dependence of the conductivity of the material. The vast majority of semiconductor devices in use today are based upon extrinsic semiconductors.

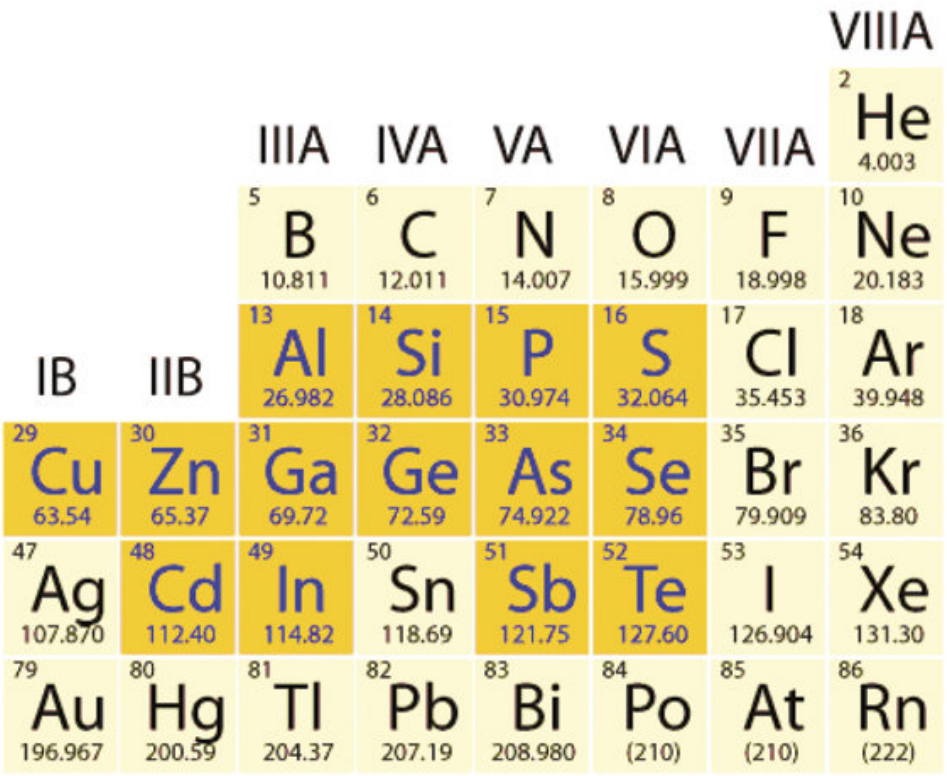

Figure 5.2: An excerpt from the periodic table of elements showing the more common elements used in the formation of semiconductor devices. At the top of each column is also their group, useful for determining which elements are often combined to form semiconductor devices [72].

5.1.1 Doping Levels

As we have seen above, the vast majority of semiconductor devices and applications utilise extrinsic semiconductors. The careful control of the number and type of charge carriers, through the deliberate inclusion of impurities, allows a diverse range of characteristics and uses to be achieved. The process of including these impurities is known as doping and is what gives the semiconductor its excess of electrons or holes in the valence band. Frequently, it is elements from group IV and group V (as seen in figure 5.2) that are combined to form extrinsic semiconductors. When combining elements to form a semiconductor, the dopant or impurity - the element that has carefully controlled singular atoms added - is added to the lattice

structure of the "parent" element to form the semiconductor compound.

By substituting an atom in an intrinsic semiconductor (such as silicon from group IV) with an element from a higher group (for example the group V element phosphorous), the semiconductor compound will have an excess of electrons, giving it a negative charge. Semiconductors with an excess of electrons are known as n-type semiconductors. Group V elements are commonly used as dopants and all characterised by a valency of five, since they have 5 electrons in their outer shells [73]. Another feature of this process is the similarity in atomic size and electronic structure of the elements involved. The phosphorous atoms are similar in size and electronic band structure to their silicon counterparts, meaning that the substitution of one atom for another in the lattice structure is possible without any significant difficulty. The phosphorous atom only needs four of its five valence electrons to form covalent bonds with their neighbours. The fifth valence electron that is not tightly bound is free to orbit the positively charged impurity atom and behave similarly to the Bohr model of a hydrogen atom, i.e. orbiting the atom in a stable orbit of a distinct energy level to avoid radiation.

Another pair of commonly combined elemental groups are group III and group IV, which, when combined, form p-type semiconductors. The group III elements have a deficiency of electrons when compared to group IV elements. This deficiency of electrons manifests itself as an excess of acceptor sites, often referred to as holes. The p-type impurities, that is the atoms from the elements with an excess of holes in the valence band, would "accept" a valence electron from another atom, hence why they are referred to as "acceptor impurities". P-type impurities are characterised by three electrons forming covalent bonds with the neighbouring atoms in the parent element, leaving a vacancy. At 0K, the vacancy is not a hole, however when some temperature is added, an electron from the valence

band fills this vacancy, resulting in a hole in the valence band [73].

By carefully managing the insertion of p- and n-type impurities, the electrical characteristics of the semiconductor can be controlled to suit the needs of the device. In general, an increase in the doping level of the material leads to an increase in the materials conductivity, since there are more charge carriers available. Doping changes the band structure of the material, bending and shifting the energy bands relative to the Fermi level, thus changing the thermal dependency of the device. In many electronic applications this is highly important. It is undesirable (and can cause significant problems to the device's health and operation) if the electromagnetic behaviour of the device were to change appreciably with temperature, so doping in semiconductor materials is often used to "tune out" this response.

5.1.2 p-n Junctions

Having already discussed p-type and n-type semiconductors, attention now turns to the pn junction, a region in a semiconductor material where p-type and n-type semiconductor interface within a single crystal. Through careful ad selective doping it is possible to have a region of p-type semiconductor adjacent to a region of n-type semiconductor, however in practice the interface is not perfectly abrupt. The transition region between the n-type and p-type semiconductor is often small enough that it can be approximated to an abrupt interface.

The reason that an abrupt interface is impossible in practice is that a pn junction cannot be formed by bringing a piece of n-type semiconductor and placing it next to a piece of p-type semiconductor. Instead, the doping of the whole material needs to be done to create the p- and n- regions adjacent to one another in the same material. However, when

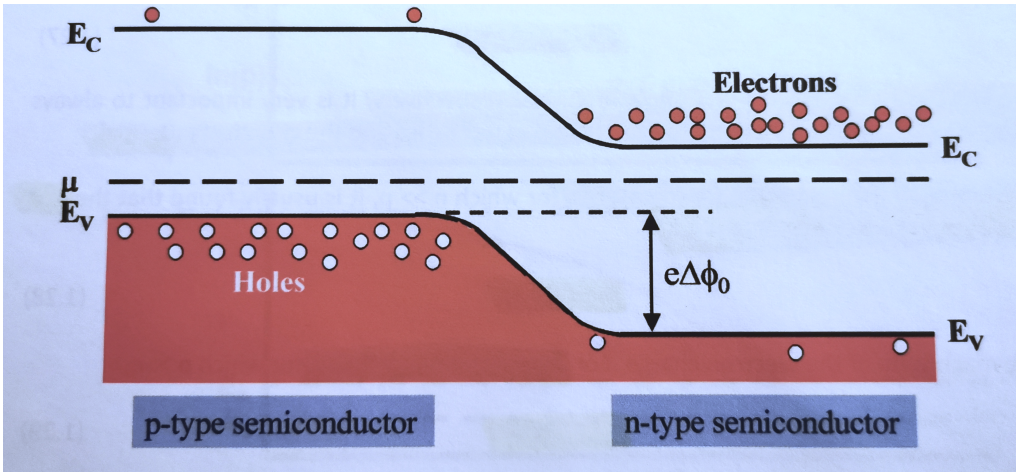

Figure 5.3: A diagram showing the pn junction of a semiconductor material. The excess in holes in the p-type semiconductor causes the valence band of the semiconductor to rise in this region and be close to the chemical potential, with the n-type semiconductor and the excess of electrons pulling the conduction band down towards the chemical potential. The bending of the energy bands is due to the dynamic equilibrium, with the bending in the bands also causing an electrostatic potential difference of $e\Delta\phi_0$ between the n- and p-type regions, resulting in an electric field in the interface region [74].

understanding the nature of a pn junction, it can be advantageous to imagine this scenario. The chemical potential, μ of the n-type semiconductor lies below the bottom of the conduction band and close to the donor level. Similarly, for the p-type material, μ is above the valence band and close to the acceptor level. When these two materials are placed adjacent to one another, a electrons will diffuse from the n-type semiconductor to the p-type semiconductor filling the empty states in the valence band.

The result of this diffusion of electrons is that the energy levels in the bulk of the p-type semiconductor have now risen with respect to the n-type semiconductor, causing the valence and conduction bands to "bend" across the junction (see figure 5.3). The reason for this bending in the band structure is to ensure that the chemical potential of the material is constant throughout the junction, resulting in a net electrostatic potential difference across the junction.

Once the electron drift current (the movement of electrons through the semiconductor due to the electric field) and the electron diffusion current (the movement of electrons in the semiconductor from one on type to

the other) are equal an opposite, a dynamic equilibrium is reached which manifests in the bending of the energy bands seen in figure 5.3. The electric field in the p-n junction region results from the potential difference caused by the bending of the energy levels. The bending of the energy levels causes a potential difference (voltage) between the p-type semiconductor and the n-type semiconductor of $e\Delta\phi_0$, generating an electric field in that region. When in this state of dynamic equilibrium, there is no net current flow if there is no external voltage applied.

When the junction is in equilibrium the two main current sources across the junction, the generation current and the recombination current, are equal in magnitude and opposite in direction:

$$J_{gen} + J_{rec} = 0 \tag{5.1}$$

The generation current (J_{gen}) is the rate of production of electron-hole pairs. This occurs at a low rate, but if it occurs in the depletion region, the hole and the electron are drawn apart rapidly by the electric field that is present. The generation current is therefore a negative current that flows from the n-side to the p-side, given by:

$$J_{gen} = -Aexp\left(\frac{-E_g}{2k_BT}\right) \tag{5.2}$$

where A is a positive material constant which is weakly dependent on temperature.

The recombination current (J_{rec}) is in some ways the opposite of the generation current. It is a positive current flow created by charge carriers (electrons and holes) having sufficient thermal energy to overcome the electrostatic potential energy barrier ($e\Delta\phi_0$). This means that electrons in the n-type region have sufficient energy to move to the p-type region and re-

combine with a hole. It also results in holes having enough energy to cross from p-type to n-type regions and recombine with electrons. With the introduction of another weakly temperature dependent positive material constant, B, the recombination current can be written as:

$$J_{rec} = Bexp\left(\frac{-e\Delta\phi_0}{2k_BT}\right) \tag{5.3}$$

Although ever present, these currents are small compared to when an external bias voltage is applied across the p-n junction (such as can be found from the interaction between the EM wave and the inductive post in this research). When an external voltage, V, is applied across the p-n junction, there will be a net current flow. The most useful scenario is when junction is forward biased, that is when the p-type region is biased positive with respect to the n-type region, which allows the current to increase exponentially. In this situation, the generation current remains almost unchanged, but the recombination current increases to:

$$J_{rec} = Bexp\left(\frac{-e\Delta\phi_0 - V}{2k_BT}\right) \tag{5.4}$$

In the forward bias condition, when $eV >> k_BT$ the current increases exponentially. However, in the reverse bias, the current saturates at the value of the generation current.

5.2 PiN Diode Basics

The PiN diode uses the physics of the p-n junction to make much more useful devices for a number of applications. Recall that the doping process can be very well controlled, allowing specific regions to have their characteristics controlled by the amount of dopant added to the parent

semiconductor. This allows the electronic properties of a material to be very carefully engineered through the use of p-layers, n-layers and I-layers.

5.2.1 P, I, N layer definitions

A PiN diode normally consists of three distinct, semiconductor layers. The first layer is the p-layer discussed above, a layer of the parent semiconductor that has been doped with acceptor atoms, giving them an excess of holes.

In the middle lies the I-layer, also known as the intrinsic region. The I-layer is a region of undoped parent semiconductor. This layer can take a range of thicknesses depending on the desired electronic properties of the device. This is the region that causes the change in properties when compared to a typical p-n junction. In most PiN diodes, this layer is very thin, with the intrinsic region thickness often measuring less than 200 μm.

Finally, the bottom layer of the PiN diode is a layer of parent semiconductor doped with the donor atoms. This n-layer has an excess of electrons that, if the applied voltage is large enough, will have sufficient energy to traverse the band gap into the valence band.

In practice, this switching bands does not manifest in the form of a singular electron passing through the entire I-layer into the p-type semiconductor. Rather it is the displacement of a series of electrons across the atoms between the n-type and the p-type semiconductors that allows a small flow of electron current, a recombination current addressed earlier, with the result being the filling of one hole by one electron. Similarly, it is unlikely that only one electron will be sufficiently excited to recombine, thus the recombination current will be higher than simply one electron.

5.2.2 Electrical Conductivity from Hole Mobility

In an RxP system the most interesting property of the PiN diode is the electrical conductivity. This can be calculated from the electron and hole mobility of the doped elements themselves.

The electrical conductivity of a semiconductor is given by the equation:

$$\sigma_E = e\left(n\mu_e + p\mu_p\right) \tag{5.5}$$

where μ_e and μp are the electron and hole mobilities respectively, with n and p representing the electron and hole concentrations. Assuming, that the electrons and holes are silicon atoms:

$$\mu_e = 1,400 cm^2/(V.s) \tag{5.6}$$

$$\mu_p = 450 cm^2/(V.s) \tag{5.7}$$

And taking the electron and hole doping levels to be:[75]

$$n = 2 \times 10^{19} cm^{-3} \tag{5.8}$$

$$p = 4 \times 10^{19} cm^{-3} \tag{5.9}$$

The electrical conductivity can be found to be:

$$\sigma_E = 1.6 \times 10^{-19}\left(2 \times 10^{19} \cdot 1400 + 4 \times 10^{19} \cdot 450\right) \tag{5.10}$$

$$= 7360 \tag{5.11}$$

$$= \mathbf{7.36 \times 10^5 S/m} \tag{5.12}$$

This is significantly less than that of pure gold for example, but far higher than undoped Si. The significance of this is evident when a current is applied across the semiconductor region. As previously discussed, if the current is large enough, the electrons will be accelerated across the band gap to recombine with the holes, thus a higher electrical conductivity is ideal. When the electric field of the incident signal is incident on the semiconductor, the generated current causes conduction across the band gap, in turn generating an opposing electric field and cancelling out the signal.

5.3 PiN Diode Uses and Applications

PiN diodes and p-n junctions have a plethora of uses in modern technology. Solar cells rely on the photons from the Sun having energy greater than the semiconductor band gap. If the photon has sufficient energy, an electron hole pair is produced, which is then immediately pulled apart by the strong electric field in the depletion region. This creates the current which is used to charge batteries, power homes etc.

LEDs have grown in popularity and are almost exclusively used instead of traditional light bulbs. The recombination process involves the emission of photons at specific frequencies. Therefore, the p-n junction can be used to make efficient light emitting diodes (LEDs) and careful engineering of the band gap can allow the frequency of the emitted photon to be dictated.

One of the most common uses for a semiconductor PiN diode is as an RF switch and rectifier. The current-voltage characteristics of p-n junctions are very asymmetric between both the forward and reverse biases, making them excellent diodes [74]. In the RF setting, this asymmetry allows for a

switching behaviour when the incident has adequate power to switch the diode from reverse to forward biased, and in the case of an RxP "switch on" the on-state behaviour that protects the receiver. Given their highly manipulatable nature, they are well suited to a number of applications in this sector.

5.3.1 Semiconductor Materials

Commonly, silicon (Si) is used in the formation of semiconductor devices. Silicon is an example of an elemental semiconductor, meaning that pure silicon itself is a semiconductor. Silicon is by far the most technologically important semiconductor, owing to its stability, abundance, inexpensiveness and flexibility. Silicon can be formed into large crystals, frequently very pure, processed into extremely small structures on the scale of microns and below (nanostructures), and can be easily doped. It is very common for silicon to be doped and used in both the p- and n- layers of a PiN diode, often with undoped silicon forming the intermediate layer between them.

Depending on the desired application, financial considerations and fabrication process, other elemental compounds may be used to form semiconductor devices. Another of the more frequently seen combinations is Gallium-Arsenide (GaAs). Some of the electronic properties of GaAs semiconductors are more useful than their Si counterparts, such as the increased frequency range of operation, wider energy band gap leading to less noise and a greater insensitivity to overheating. However, given the relative abundance of silicon, one benefit of Si semiconductor devices is that they are often cheaper and easier to manufacture than their GaAs counterparts.

Building upon the GaAs semiconductor devices, Aluminium Gallium Arsenide semiconductors combine GaAs semiconductor structures with

AlAs (aluminium Arsenide) semiconductors. AlGaAs semiconductors are have a special use in red and near-infra-red emitting laser diodes. [76].

The next chapter will take a thorough look at how these devices are modelled in the literature and research. Given their non-linear nature, modelling semiconductors often causes difficulty in industrial simulations. A number of different approaches have been taken to achieve this, with success across a number of different fields.

Chapter 6

PiN Diode Modelling Techniques: A Review

This chapter presents a brief overview of the history of modelling small electronic components, with a later focus on PiN diodes. Initially, the equivalent circuit representation will be introduced, followed by the development of the transmission line modelling method (TLM). Then, a discussion will be made regarding the modelling of complex electronic components and the commonly used modern day methods, where a few applications and examples will be provided. Finally, a case will be made for using UTLM to model these components and why it may be advantageous when compared to other modelling methods. This discussion will also address ways in which UTLM may be used together with one of the modern day methods and the reasoning on the decision to proceed with solely UTLM will be given.

6.1 EM Fields and Equivalent Circuits

In the middle of the twentieth century, whilst considering ways to simulate the performance of rotating electrical machinery, Gabriel Kron realised that "by ignoring the very alive phenomena underlying the lifeless symbols [In physical equations and calculus]... it is not possible to form a correct physical picture, much less build a physical model that corresponds term by term to the equations" [77]. Kron then proceeded to develop an equivalent circuit to represent Maxwell's equations for EM fields (see [77, 78]) that are capable of accurately describing the interactions of the field whilst allowing for variation in frequency, homogeneous and non-homogeneous fields and isotropic or non-isotropic fields. By considering tensors, Kron was able to rewrite the Maxwell equations in a form that allowed the electric and magnetic field components along the three directions of the orthogonal curvilinear co-ordinate system to be represented by voltages and currents in impedance elements. The values of these elements depend only upon the permeability, permittivity and conductivity of the propagating medium and the size of the infinitesimal cube of space being replaced by the network. Thus the network represents space rather than any particular wave mode or frequency [78], allowing for a more complete simulation and understanding. This allowed the propagation of the EM wave to be modelled as an "Equivalent Circuit" with voltages, currents, inductances and capacitances each describing the progression of the wave through the system and the interaction of the wave with any discontinuities present. In accompanying works, Whinnery et al. [79, 80, 81] discussed how the equivalent circuit technique developed by Kron could be used to solve a number of problems involving EM fields. They then went on to test this, using this technique to preliminarily solve some high-frequency field problems involving waveguides of a variety of shapes, both with and without discontinuities, and

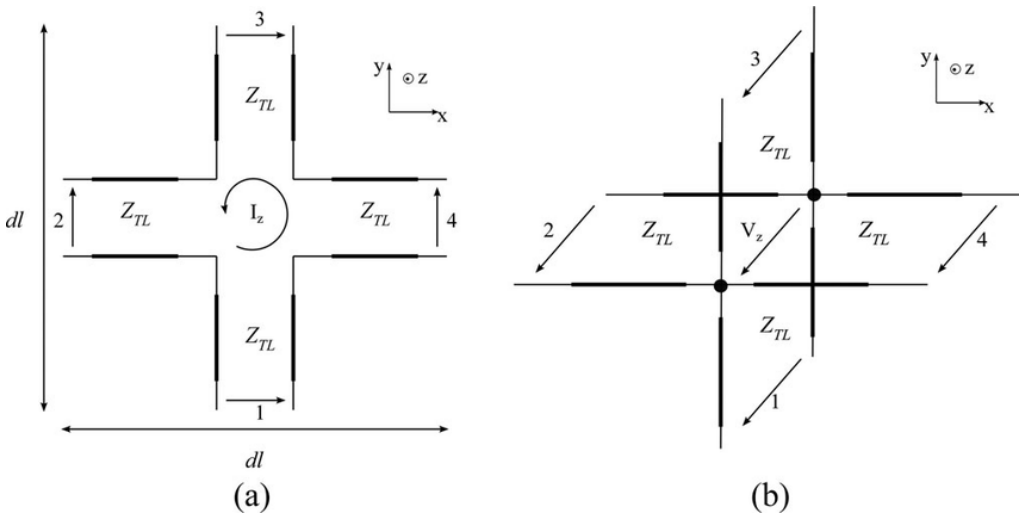

Figure 6.1: (a) A series node in TLM, (b) a shunt node in TLM. Each of these nodes is used to form free space in 2D TLM or combined to generate the expanded TLM node used for TLM modelling in 3 dimensional space. This allows all 6 of the field components to be realised [54].

other cavity resonators, as well as verifying the accuracy of the equivalent circuit method using a network analyser [80]. These works, with the basis provided by Kron, provide the foundations of one of the most commonly used techniques in modern microwave modelling - the Transmission Line Matrix Method (TLM).

6.2 The Development of TLM

In the early 1970s, the nascence of TLM occurred when the equivalent circuit modelling method was elaborated upon to discretize the problem space into lumped circuit components. These were represented by transmission line segments - ensuring the problem is therefore also discrete in time. In 1971, Johns and Beurle took the first significant steps into the development of TLM by introducing the "shunt node" as the basic structure for 2 dimensional modelling [16, 82]. As discussed previously in section 3.2.4, the TLM method is based on the analogy between electric circuits and EM fields. In the 2 dimensional form, free space is modelled in TLM using the

series node (figure 6.1(a)) and the shunt node 6.1(b)). The series and shunt nodes are identified by their relationship with the characteristic impedance of free space, Z_0, the series node having a transmission line impedance of $Z_{TL-Series} = \frac{Z_0}{\sqrt{2}}$, and the shunt node having a transmission line impedance of $Z_{TL-Shunt} = \sqrt{2}Z_0$ [54]. It uses these nodes to formulate a network model of Maxwell's equations in terms of scattering impulses [83].

The TLM method relies on a three part algorithm evaluated at each node. This algorithm is described in detail in [84]. Each node is excited at time-step k by an incident voltage pulse, combined with any reflected voltages from other nodes. This signal is then scattered by the node, where the reflected pulses are computed. The nodes form a network and each is connected to its neighbouring nodes through one of 4 ports. The scattered signals are then passed through one of the 4 ports (for 2D TLM) to the next node, where they form part of the incident voltage pulse for time-step *k+1*.

Johns, with input from Rowbotham and Akhtarzad, used this new method (TLM) to perform a comprehensive analysis of EM fields through a rectangular waveguide (both homogeneous and inhomogeneous) in a wide variety of different configurations (see [85, 86, 87, 88, 89]). In these works he postulated that the TLM method was superior to other methods of the era (including finite element and finite differences), particularly when considering the storage requirements throughout the calculations. Further comparisons were drawn between TLM and the finite difference method in a later work (see [90]), where Johns illustrated that TLM could be used in a specific manner to emulate the finite difference method, though TLM provided more information and required less storage. He suggested that, since TLM is a physical model and finite difference a mathematical model, each complement the other, each method helping to lead to a better understanding of the other [90].

Similar to its predecessor, the equivalent circuit method, Johns and Akhtarzad used the new TLM method to solve Maxwell's equations, where they also illustrated that a general 3 dimensional medium may be represented by a simple model made up of 2-dimensional nodes [91]. The creation of the expanded TLM node allowed 3-Dimensional problems to be solved more easily by combing the shunt nodes with series nodes (both of which are shown in figure 6.1) to allow all 6 field components to be described in space [16]. By placing a shunt node in each of the co-ordinate planes, the voltages across which represent the components of the E-field, and a series node in each of the planes with currents representing the components of the H-field, the geometry of the 3-dimensional problem is defined [92].

A series of publications by P.B. Johns and S. Akhtarzad soon followed, making use of the new TLM method for a variety of applications, illustrating how it can be used to describe the behaviour of EM fields though different systems including Microstrip lines [93] and Microwave cavities [92]. The computational implementation of TLM was published in 1976 [94] and in 1977, the value of TLM in the classroom was highlighted when Lohse noted that it could be used computationally as a valuable tool to teach transient fields[95].

6.3 Expansion of TLM

Further improvements were made to TLM when the node structure was expanded. Initially, the node was expanded into 3 dimensions by interconnecting a series of 2-Dimensional shunt and series nodes [91], as mentioned above. Conventional three-dimensional TLM networks require three shunt and three series nodes to represent a single cell [96], however it was noted that this caused the topology to become quite cumbersome, which had a

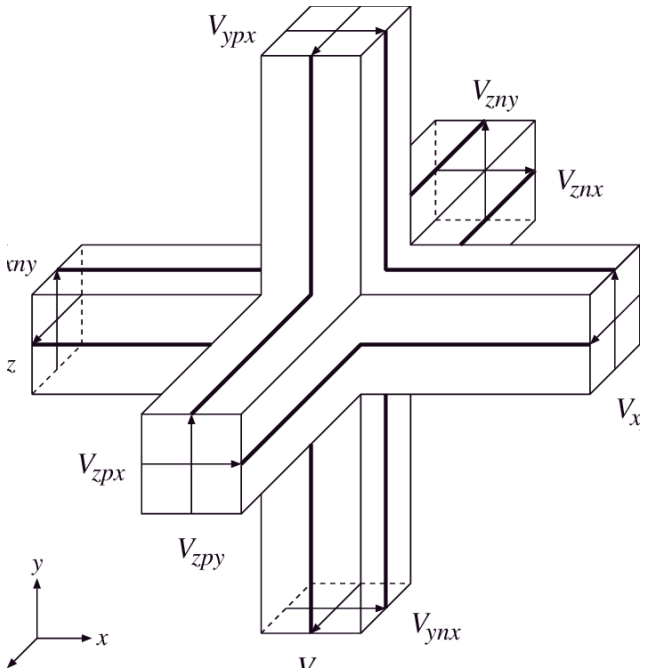

Figure 6.2: A Symmetrical Condensed Node, used in 3D TLM to calculate and propagate the electromagnetic field components in space [55].

serious detrimental impact on data preparation, particularly when using automatic data preparation schemes [55]. This led to boundary modelling becoming troublesome and liable to errors. These problems with the expanded node network were initially overcome by Saguet and Pic with the development of the condensed node structure [97, 55]. Despite being asymmetrical, this new condensed node, along with some other modifications [98] had a much simpler topology than the expanded node, ensuring that all the scattering processes for the node took place at a single point in space, and boundary conditions are simpler to apply, since they are now applied either at the node or halfway between nodes [55].

The new "symmetrical condensed node", shown in figure 6.2 is itself a further refinement of the condensed TLM node, is now exclusively used for 3-Dimensional modelling in TLM [16], removed the disadvantageous asymmetry of the previous node, allowing the field components to be condensed to one point in space [55, 99]. Furthermore, the new node intro-

duced the advantage that three of the 6 field components are defined and available at each node, whereas in other methods, only one was possible, thus vastly reducing the computational expenditure vs previous iterations. The symmetrical condensed node cannot be represented by a lumped circuit and so departs from the equivalent circuit method, though the analogy of transmission lines (particularly the two-wire non-coupling transmission line) still remains [55].

The symmetrical condensed node (without stubs) comprises of 12 ports, with each incident wave interacting with a multitude of ports depending on the properties of the field, with the direction of propagation indicating on which port it is incident, and the direction of the components of the field (e.g. E_x or H_z) determining which subsequent ports it is scattered into. By adding in 6 stub ports, one for each component of the E-field and H-field, it is possible to add capacitance and inductance to the node. Each individual component of the E-field and H-field will only couple to and scatter into certain nodes, meaning that for a uniform field, it is easy to predict the directional scattering at each node.

After "extensive and exhaustive" testing, Johns et al. found that this new node was more accurate, easier to use [55], and compares computationally favourably to finite element and finite difference models [96] - a trait of significant importance in this time as computers were in their infancy and parameters such as storage could be a real problem. More recently, TLM has been and continues to be expanded and applied extensively to solve all manner of EM field, diffusion and network problems across many engineering and science disciplines [100, 16].

6.4 Non-Linear Component Behaviour

As numerical modelling developed, it became an invaluable tool. Two methods proved to be more popular for solving EM problems in the time-domain, owing to their efficiency and accuracy; TLM and the Finite Difference Time Domain method (FDTD) [101], although the equivalent circuit method was often still used as a prerequisite for an efficient computer aided design (CAD) [67]. One particular problem that these modelling methods needed to overcome was the handling of non-linear and active components within the circuit (such as tunnel diode oscillators and pn- junction diodes). By the mid 1990s, only a limited number of approaches had been published, many of which were based on the combination of field and circuit theory [102].

By combining field and circuit theory in innovative ways, it has become possible to incorporate the complex behaviour of non-linear or active components into the simulation without having to redefine the behaviour of the network as a whole. One method is to incorporate these components as lumped elements within the circuit, thus allowing the majority of the problem to be simulated in the normal fashion. An interface between the lumped elements and the solver needs to be established for the components to be fully incorporated, though this has been achieved successfully in both FDTD, using a SPICE model (a text description of a circuit component used by a simulator to mathematically predict the behaviour of that part) [103, 104], and in TLM [101, 105]. The inclusion of these lumped elements has now become a key part in modern simulation techniques with more complex components than ever now able to be modelled.

Another approach is to parametrise the highly complex non-linear behaviour into less complex parts and simulate each. This approach is akin to the approach followed in this research and has recently seen much

success in modelling an Esaki tunnel diode in a circuit simulator [106].

6.5 Behavioural Modelling and Modern Day Simulations

Today, the accurate simulation and analysis of microwave circuits and components is highly important in the industrial development of GHz systems, particularly given the reduction in feature size in modern digital systems [107, 108] and the progression into higher frequencies of the telecommunications domain with 5G and the coming 6G networks [109]. As components get smaller and more intricate, and their behaviour increasingly complex, the use of accurate simulation is the most efficient and cost effective method to explore and expand the manufacturing process of microwave components, both at the circuit and system levels [110], giving a deeper understanding and better informing design. Following the adoption and expansion of the method by many, the Transmission Line Modelling Method (TLM) by the early 2000s had been comprehensively defined and risen to be one of the most frequently used solver methods in modern electronics. It explores the similarities between the propagation of an EM wave through a system and the progression of voltages and currents through a circuit [84], and is a straightforward approach for simulating problems of electromagnetic compatibility and can be extended to describe non-linear lumped components such as diodes and transistors [111].

Modern modelling provides accurate simulation and analysis of many RF and microwave circuits and components. This is achieved using a variety of tools, though the most common are full-wave solvers and behavioural circuit simulators. Predicting the practical behaviour of systems based on

just schematic circuit diagrams - which indicate topology- fails to include the consequences of field effects (which require geometrical information). Given the ever increasing frequencies of modern digital systems, these field effects are of paramount importance [112]. While behavioural circuit simulators are simpler, field phenomena such as multiple random noise sources, and complex coupling are difficult to include [113]. Full-wave methods, one of the most common of which is TLM, are able to incorporate these effects, but are (often prohibitively) computationally expensive and time consuming to operate [112, 113]. Moreover, some of the issues that arise when simulating digital circuits, such as crosstalk, and external EMI are caused by field phenomena, and are difficult to include in behavioural circuit simulators [108]. The use of TLM results in algorithms which are easy to understand and can be efficiently implemented [100]. The modelling of electromagnetic fields using TLM with the inclusion of passive fine electrical features has been achieved with great success [111, 114], though the inclusion of active components, such as diodes, has not been so forthcoming [1].

Behavioural models are widely used in circuit solvers, due to their simplicity and accuracy, yet their use in full wave solvers has received little attention [113]. Given their success in improving the capabilities of circuit solvers, it is plausible that the incorporation behavioural models into full wave solvers could have a significant impact in improving the accuracy of the simulations whilst simultaneously reducing the complexity of the models and the computational requirements.

6.6 Motivation

The non-linear behaviour demonstrated by the post-diode configuration within a receiver protector (RxP) is difficult to model using TLM. Given the nature of a PiN diode as an active component, the parametrisation approach of running two simulations, one where the RxP is in the off-state, and therefore the PiN diode is forward biased, and the second with the PiN reverse biased in the on-state. This approach, though useful, fails to accurately model the full behaviour of the diode, particularly in the "switch over" region, where the diode switches from forward to reverse biased, though this region is largely negligible in practical applications and can be accounted for. Furthermore, to make the model as accurate as possible, it is important to define each of the layers of the PiN diode individually, thus allowing their electronic and material properties to be individually assigned. This raises the requirement of a hyperfine mesh in this region as some layers of the PiN diode are of the order of microns, resulting in a much greater computational resource requirement.

By replacing the diode region with a behavioural model "block" - a uniform body whose response is defined by a behavioural model to carefully mimic the complex behaviour of the component it replaces - it is possible to increase the mesh size (and therefore time step) of the simulation, allow a more accurate exemplification of the behaviour throughout the spectrum of the impulse and it should also remove the requirement for a second simulation to be conducted as the full behaviour may be modelled in one pass. Moreover, the potential for more complex component behaviours will become available for simulation as the behavioural model integration removes the need for approximation to simpler behaviours, which is often difficult and time consuming.

However, one of the major disadvantaged of replacing the complex

components with a "block" with predefined behaviour is that the intricacies and detail are lost. It is no longer possible to understand how the finer features of the diode itself (such as the layer thickness, doping levels, connecting ribbon path and so on) can impact the response of the diode. Each manufactured diode is unique and although the method of including a "block" of predetermined behaviour may be beneficial, it generalises the behaviour of the diode and does not allow for a complete understanding of the RxP system. With the capabilities of non-destructive inspection, the modern manufacturer can, if they so wish, simulate their exact system if the diode is not treated as a behavioural "block".

6.7 Model Integration

The modelling of complex components within an RF system is more commonly making use of behavioural models to describe their behaviour. These models replace fine and/or complex components or regions with larger lumped components, comprising of a block whose behaviour is determined by a preprogrammed equivalent circuit. It is the lumped component equivalent circuit that then interacts with the transmission line of the system (in TLM). It receives the incident voltages and currents, interacting with them as the device would, then passes output voltages and currents along the rest of the transmission line. Although other techniques have successfully interfaced complex lumped elements with solver previously (see [102]), modern simulations frequently use one of two models to do this, the SPICE model [115] or the Input/Output Buffer Information Specification (IBIS) model [113].

These two techniques can be integrated into the more common modelling methods, and have a large range of components that have had their

behavioural models defined for ease of access. However, consideration needs to be given to the predetermined nature of these models and the inability for detailed investigation or understanding, though the standardisation of components, particularly electronic components such as capacitors and diodes, often resigns this concern to the field of research rather than industry.

6.8 SPICE Model

The SPICE model has been interfaced with both FDTD (see [104, 107]) and TLM (see [115]). Building upon the equivalent circuit model, the SPICE model provides a circuit element that needs to be incorporated into the solver being used.

This circuit gives the current through the circuit element as a function of the voltage across the device. For some simple cases, the SPICE model can be implemented analytically [104]. A SPICE model is a text-description of a circuit component used by the SPICE Simulator to mathematically predict the behaviour of that part under varying operating conditions. SPICE models range from the simplest one line descriptions of a passive component, such as a resistor, to extremely complex sub-circuits that can be hundreds of lines long [103]. This text description can be limited by the availability of the devices in the SPICE library. Furthermore, SPICE needs to be invoked at every time step in a TLM simulation, limiting the computational efficiency of the simulation [108, 113].

The implementation of SPICE into TLM has been achieved, expanding the repertoire of TLM [115] and providing the advantage of a coarser spatial mesh throughout the simulation since the complexity of the circuit is modelled through the SPICE-TLM interface [108].

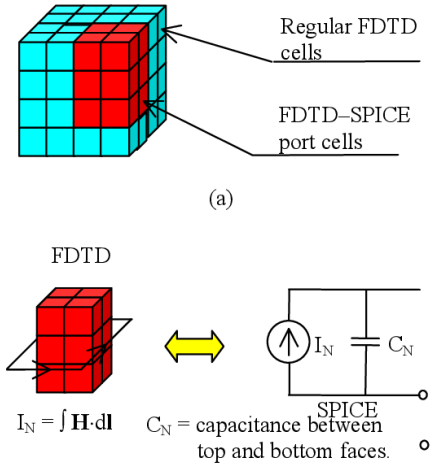

(a) The integration of SPICE model cells into an FDTD simulation [107]

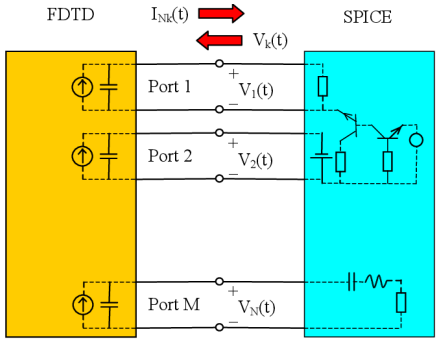

(b) The interface between a SPICE model and FDTD, showing how each FDTD port is connected to the SPICE model via an equivalent circuit [107]

Figure 6.3: The integration of the SPICE model with FDTD simulation (a) and the interface between the SPICE model and FDTD (b) are some of the key features of modern SPICE modelling techniques.

The SPICE model has been incorporated into FDTD and TLM using similar principles. In FDTD, the problem is split into two parts; (I) the distributed part analysed by FDTD and (II) the circuit part of the structure that is to be solved by SPICE. These two parts are then connected through a number of FDTD-SPICE ports, and are evaluated at each time step with the FDTD analysis passing to the SPICE model the input current for the port, before SPICE solves the magnetic field curl equation 6.1, passing the resultant voltage back into FDTD to update the electric field at the port nodes [107].

$$\nabla \times \mathbf{H} = \epsilon \frac{\partial \mathbf{E}}{\partial t} + \mathbf{J}(\mathbf{E}) \tag{6.1}$$

In TLM, the SPICE model can be implemented at either the nodes or the cell boundaries. Similarly to the FDTD implementation, the SPICE circuit is connected at a number of ports (TLM-SPICE interface ports) where the TLM mesh feeds the SPICE circuit with an input voltage. The SPICE circuit makes use of this input voltage to calculate the output volt-

age which is then fed back into the TLM circuit for further propagation. The SPICE circuit may consist of lumped and distributed elements, though to interface with the TLM mesh, a Thévenin voltage source or a Norton current source (depending on whether the SPICE circuit is current or voltage driven) must be found to represent the TLM structure [115].

Although the SPICE model has many benefits and can be seamlessly integrated into both TLM and FDTD, the requirement to invoke the model at each iteration is detrimental to the accessibility of this method. The increase in runtime experienced as a result of this requirement could result in simulation durations in excess of reasonable time, rendering the tool impractical for use. Additionally, the inability to investigate the finer details of the components poses an obstacle to understanding and can inhibit further innovation.

6.9 IBIS Model

The Input/Output Buffer Information Specification (IBIS) model is one of the most commonly used techniques for simulation complex components today. Developed by Intel in the 1990's, an IBIS model is a behavioural description of a device consisting of a catalog of look up tables with typical minimum and maximum current values for an operating range of voltages, that define how the device behaves electrically. The IBIS model is commonly interfaced with TLM with great success, and a significant amount of work in this area has been performed by Ian Scott et al. (see [112, 1, 113, 108]), enabling the insertion of active components as substructures within the TLM mesh [112].

The methodology behind the IBIS tables and their usage is read-

ily available [116], and improvements are being made and researched as the model continues to grow in popularity [117]. An IBIS model can be generated from a circuit simulation or by experimental measurements and can also include package resistance, inductance, capacitance and integrated circuit (IC) die capacitance at each port [118, 113].

The IBIS representation of a device removes the need to define the internal device structure (since only the behaviour of the device is required to be defined in the lumped element), resulting in the IBIS modelling technique has been widely adopted by industry to allow successful modelling by end users without the need to reveal proprietary information [1, 108]. A further advantage of IBIS is that computational efficiency is increased, since the method involves a simple look-up procedure rather than any complex calculations at each step.

6.9.1 IBIS Implementation

Integrating IBIS into TLM is frequently a three step process, though in some situations, embedding the IBIS model directly into TLM may be preferable (see [108]).

I. After the IBIS model has been selected, it is used as a non-linear termination to the TLM node.

II. Next, a short 1D circuit TLM model is placed between the IBIS termination to the 3D TLM field solver, with the 1D circuit including the package parasitics and die capacitance.

III. Finally, this 1D circuit is interfaced with the 3D TLM field solver.

The interface between the 1D circuit in section (II) and the 3D TLM solver

in section (III) is a standard TLM formulation (described in detail in [84]) and is defined at the boundary of the TLM node. This approach is more general, allowing the insertion of the behavioural model into the full field simulation and remains independent of the type of TLM node interfaced with [108]. At the TLM-IBIS interface, a Thévenin equivalent circuit is used to pass the source voltage from TLM to IBIS and back, with the standard Newton-Raphson method used with the IBIS model lookup tables to find the define the current given the voltage. This information is then fed back through the Thévenin equivalent circuit into TLM for further propagation. The IC (integrated component) itself is treated like a "black box", with only the equivalent circuit of the IC port represented by the IBIS lookup tables, effectively anonymising the device, which is preferable to manufacturers.

The IBIS model uses a V-I curve in the form of a table of current measurements taken as a series of output voltages within the range of $-V_{cc}$ to $+2V_{cc}$, where V_{cc} is the clamp curve voltage. This range is the operating voltage range that is used through any steps of the IBIS model. The data for the V-I curves are measured by placing a stepped / swept voltage source on the output and measuring the current into or out of the pin. The device is allowed to settle into semi-quiescent conditions. Allowing a buffer to reach quiescent conditions is easier to measure, but can be misleading in modelling dynamic switching behaviour. Adding pin parasitic information better models the high speed / high current switching behaviour.

The device anonymity of the IBIS model is highly appealing to many industrial parties as it can be used to protect intellectual property whilst still allowing the publication of research. Unfortunately, this can also have a negative impact on innovation in the field as results can often be irreplicable by other parties without the details of the devices. Similarly, the IBIS model standardizes the response of each component to a given range,

making exploratory research difficult.

Finally, although the computational resource requirements have been greatly reduced compared to the SPICE model, the inclusion of the 1D circuits to transition between 3D TLM and IBIS has the capability of introducing error into the simulation, particularly in the form of numerical rounding error and loss.

6.10 IBIS - SPICE Compatibility

Between the two modelling techniques, a plethora of devices and systems are able to be modelled. However, given that each model uses (and is applied using) different approaches, at first it seems that the two libraries would not be compatible. However, it has been suggested that an IBIS model could indeed be generated from SPICE, opening up a whole new catalogue of possibilities [119].

It can be conceived from the nature of an IBIS model, using voltage and current lookup tables to determine the output parameters of a device given the incident voltage / current, that the data from a SPICE model could be used to provide the data for the lookup tables of the IBIS model. By first simulating the device to get the V/I and V/T data for each of the input/output buffers, then feeding this data into an IBIS converter, it is possible to use the simulated data from the SPICE model to power the IBIS model[119].

6.11 Diode Models in Simulations

Whilst these has been some success in modelling PiN diodes in a different simulation software, little has been done in the application of PiN diodes in an RxP system. The design of the diode itself has been the focus of some research, with the intention of optimising and improving this ubiquitous component. The electro-thermal behaviour of the diode is important in all applications. Modelling the self heating behaviour of the PiN diode using DESSIS-ISE, Mimouni et al identified that the self heating of the device depends on the geometry and material parameters of the diode [120]. They also note that the use of TLM for such simulations is preferable since it is unconditionally stable. Minoumi et al built on the earlier understanding of the electrothermal properties of a PiN diode by Caverly et al [121]. Caverly and Khan used a SPICE model to determine how the resistance and insertion loss of a PiN diode varied with temperature. Combining these two works permits designers key insights to the electrothermal properties of PiN diodes, informing future advancements and design.

The use of PiN diodes as RF switches has been widely studied with their uses ranging from medical MRI [122] to high power limiters and broadband switches [123, 124]. Even though a SPICE model for a PiN diode exists [125], it is not uncommon for new research to innovate new representations of the diode. Simple, resistance only models cannot adequately model some of the more intricate effects observed in a PiN diode, such as I-region charge storage [125], thus more detailed and effective models are required to appropriately reproduce the behaviour of the PiN diode.

Despite significant research being completed into modelling PiN diodes, PiN diode model development and model implementation in a large number of applications, little has been applied to the application of a PiN diode within an RF waveguide or receiver protector system. Two potential

causes for the lack of publications could be the nature of the application and the state of innovation in the industry. Industrial producers of RxP systems are sensitive about the intellectual property of their research, given it directly impacts the performance of their devices and company, and therefore may be less willing to publish their findings. Similarly, as one of the primary uses for an RxP system is in the defence sector, publishing research into the modelling and operation of these sensitive devices could be detrimental.

The use of behavioural models to describe complex, active or non-linear components within an EM field simulation is an invaluable tool. Being able to simplify the region to a uniform block whose behaviour is defined by either an equivalent circuit or some lookup tables vastly improves the accuracy and capabilities of the simulation, whilst simultaneously reducing the computational resources required. Equally, the ability to study in detail the composition of the PiN diode can be beneficial to future design and production of RxP systems, improving their efficiency and efficacy.

Although a SPICE model of a PiN diode is currently available, this research will instead focus on the development of an alternative model. The deeper insight and understanding of the RxP system and the role of the PiN diode within this system that is the goal of this research, will not be achievable through the integration of the SPICE model. The challenges of integration and modification of the SPICE model for the purposes of this research outweigh the benefits that would be gained.

Furthermore, with the recent development of UTLM (the interested reader is referred to chapter 3.3 and the references therein) the reliance of TLM on equivalent circuit models and representations to imitate small or complex components is reduced. With the unstructured mesh approach offered by UTLM, small details and curved surfaces can be modelled in a way that minimises the numerical and dispersion errors that are typically

present in conventional TLM.

Therefore, the decision was taken to use UTLM to construct the diode model in this research. The enhanced ability of UTLM to appropriately define small and curved elements of the geometry offers an opportunity for a detailed study of the diode and its behaviour. The next chapter presents a step-by-step approach to the building of the diode model. This method increases the understanding of the elements found within the diode and highlights the origin of some of the features within the data. This chapter has 2 key features, first, it uses a parametrised solution to modelling the non-linear behaviour of the diode. At RF frequencies, the "switch-over" time for a PiN diode (where it transitions from forward to reverse biased - off-state to on-state) is miniscule, and therefore can be disregarded in the model development presented in this work. The focus of the simulations can then become the behaviour of the diode in the two distinct states, where it spends the majority of its life. Secondly, by building the diode from a simple model to one where each of the constituent layers of the diode are realised, a comprehensive understanding of which elements contribute most to the behaviour of the diode can be developed.

These two features will allow a significant level of detail and comprehension to be achieved. However, for this to be a successful endeavour, the model developed in this research should at least match if not exceed the performance of the other techniques presented here. Through discussions with industry, a set of threshold parameters have been identified that will be explained in more detail in the coming pages of this thesis. Future research could look at including either a SPICE or an IBIS representation of a diode into UTLM for comparison and accessibility.

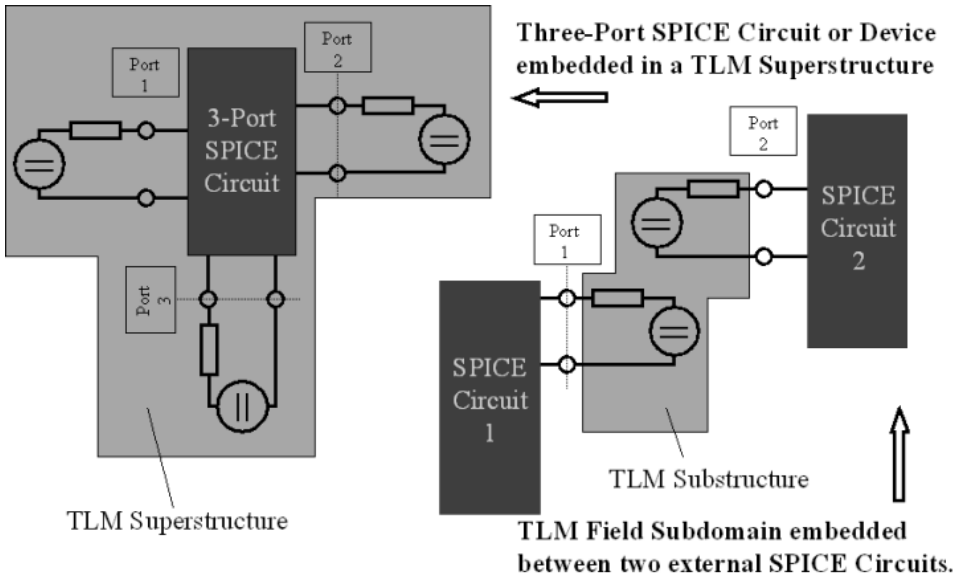

(a) The 2 different forms of integration of a SPICE model into a TLM simulation [115]

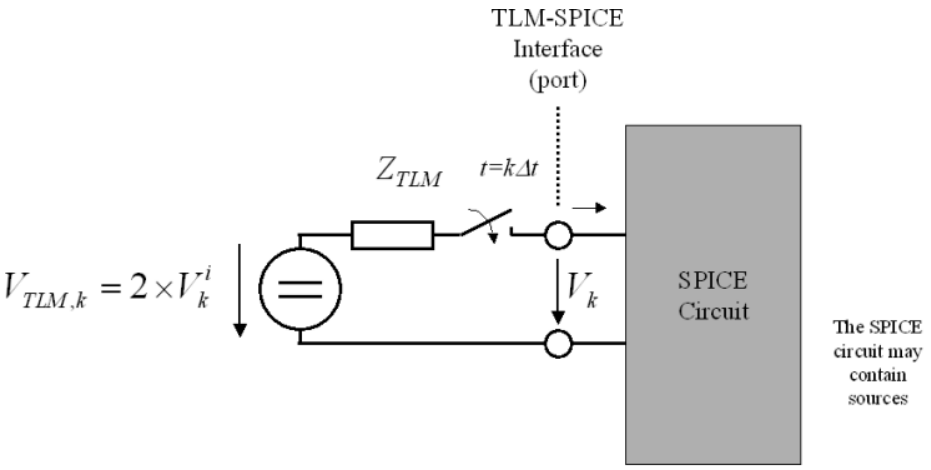

(b) The interface between a SPICE model and a TLM node, showing the equivalent circuit required at the TLM-SPICE interface [115]

Figure 6.4: SPICE models can also be integrated into TLM (a), using an equivalent circuit at the interface (b).

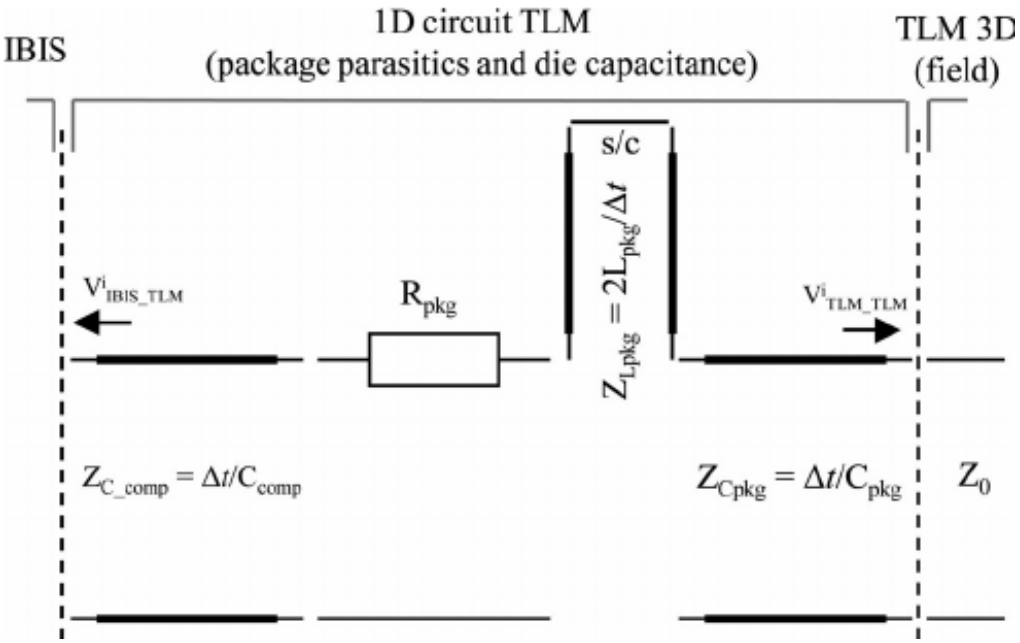

Figure 6.5: Diagram showing the 1-D TLM circuit modeling the IBIS package parasitics between the non-linear IBIS source/load on the left and the 3-D field TLM on the right. [1]

Chapter 7

A Systematic Approach to Modelling a PiN Diode

The previous results (chapter 4) presented a comprehensive investigation into some of the classically behaved components that comprise a receiver protection system (RxP), however it did not address the complex behaviour observed in practical systems. The response of the PiN diode can broadly be simplified into two states of operation, the off-state where the diode is forward biased and allows wave propagation, i.e. the RxP is inactive, and the on-state, where the forward biased nature of the diode inhibits the flow of the signal, protecting the receiver. Modelling PiN diodes is challenging due to the layers of semiconductor present being of the order of microns, and consequently, this component is often replaced by a simple homogenous block with a predefined response or programmed with an equivalent circuit (see chapter 6).

This chapter presents a methodical approach to creating a reliable and detailed model of the diode. The first part of this chapter will outline the motivation for conducting this study, followed by an introduction to the

method used to develop the diode model. The results of the simulations are then presented, along with a discussion of how each model compares with the last stage, before the key takeaways from this investigation are highlighted. This investigation will develop the model of the diode from a simple homogeneous block into a 3-layer representation through 5 stages, with each increasing in complexity and accuracy on the last.

The final part of this chapter will explore the scattering effects identified within the RxP system. The presence of the RxP system, in particular the inductive post, can cause the incident signal to be scattered into other modes, with higher cut-off frequencies. Which modes are excited depends on what characteristics the scattered modes share with the incident signal.

7.1 Introduction and Motivation

The PiN diode is the most complex component within the RxP system to model. In addition to the bi-state behaviour the physical size of the diode also presents a challenge, both in terms of model integration and simulation optimisation. The difference in scale between the layers of the PiN diode and the larger components, such as the waveguide, introduces the problem of a non-uniform mesh size throughout the system. Although a uniform mesh could conceivably be used for the whole geometry, the factor of 10^4 between largest and smallest features in the geometry would result in inflated resource requirements and duration.

Developing the model in stages has the additional advantage, much like in the piecewise analysis, of giving an insight into how each aspect of the geometry can influence the behaviour of the the s-parameters. This could potentially enable easier and more streamlined fault finding in future. Having a detailed model can provide a more cost effective resource for

tuning the system and facilitate more efficient research and development of similar systems in the future.

With this in mind, the primary objectives for this investigation were:

I. **To build a physically accurate diode model** - Both in terms of geometry and features, and ensuring that the device responds in the same way as a physical diode would.

II. **To minimise resource and runtime requirements** - Making the model more accessible by reducing the requirement for expensive, high performance infrastructure. Efficient simulations can also be used to drive advancements in the RxP system through cost effective research and development.

7.2 Investigation Outline

Following a similar iterative process to the one outlined in chapter 4, the PiN diode will be transformed from a simple, homogeneous block of material to a fully detailed, 3-layer representation, which will be adaptable for future research avenues, including exploring different semiconductor heterostructures.

Starting with a simple metallic "switching block", a block of homogeneous material with identical dimensions to the diode, the model is developed over 5 stages, culminating in a detailed representation of the full RxP system found in use today. The final formulation of the RxP features two diodes housed in a diode package and connected to the inductive post through a pair of bonding ribbons. These diodes will be fully represented as surface layer geometries, meaning that although not physically present in the rendering, they are included in the simulation stage of the system.

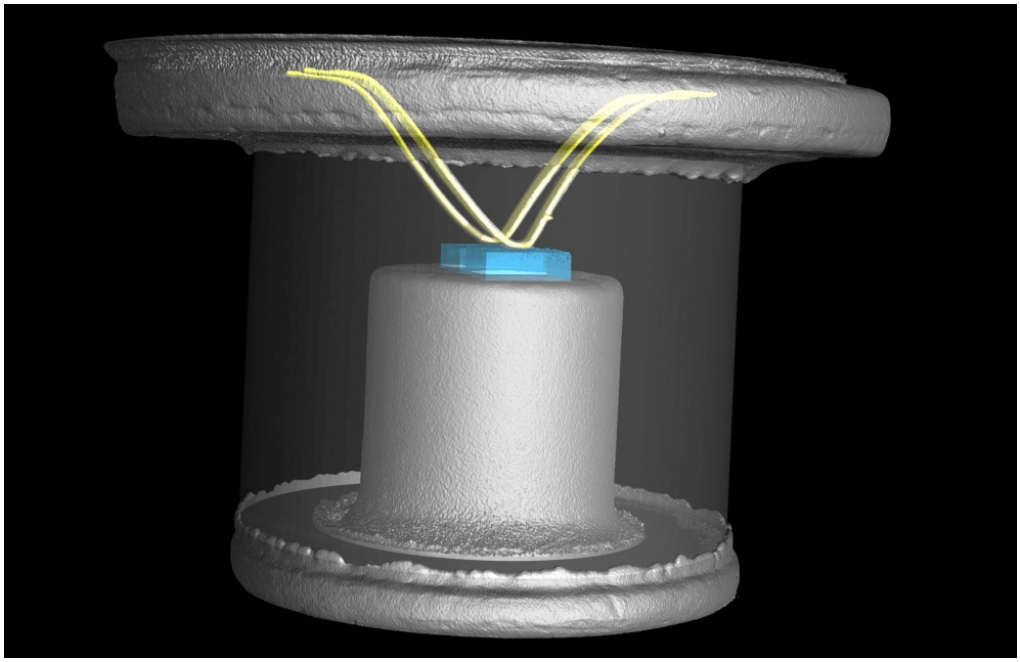

Figure 7.1: A rendering of the inside of the PiN diode package developed from a micro-CT scan taken at the University of Nottingham. The rendering highlights the presence of 2 diodes within the package, connected via 2 metallic ribbons to the plate at the top of the package, where it would join into the rest of the RxP structure.

This has the significant advantage of being able to simulate the diode in microscopic layer detail without the need for a hyperfine mesh across the simulation. Furthermore, modelling the diode in surface layer configuration opens the door to exploring alternative diode constructions, from doping levels and dopants to different semiconductor materials.

A comprehensive understanding of the inner workings of the diode package was achieved by performing x-ray tomography on a diode package kindly provided by an industrial advisor (see figure 7.1). This process allowed the construction of the PiN diode to be studied without destroying the device. The final model was developed to have the same features as the physical diode in the x-ray, though the paths of the connecting ribbons are arbitrary, so a simpler, more uniform path was chosen. By combining the x-ray of the diode with the schematic details, each stage of the diode model development was designed to incorporate a new, significant feature into the geometry or to modify the current representation to better reflect

reality or improve performance.

The performance of the model at each stage will be derived from the input and output voltages and currents of the simulations in the form of the s-parameters, and power conservation. In addition, the s-parameters will be qualitatively compared to a set of results published in the literature (see [6]) as a benchmark of behaviour in similar devices. The sensitivity of the system to minor dimensional changes (as explored in chapter 4) means that these results will not be directly comparable to those in this research, however it was still possible to compare the nature of the curves generated by the two systems.

The results of each model presented in this chapter all follow the same structure. Initially, the geometry of the model is presented, along with a description of the differences compared to the previous iteration. The performance of the simulation is compared to the previous model by means of the key simulation parameters, defined in table 7.1, giving an insight into the requirements and run time for this model. Table 7.1, also mentions the target behaviour, intentions and thresholds for these parameters.

The performance of each model will be analysed using the s-parameters and power analysis. The s-parameters will be used to search for regions of transmission and reflection. The off-state should allow the signal to propagate uninhibited in-band, with reflection being the in-band behaviour when the diode is in the off-state. Additionally, the power conservation of each model will be checked using the s-parameter relations expressed in 2.65. Since the system is only excited through port one, power can be deemed conserved if equation 2.65a is satisfied. Sources of power loss are most likely absorption from the components. Occasionally, oscillations are observed around a value, which are often caused by numerical error. The final panel in the plots will always remain the curves found in literature [6].

Key Parameter Definitions		
Parameter	**Definition**	**Target**
Mesh Size & Refinements	The grid separation of the mesh of the geometry **&** Details of any smaller regions of mesh to improve accuracy	Maximise using refinements where necessary in the smallest regions
SCN Equivalent Edge Length	The minimum length of the edge of a symmetrically condensed node	Maximise
Timestep Size & Number of Timesteps	The time taken for the signal to pass a distance of 1 SCN equivalent edge length **&** The total number of timesteps in the simulation	Minimise
Simulation Run Time	How long (in hours/minutes/seconds) the simulation took to complete	Minimise - Keep below 24 hours

Table 7.1: This table summarises the definitions for each of the key simulation parameters compared within this investigation. It also provides an indication into the target (threshold) behaviour of the parameter (whether it is should be maximised or minimised and any threshold values) which are chosen to improve the utility of this model.

7.2.1 Model development pathway

The diode modelled in this research is a silicon PiN diode with 3 distinct p-, i-, and n-layers. The p- and n- layers each measure $1\mu m$ in thickness with the intrinsic layer having a thickness of $12\mu m$. In order to effectively model this device, a 5 stage model development pathway was identified, as shown in figure 7.2. Some of the key terms used in this research:

- **Switching block** - homogeneous block of material, modelled as a perfect metal in the on-state and a dielectric with the relative permittivity ϵ_r (silicon) in the off-state.
- **Surface layers** - introduced in the simulation file, behave as if layers were physically present but are not meshed in the final geometry, increasing the size of the smallest component in the geometry.

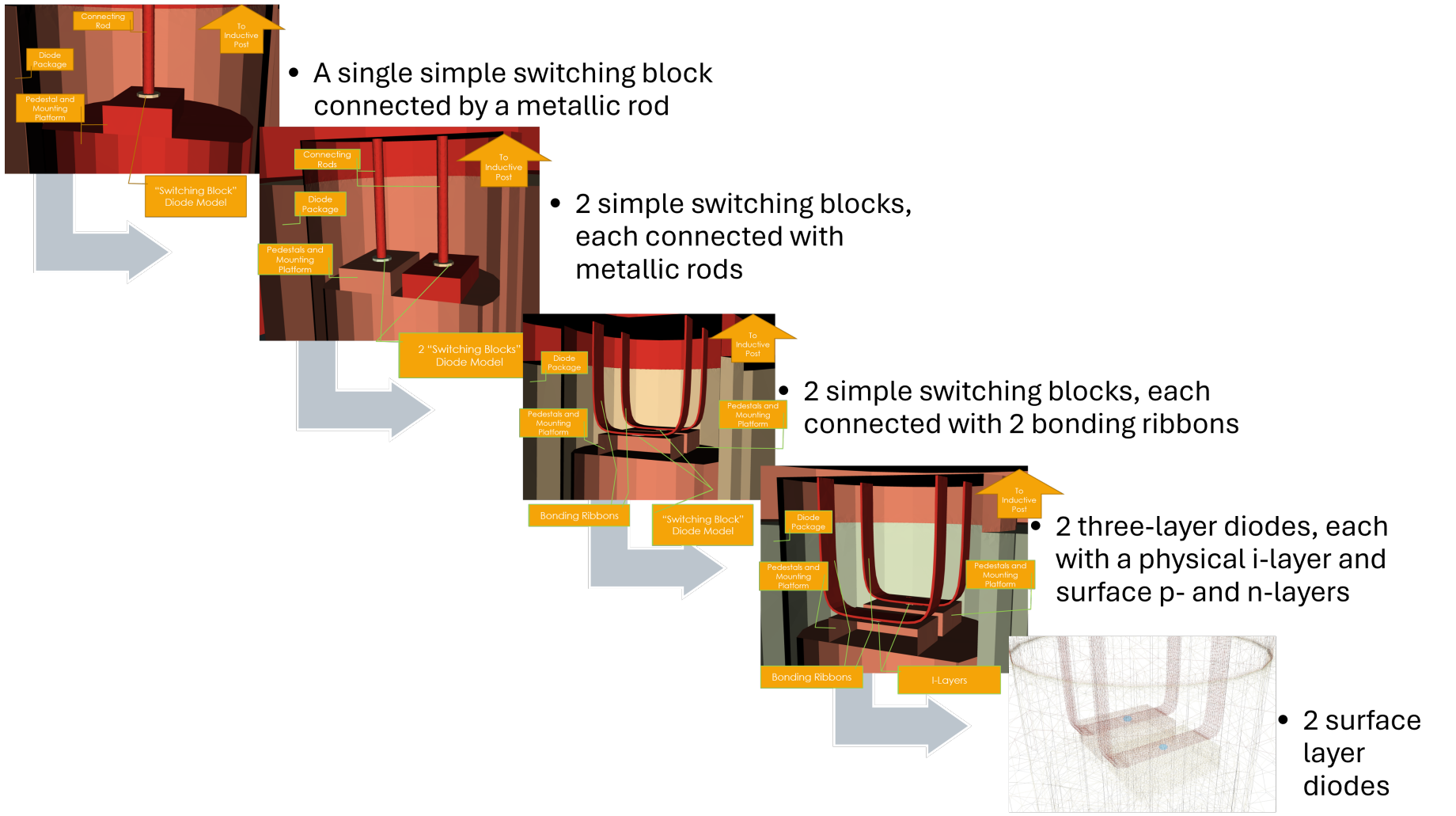

Figure 7.2: A simple diagram presenting the pathway of the PiN diode model development - starting with a singular simple switching block connected to the main post structure via a solid metallic rod and finishing with a fully described 3 layer model of multiple PiN diodes, as would be seen in RxP systems in practice.

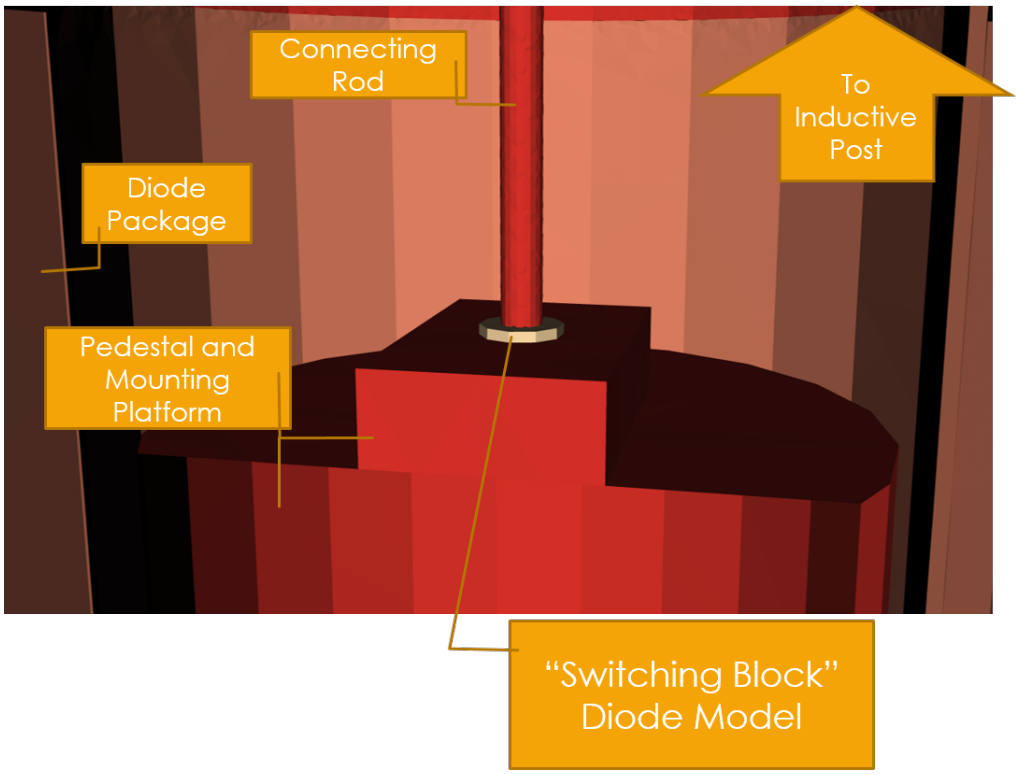

Figure 7.3: The first stage of the investigation into the diode model. This image shows a detailed view of the inside of the diode package where a small "switching block" of material can be seen attached to the inductive post by a thin connecting rod. The switching block is designed to have the same dimensions as the diode and perform in a similar way, namely dielectric in the off-state and conducting in the on-state. Future models will build on this simple representation of a diode.

7.3 Model 1 - The Simple Switching Block

This first diode model, shown in figure 7.3, introduces 2 new components into the system and modifies one other. The first inclusion is the diode package, a hollow cylinder of dielectric surrounding the region where the diode and connectors are found. The relative permittivity of this package cylinder is selected to be $\epsilon_r = 9.2$, designed to imitate a form of ceramic known as alumina.

In addition, a small mounting platform is included to connect the diode to the bottom of the waveguide cavity. It narrows and extends inside the diode package. On top of the mounting platform, a small, homoge-

neous block of material. This is the "switching block" used to imitate the "diode". It is conducting (metallic) in the on-state and in the off-state is dielectric with a relative permittivity of $\epsilon_r = 11.7$, the same as a block of silicon. The dimensions of the switching block diode are identical to the diode, with a diameter of 125 μm and a depth of 12 μm .

In this model, the diode is centred on the top of the mounting platform. In the physical device (and in later stages of this research) there are two diodes present, each positioned off centre, as can be seen in figure 7.1. The switching block diode is connected to the full post structure above using a thinner portion of the inductive post, referred to as the connecting rod.

When simulating the system in the on-state, when the diode is forward biased and the system is in a short-circuit state to protect the receiver. In this state, the diode is treated as an extension of the inductive post, with all each of the elements merged into one large inductive post. This achieved the same accuracy as when each element was modelled individually, but minimised the number of interfaces and small artefacts within the geometry, improving the simulation speed.

The key simulation parameters for this model are documented in table 7.2. Given the simplicity of this model, it is to be expected that both the simulation run time and the required number of timesteps will be lower than for the more advanced models. Being the first model in an investigation, there is little to compare the results to, however in terms of the threshold targets laid out at the start of this chapter, the model fits well within those bounds. These results show that the computational performance of the model is good.

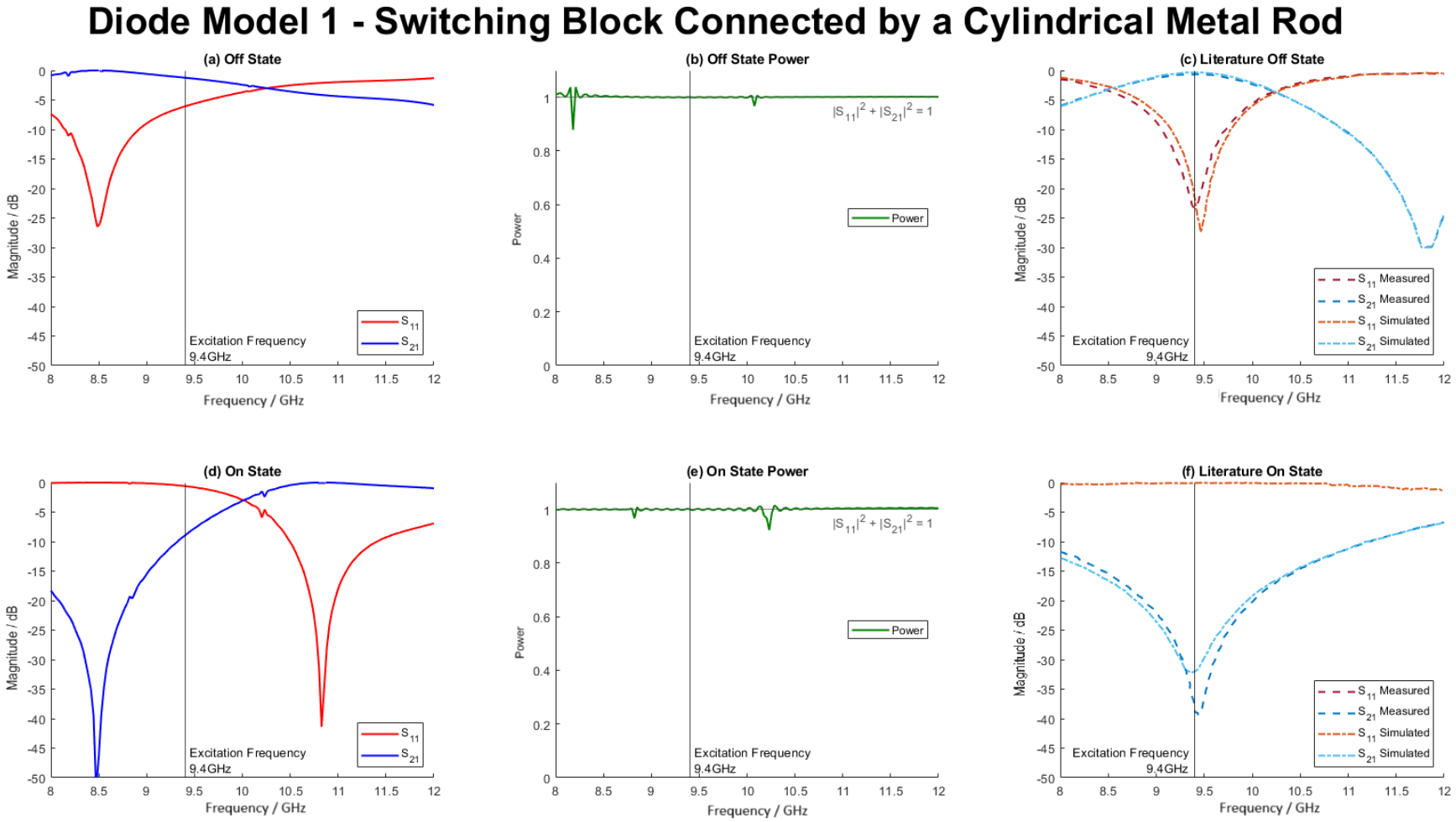

Figure 7.4: Simulation data from the first model in the diode model investigation. (a) The in-band s-parameter response with the diode in the off-state, (b) The total power of the system in-band in the off-state computed from equation 2.65a, (c) The in-band response from a full RxP system in the off-state (both simulation data and experimental measurement) found in [6], (d) the in-band s-parameter response with the diode in the on-state, (e) The total power of the system in-band in the on-state computed from equation 2.65a, (f) The in-band response from a full RxP system in the on-state (both simulation data and experimental measurement) found in [6]

Model 1 - Singular Switching Block Diode		
Parameter	**Off-state**	**On-State**
Mesh Size & Refinements	1 mm no refinements	1 mm no refinements
SCN Equivalent Edge Length	8.3 μm	8.45 μm
Timestep Size & Number of Timesteps	0.01 ps 2×10^6	0.014 ps 2×10^6
Simulation Run Time	1 hour 50 minutes	1 hour 48 minutes

Table 7.2: The key simulation parameters for the first simulation in the diode model investigation. The diode model tested consists of a single "switching block" connected by a metallic rod to the rest of the inductive post. As predicted, the runtime and required number of timesteps for this simple model remain low.

The in-band response of the single switching block diode model is shown in figure 7.4 following excitation at 9.4 GHz. The leftmost panels show the s-parameter response of the model for the main operational band in the off-state (a) and on-state (d) respectively. Comparing these two panels shows a clear switch in behaviour. In panel (a), a region of transmission can be observed between ≈8-10 GHz, where the transmission coefficient S_{21} is in a region of maximum (≈ 1) whereas the reflection coefficient, S_{11} is significantly below. Peak transmission occurs in the off-state at around 8.5 GHz, where it is possible to observe that both coefficients are opposed, with S_{21} at a maximum and S_{11} at a minimum.

In the on-state, a region of reflection observed between ≈8-10 GHz, with peak reflection at around 8.5GHz. This is the behaviour that would be expected of an RxP system. The desired response is that the regions of maximum reflection and transmission occur in-band, as close to the excitation frequency as possible. Although the peak performance here is not in-line with the excitation, the behaviour itself is correct. It would be expected that such a simplistic representation would not give perfect results, however the response is promising.

Panels (b) and (e) show that power is conserved within the system, indicating that the simulation is physically accurate. Minor oscillations are visible in the data, though these are likely due to numerical noise. The power conservation is considered to be within acceptable bounds.

Finally, the rightmost panels (c) and (f) show the in-band response found in literature [6].The data presented by Farrington et al. is for a more complex diode model than this simple switching block, however, the general shape of the response curves do match. The behaviour of the two systems is similar, though peak performance occurs at different frequencies, indicating that the simple switching block model is exhibiting the correct behaviour of an RxP system, though has been overly simplified. It also indicates that the design of the two models differs, with some aspects of this model differing in size from the published model.

7.4 Stage 2 - 2 Switching Blocks

The second model introduces the second diode, as seen in figure 7.5, in order to reflect practical RxP systems. This introduces 2 key differences to the previous model, the diodes are no longer central in the package, and the introduction of a second connecting rod in parallel to the first. Instead of being placed in the centre of the package, the diodes are spaced equally from the centre line in the z-orientation (i.e. along the direction of propagation of the wave).

As before, the post is extended in two thinner rods to connect to the diode, as shown in figure 7.5, and in the on-state, the diodes are treated as conducting and therefore merge with all of the above structure, including the thinner connecting rods.

Table 7.3 shows the key simulation parameters for this second model.

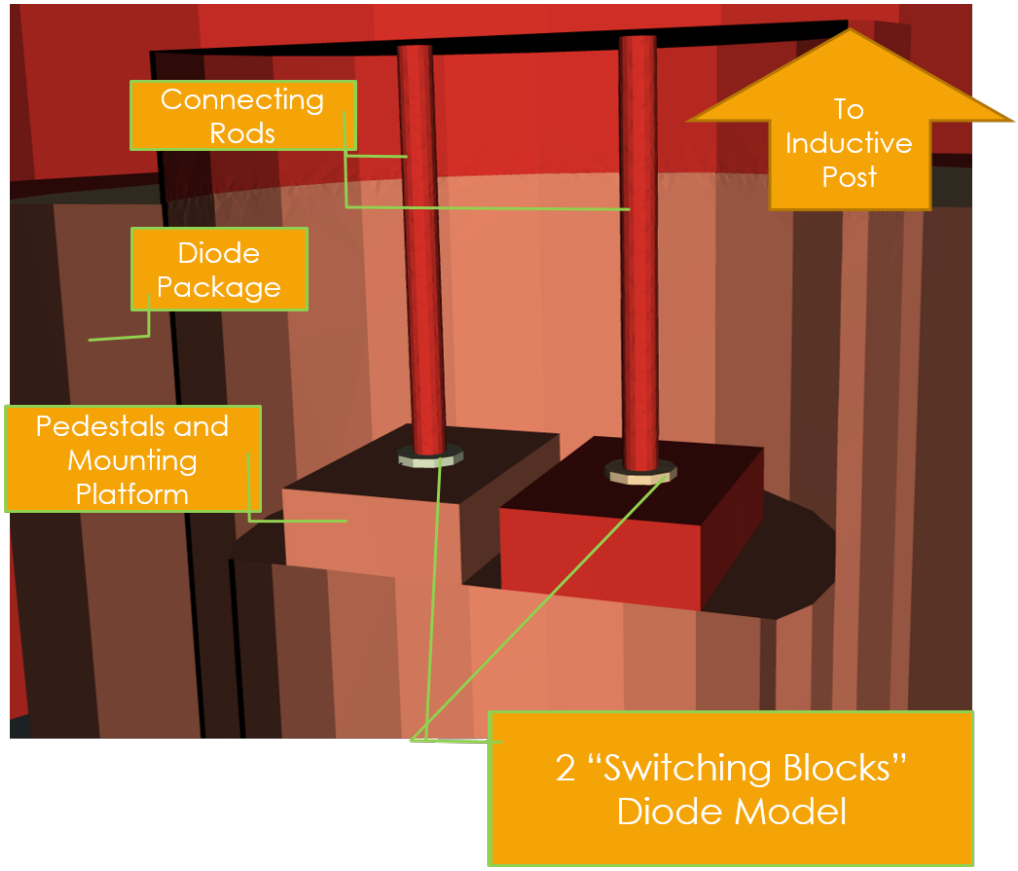

Figure 7.5: The second stage of the investigation into the diode model. This image shows a detailed view of the inside of the diode package where two thin "switching blocks" of material can be seen attached to the inductive post by connecting rods.

The most noticeable difference when comparing this data with the previous set is that the SCN equivalent edge length has reduced from $\approx 8.4\ \mu m$ to $3.7\ \mu m$. This reflects the increase in the complexity of the geometry introduced by the close proximity of the two diode structures. The driving factor behind the SCN equivalent edge length is the clustering of smaller tetrahedra into larger non-uniform shapes. If the geometry consists of large, uniform shapes and structures, the standard Cartesian mesh often suffices with little need for clustering. However, with multiple curved surfaces in close proximity, the requirement to cluster together smaller tetrahedra to appropriately define these surfaces increases, thus reducing the size of the symmetrically condensed nodes (SCNs) found in this region.

One consequence of this is the decrease in timestep size, from $\approx$

Model 2 - 2 Switching Block Diodes		
Parameter	**Off-state**	**On-State**
Mesh Size & Refinements	1 mm no refinements	1 mm no refinements
SCN Equivalent Edge Length	3.79 μm	4.14 μm
Timestep Size & Number of Timesteps	0.006 ps 2×10^6	0.006 ps 2×10^6
Simulation Run Time	1 hour 58 minutes	1 hour 54 minutes

Table 7.3: The key simulation parameters for the second simulation in the diode model investigation. This diode model is formed of two "switching blocks" connected by a metallic rods to the rest of the inductive post structure. They are equally spaced in the direction of wave propagation with their collective centre point positioned in the centre of the waveguide. As predicted, the runtime and required number of timesteps for this simple model remain low.

0.01 ps to just over half that value at 0.006 ps. The reduction in timestep duration was necessitated by the reduction in size of the SCN node edge length, otherwise the spatial resolution required to realise these aspects of the geometry would not be achieved.

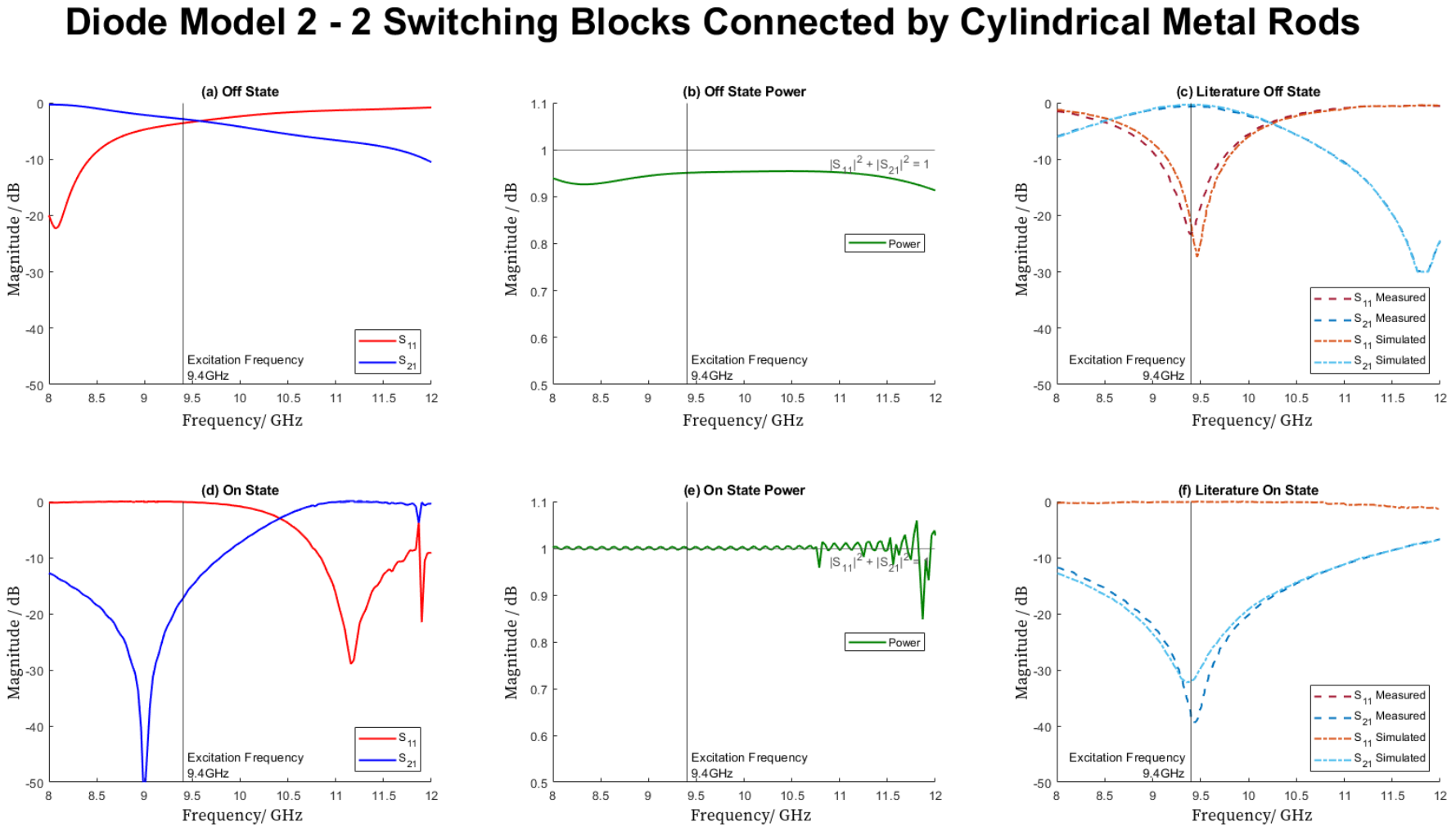

Figure 7.6: Simulation data from the second model in the diode model investigation. (a) The in-band s-parameter response with the diode in the off-state, (b) The total power of the system in-band in the off-state computed from equation 2.65a, (c) The in-band response from a full RxP system in the off-state (both simulation data and experimental measurement) found in [6], (d) the in-band s-parameter response with the diode in the on-state, (e) The total power of the system in-band in the on-state calculated from equation 2.65a, (f) The in-band response from a full RxP system in the on-state (both simulation data and experimental measurement) found in [6]

Comparing the s-parameter responses in the off-state (panel (a)) and on-state (panel (d)) with those found in the published literature - panels (c) and (e) respectively - the behaviour of this model is similar to the full RxP. Understandably, the performance of this simplified model is below that of the full RxP system found in literature, and with different dimensions for each of the components the responses will not match. However, clear regions of transmission and reflection are found in this model in the off- and on-states respectively.

It is worth noting that the region of peak transmission in the off-state is at a lower frequency than the region of reflection in the on-state. This discrepancy results from the geometry of the system, and with further tuning, the strongest transmission region can be brought to match the strongest reflection region. Considering that the true system involves more complex connecting ribbons, rather than rods, this was not of concern.

Furthermore, a small resonance between the two conducting rods can be observed in the on-state, peaking at around 11.8 GHz. This can clearly be identified by the oscillations in the power leading up to this spike and the spiking behaviour observed at this frequency in the s-parameters. Similarly to the switching response, this resonance is borne out of the simplistic nature of the geometry. Two conducting pillars in close proximity will interact, however once they are replaced in future models with the more intricate bonding ribbons, it is expected that this resonance will decrease.

The power of the system in the off-state, shown in panel 7.5(b), appears to show a small loss. This is most likely a combination of numerical errors in the simulation and absorption by the dielectric materials in the system. In the on-state, the implied gain towards higher frequencies is as a result of numerical noise, since the RxP is a passive system.

As before, comparison of the responses of this model (panels (a) and (d)) with those in the published literature (panels (c) and (f)) suggests the

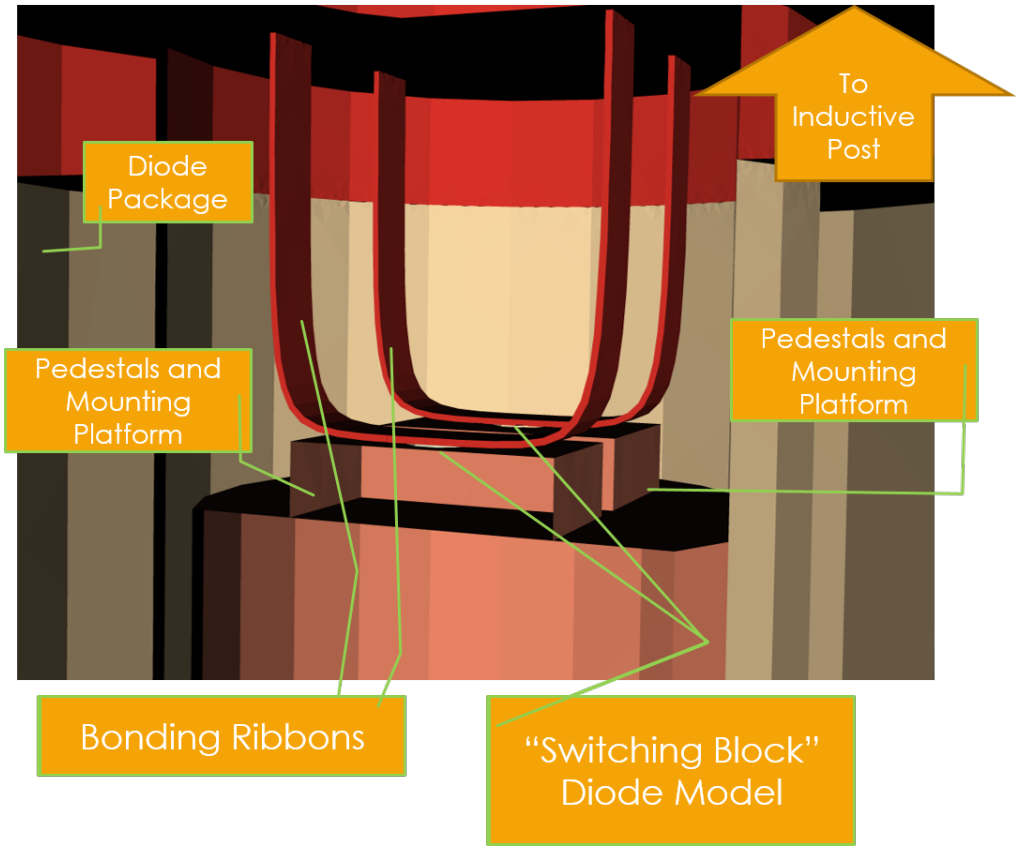

Figure 7.7: In this third stage of the model development, the two connecting rods have been replaced by bonding ribbons. These bonding ribbons are modelled to be made of a highly conductive metal with a conductivity, $\sigma_E = 1 \times 10^8$

general behaviour of the two systems are similar. The oversimplified model presented in this stage still requires further development to more closely match the fine tuned system published in the literature.

7.5 Stage 3 - Adding the Ribbons

The next stage is to replace the connecting rods found in the previous model with the more realistic connecting ribbons as seen in figure 7.7. Practically, using connecting ribbons instead of rods, reduces the amount of material required, increases the surface area (important for making a good contact) and the flexibility of the ribbons makes them more versatile in manufacture and tolerant of stresses.

Model 3 - Addition of Connecting Ribbons		
Parameter	**Off-state**	**On-State**
Mesh Size & Refinements	1 mm no refinements	1 mm no refinements
SCN Equivalent Edge Length	0.92 μm	6.13 μm
Timestep Size & Number of Timesteps	0.0015 ps 15×10^6	0.01 ps 10×10^6
Simulation Run Time	11 hours 58 minutes	5 hours 34 minutes

Table 7.4: The key simulation parameters for the third model explored in in the diode model investigation. This diode model is formed of two "switching blocks" connected by a smooth, curved bonding ribbons to the rest of the inductive post structure. The ribbons are formed of Bézier curves, are connected to the rest of the post structure and are modelled as gold. The curved nature of the ribbons, for reasons discussed previously, greatly increases the load of the simulation, but the improved accuracy of the model is a worthy result.

The arbitrary path of the ribbons in this model was a form of Bézier curve, with the general shape intended to mimic a "U" for each diode. Bézier curves use a discrete set of control points and a form linear interpolation to define a smooth, continuous curve between two end points. Figure 7.7 shows the final shape of the ribbons.

In the discussion on the shape of the inductive post addressed previously in this research 4, it was highlighted that curved surfaces have a significant impact on the simulation, both in terms of runtime and requirements. The introduction of the smooth curves of these connecting ribbons is reflected in the increased runtime shown in table 7.4. The total runtime still remains below the threshold value.

In this simulation, the significance of different material properties on the simulation parameters becomes visible. In the off-state, where the diode is a small region of dielectric, there are interfaces between different materials to be realised. The result of this is the reduction in SCN equivalent edge length when compared to the off-state and an increase in the

required number of timesteps, the runtime and reduction in timestep size.

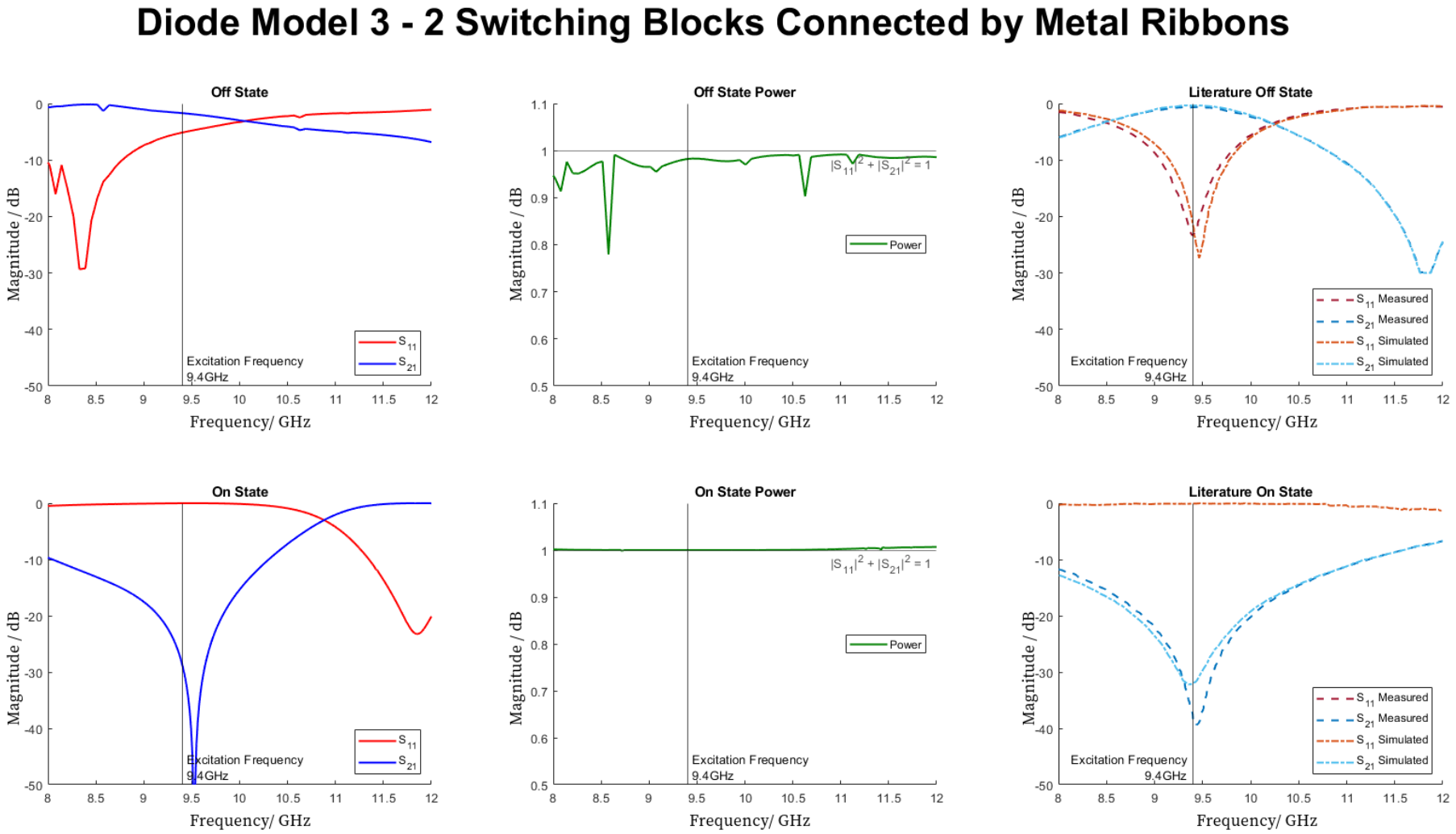

Figure 7.8: Simulation data from the third model in the diode model investigation. (a) The in-band s-parameter response with the diode in the off-state, (b) The total power of the system in-band in the off-state computed from equation 2.65a, (c) The in-band response from a full RxP system in the off-state (both simulation data and experimental measurement) found in [6], (d) the in-band s-parameter response with the diode in the on-state, (e) The total power of the system in-band in the on-state computed from equation2.65a, (f) The in-band response from a full RxP system in the on-state (both simulation data and experimental measurement) found in [6]

Panel (c) of figure 7.8 shows that the peak reflection response matches very well with the excitation frequency, and closely matches the published results, shown in figure 7.8(f). The off-state results found in panel (a) show an improvement, though still remain distinctly different from those published in the literature shown in panel (c). Furthermore, an examination of the power of the on-state simulations shown between these two panes, demonstrates that there is no power loss in the system either. Overall, the geometry of this on-state simulation, with a little tuning, is a very effective representation of the on-state behaviour of an RxP system.

In the off-state, the data shown in figure 7.8(a) demonstrates an improvement over previous models. The region of maximum transmission has processed towards the excitation frequency and now lies at approximately 8.4 GHz versus the 8.1 GHz of the previous two diode model. The comparison between the published results (7.8 (c)) and the data of this simulation suggests that the overall behaviour matches well, though further refinement is needed.

Panel (b) of figure 7.8 provides two insights into the behaviour of the off-state of this model. It can be seen that the power data is not the smooth curve found in the previous model (see panel (b) of 7.6). This suggests the presence of some interference or resonance is occurring between the two diode structures. Other than these interactions, the power of the system remains conserved, accounting for absorption and numerical errors.

7.6 Stage 4 - Introducing Surface Layers

This iteration of the diode model addresses the structure of a diode. As discussed in chapter 5, a PiN diode is not merely a homogeneous block of material, but consists of 3 distinct layers, each with their own electronic

and material properties. Reflecting this in the geometry and the diode model of this research allows a deeper understanding of the diode itself.

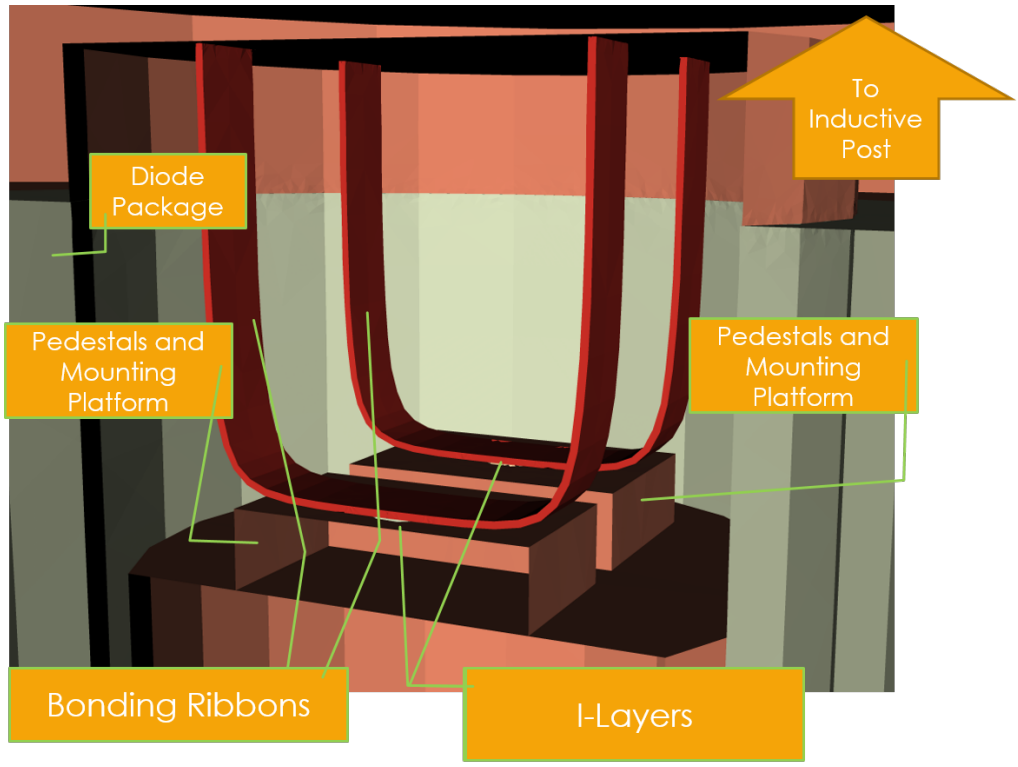

Figure 7.9: In this stage of the model, the introduction of the first two surface layers is seen. This representation of the diode involves a physical geometry element for the I-Layer, with the P- and N- layers included in the simulation through the use of surface treatment layers. This helps increase the size of the smallest physical element within the geometry to that of the I-Layer.

This model (shown in figure 7.9) removes the "switching bocks" of previous models and replaces them with a collaboration of physical and surface geometries. The I-layer situated between the bonding ribbons and the mount structure is a smaller, homogenous block. The dimensions of the block have been changed to mimic that of the I-layer size of the physical diode, taken from technical data found in [126, 127]. Similarly to previous models, the I-layer is defined to have the properties of silicon in the off-state, with a relative permittivity of $\epsilon_r = 11.7$ and in the on-state treated as conducting.

The surface p- and n-layers introduced here, unlike the I-layer, are not physically present when the geometry is meshed, but they are inserted

Model 4 - Surface p- and n-layers		
Parameter	**Off-state**	**On-State**
Mesh Size & Refinements	1 mm Bonding ribbons, I-layer and Mount refined to 0.5 μm	1 mm no refinements
SCN Equivalent Edge Length	0.21 μm	4.9 μm
Timestep Size & Number of Timesteps	0.0003 ps 50×10^6	0.008 ps 10×10^6
Simulation Run Time	160 hours 25 minutes	5 hours 34 minutes

Table 7.5: The key simulation parameters for the penultimate model explored in in the diode model investigation. This representation of the diode includes 3 distinct layers to comprise each of the two diodes. the I-layers are physically present in the meshed geometry, though the p- and n- layers are include as surface layers in the final simulation only, allowing for greater precision in their definition.

before the simulation is commenced. Introducing the layer definition of the diode allows significantly more control over the composition and properties of the diode, allowing each individual layer to be defined and explored independently. Furthermore, using surface layers for the smaller elements in the geometry prevents the need for regions of hyperfine mesh, which have a detrimental effect on simulation requirements. However, the presence of the physical I-layer in the geometry means that fine meshes are still required in some regions, though not as fine as if the p- and n- layers were physically present.

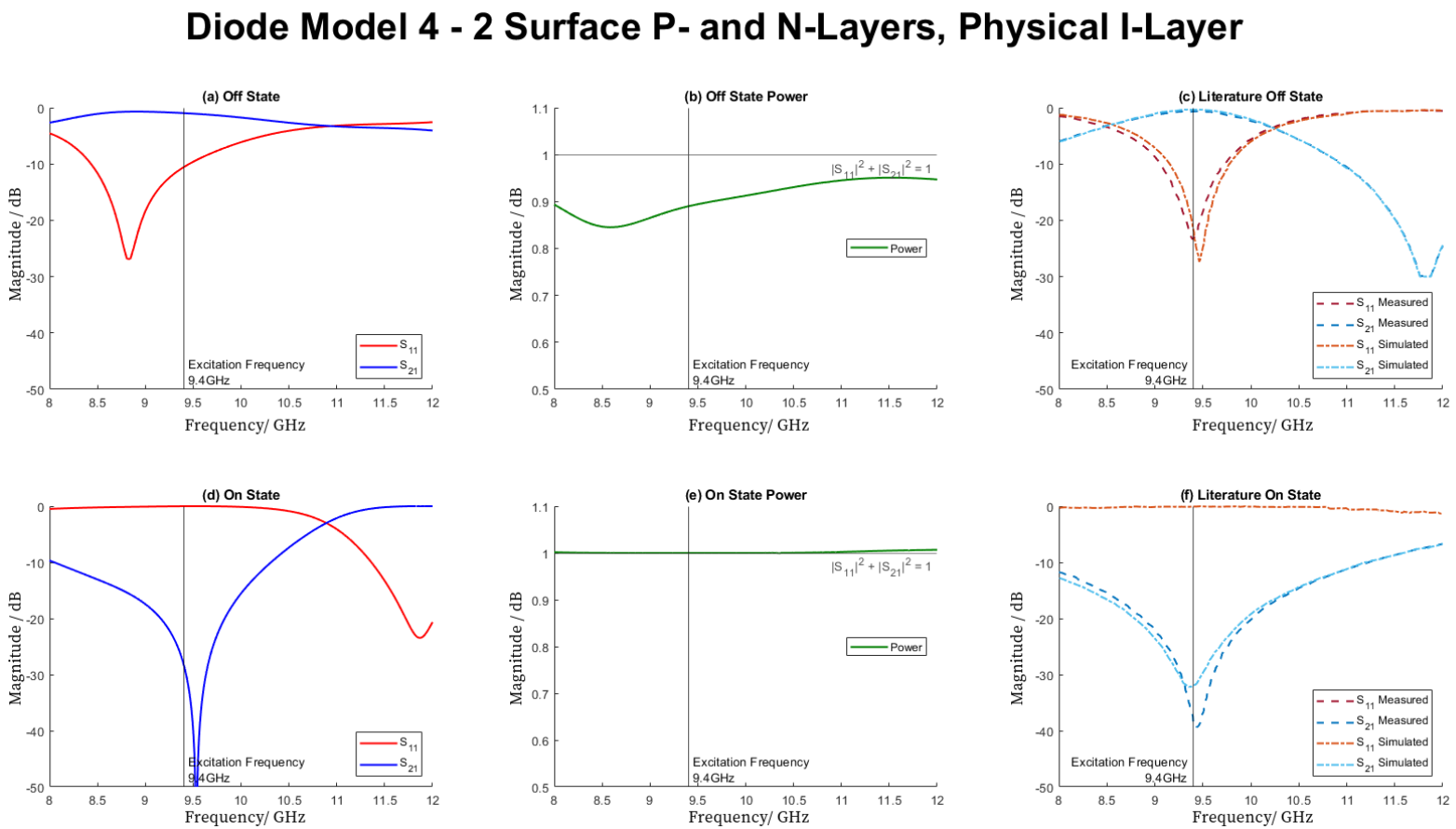

Figure 7.10: Simulation data from the penultimate model in the diode model investigation. (a) The in-band s-parameter response with the diode in the off-state, (b) The total power of the system in-band in the off-state computed from equation 2.65a, (c) The in-band response from a full RxP system in the off-state (both simulation data and experimental measurement) found in [6], (d) the in-band s-parameter response with the diode in the on-state, (e) The total power of the system in-band in the on-state computed from equation2.65a, (f) The in-band response from a full RxP system in the on-state (both simulation data and experimental measurement) found in [6]

The s-parameters presented in figure 7.10 demonstrate that this model is a good representation of an RxP, matching the data found in literature. The model requires further tuning in the off-state (panel (a) figure 7.10) to truly match the published results (panel (c)), but the general behaviour matches well. The on-state (lower panels of figure 7.10) in particular matches the published results well, with the power conservation (panel (e)) remaining optimal.

The off-state behaviour, shown in panel (a) of figure 7.10 is an improvement on previous models. The peak transmission region has progressed towards the excitation frequency with the more detailed definition of the diode layers. This suggest that with greater tuning (including parameters such as layer depth and conductivity), the measured response can be matched exactly. The resonances and noise seen in figure 7.8 (b) have vanished with the more detailed description of the diode construction, however the power loss (figure 7.10 (b)) has slightly increased. This could be attributed to stronger numerical errors experienced by the smaller geometry regions, or could be due to scattering effects within the system, though the loss levels are not significant at this stage.

7.7 Stage 5 - Surface Layer PiN Diode Model

The final stage in this model development replaces the I-layer with another surface layer. By representing the diode itself as three distinct surface layers, each layer can be adapted to reflect different conditions and properties, including doping levels, material composition, and removes the smallest element from the meshing process, allowing an increase in mesh size.

The highlighted blue regions of the mesh in figure 7.11 demonstrate

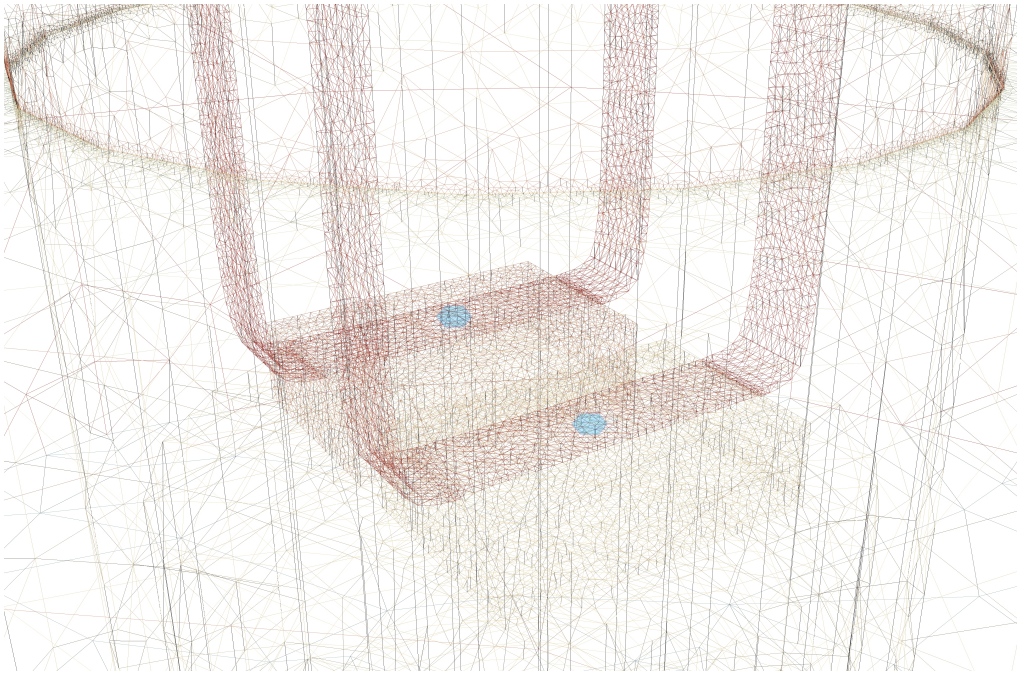

Figure 7.11

the imprinted diode, the shape and location where the diode will be added following meshing. Prior to meshing,the shape of the diode is imprinted onto each of the surfaces that it touches (in this case the bonding ribbons and mounts). Although this imprint has no physical size, it creates a artefact in the mesh that, when referenced in the simulation, defines the shape of the diode. This allows the mesh to be slightly coarser than in the previous model (as shown in table 7.6) at 1 μm . The size of the mesh has increased as it no longer needs to account for the depth of the p- or n-layers since the I-layer is no longer physically present.

The inclusion of the 3 surface layers and their specific properties has increased the runtime of the on-state simulation in comparison to model 4, but allows a more detailed model to be explored. One contributing factor for this is the required inclusion of a fine mesh around the diode region, where previously, in the on-state, this region could be merged with the bulk of the post structure. In the off-state, when comparing the runtime to model 4, there is a marked improvement. Furthermore, the region of

Model 5 - Surface layer diode		
Parameter	**Off-state**	**On-State**
Mesh Size & Refinements	1 mm Bonding ribbons and Mount refined to 1 μm	1 mm Bonding ribbons and Mount refined to 1 μm
SCN Equivalent Edge Length	1.04 μm	1.03 μm
Timestep Size & Number of Timesteps	0.0017 ps 5×10^6	0.0017 ps 4×10^6
Simulation Run Time	18 hours 3 minutes	14 hours 27 minutes

Table 7.6: The key simulation parameters for the final model explored in in the diode model investigation. In this model the diode comprises of 3 surface layers, each customizable to include different material and electronic parameters whilst minimising the requirements for hyperfine meshes around the diode region

refinement around the diode has been reduced, resulting in a larger SCN equivalent edge length and timestep size.

The removal of the physical I-layer, has enabled an increase in timestep size and a reduction in the required number of timesteps across both simulations.

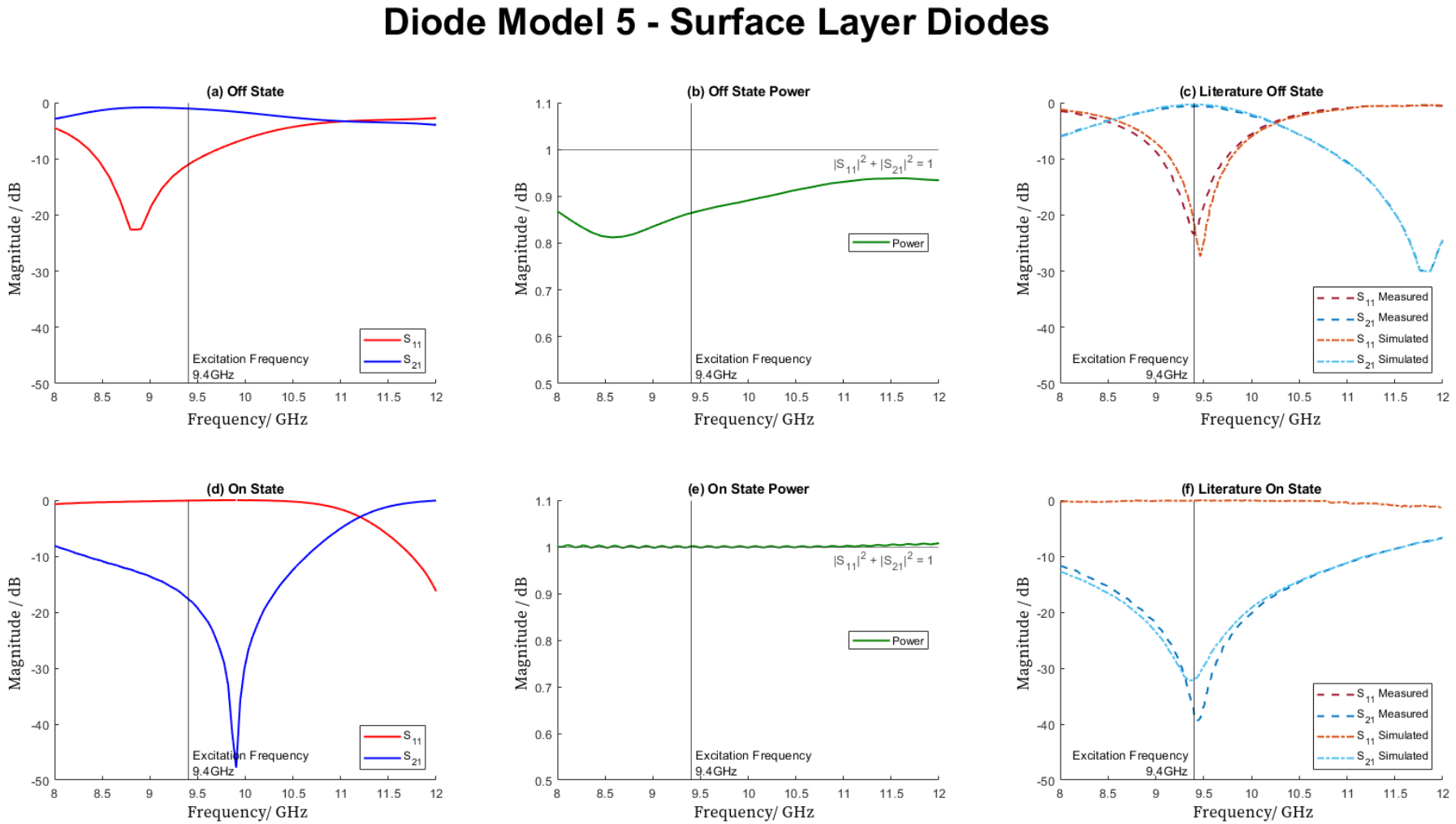

Figure 7.12: Simulation data from the final model in the diode model investigation. (a) The in-band s-parameter response with the diode in the off-state, (b) The total power of the system in-band in the off-state computed from equation 2.65a, (c) The in-band response from a full RxP system in the off-state (both simulation data and experimental measurement) found in [6], (d) the in-band s-parameter response with the diode in the on-state, (e) The total power of the system in-band in the on-state computed from equation2.65a, (f) The in-band response from a full RxP system in the on-state (both simulation data and experimental measurement) found in [6]

The response of this surface layer diode model, shown in figure 7.12 is similar to that of model 4, suggesting that either model is suitable for use in understanding the behaviour of the RxP system. However, the significant advantage of this later model is the reduction of runtime and ability to add increased levels of detail, whilst maintaining accuracy.

Comparing the published results in literature (panels (c) and (f)) with the simulation results from these simulations (panels (a) and (d)) shows that the response is similar and reflects the behaviour of an RxP system. This validates the feasibility and functionality of the model. Further tuning of the model is required to exactly match the published results, but the model developed in this research now allows the semiconductor behaviour of the PiN diode to be modelled in more detail, with the ability to introduce the effects of different dopants, semiconductor heterostructures and doping levels now available.

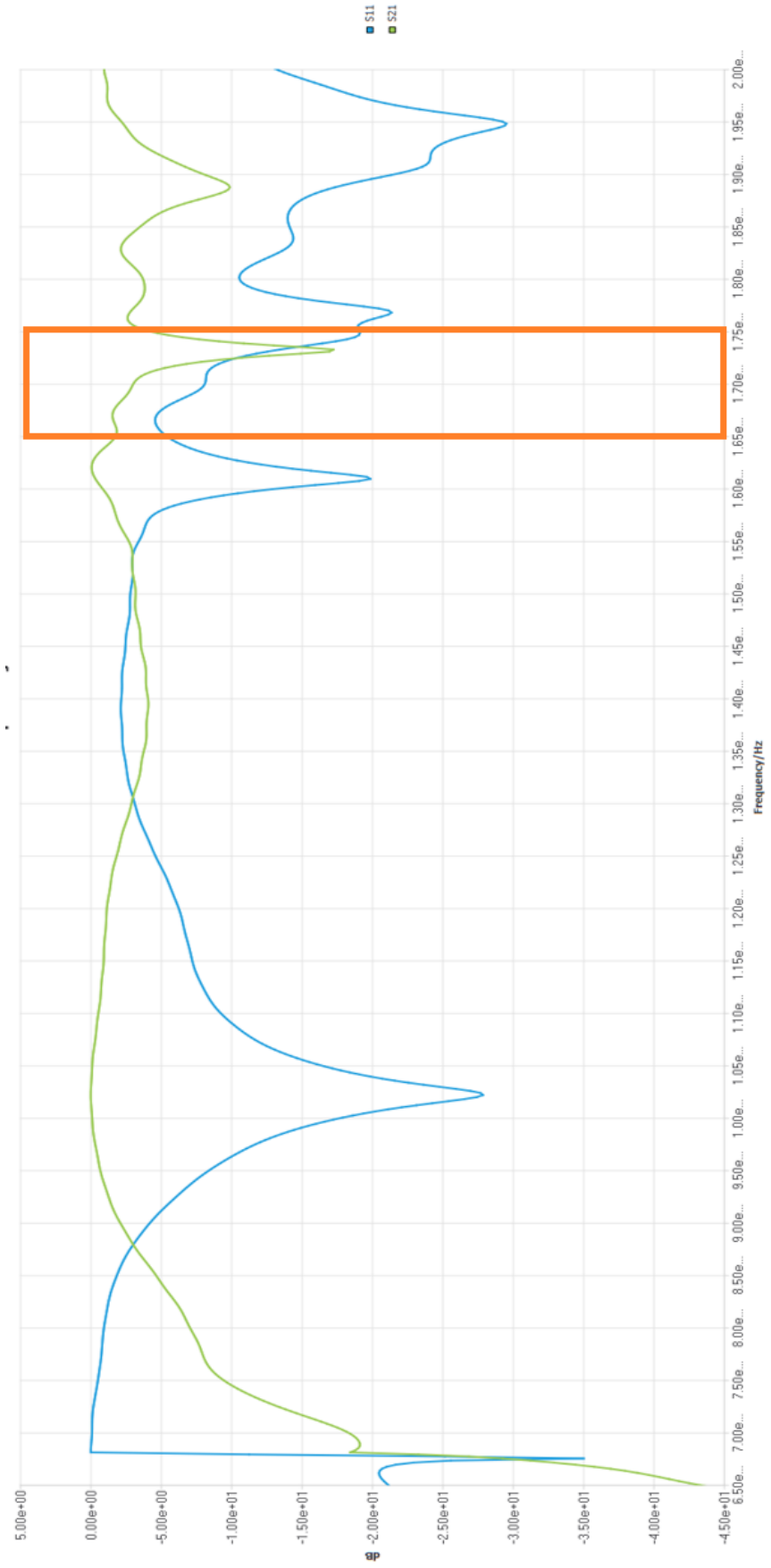

Figure 7.13: Simulation data from the final model in the diode model investigation up to 20 GHz. Studying this data lead to an insight that scattering may be occurring as both S_{11} and S_{21} simultaneously drop around 16.5 GHz, highlighted in the box.

7.8 Scattering Effects

Extending the simulations of the final model up to 20 GHz lead to some interesting insights into the out of band response of an RxP. One area of RxP development that has not been fully understood is how well the system responds above the operating band. The data presented in figure 7.13 shows that as the frequency approaches 16.5 GHz, a simultaneous drop in both S_{11} and S_{21} can be observed when monitoring the input and output of the fundamental TE_{10} mode. This suggests that there is a reduction in the power observed at the output port, since the S-parameters are calculated from the input and output voltages and currents at each port. This reduction is most likely caused by either by absorption by the materials, numerical errors or the scattering effects of the system itself.

Knowing that the metals in this simulation were defined as perfect conductors and that only small amounts of dielectric were present, the most likely cause of this discrepancy was determined to be the scattering effects. Under the right conditions, the fundamental mode can be scattered by the inductive post into another mode with a higher cut-off frequency. The potential modes between 6 and 20 GHz, other than the fundamental mode, are TE_{20} with a cut-off frequency, $f_c = 13.11$ GHz, TE_{01} ($f_c = 14.76$ GHz), and TE_{11}, whose cut-off frequency $f_c = 16.15$ GHz.

Simulating each of these modes showed that the TE_{01} and TE_{20} modes did not experience significant excitation, but some transmission did occur through the TE_{11} mode around 16.5 GHz. To obtain S-parameters for each of these higher modes, the system was excited using the fundamental TE_{10} mode at the input port, but the voltage and current at the output port was measured for the higher mode. Figure 7.14 shows the s-parameters for each of the modes. The data shows that no transmission occurred in the

TE_{20} and TE_{01} modes, since there are no regions where S_{21} exceeds S_{11}. However, when looking at the TE_{11} data, a small region of transmission can be seen around 16.5 GHz, suggesting that the scattering effects caused some of the incident signal to be transmitted through the TE_{11} mode.

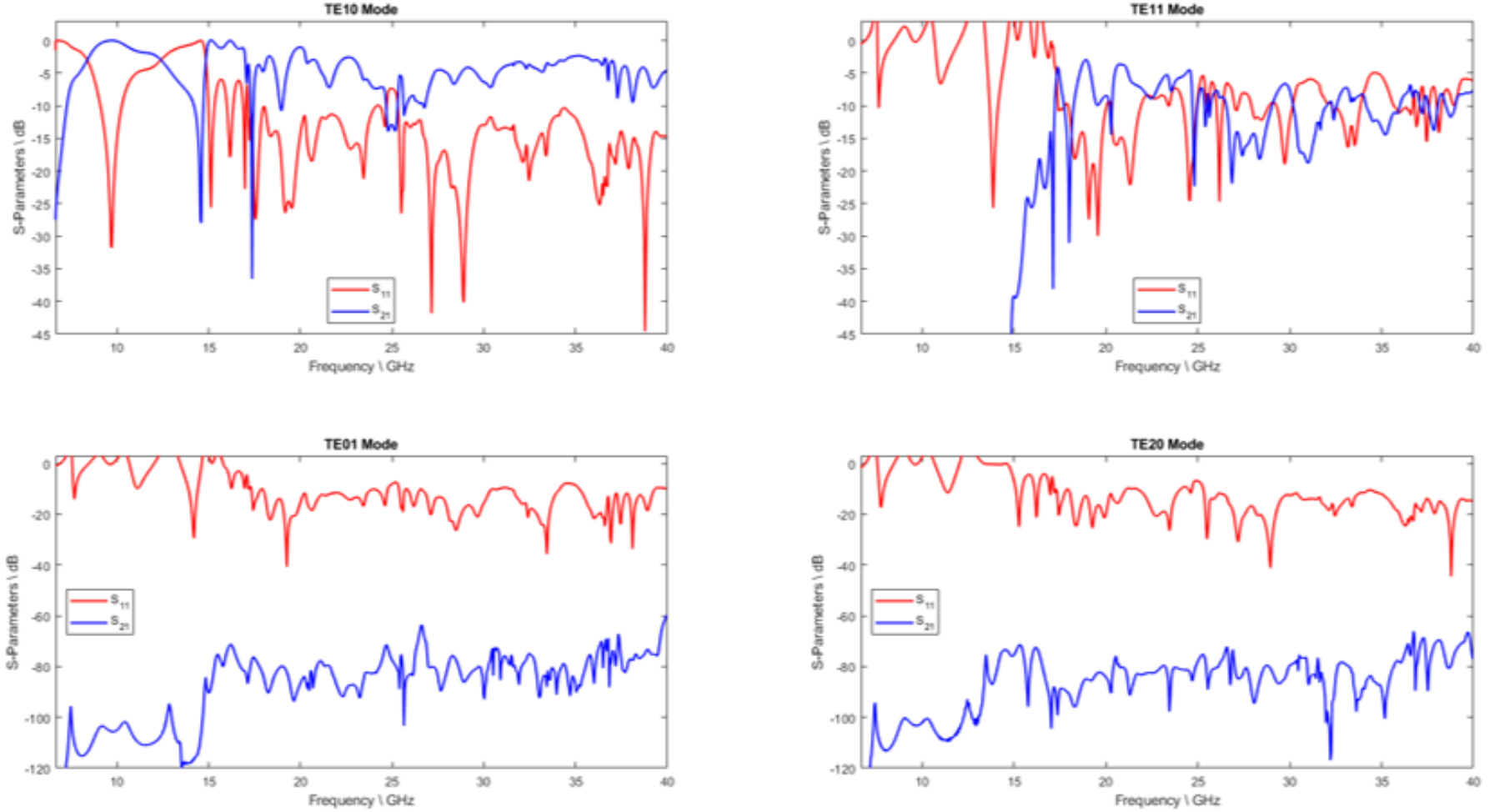

Figure 7.14: Simulation data from the simulations exploring the scattering effects into modes with higher cut-off frequencies. The TE_{01} and TE_{20} modes did not demonstrate any transmission as can be seen by S_{21} remaining significantly below S_{11} and no crossing occurs. However, TE_{11} does demonstrate a small amount of transmission at around 16.5 GHz, suggesting that it has been excited by the scattering effects.

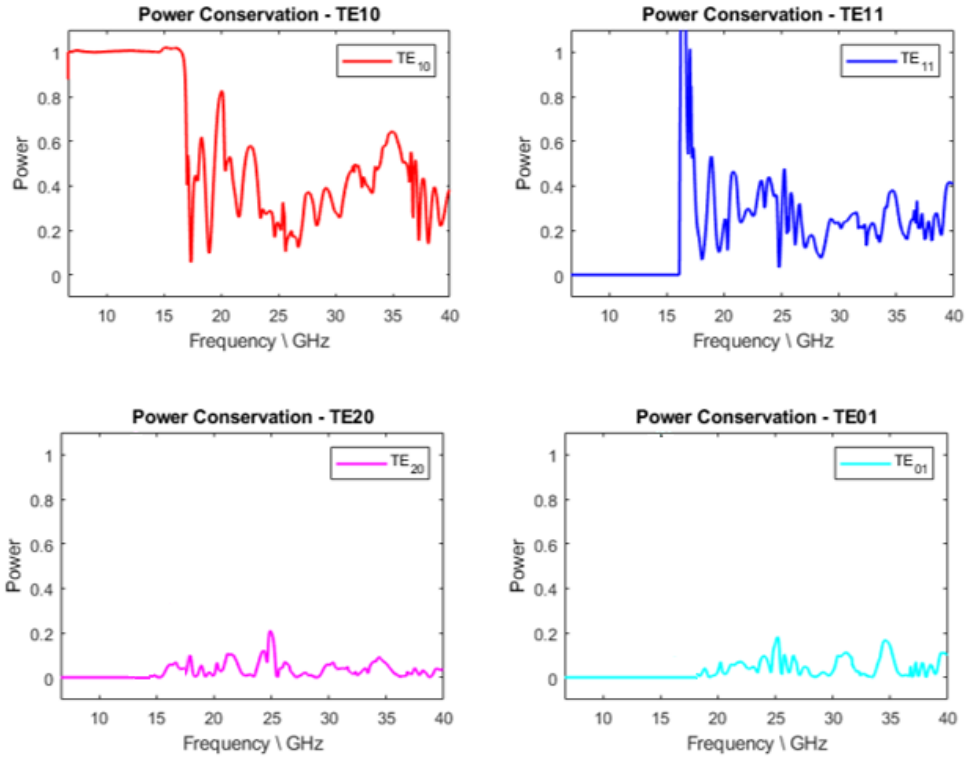

Figure 7.15: Analysing the power present in each mode indicates that transmission only occurs through the TE_{11} mode above 16.5 GHz, but that this is only a small amount of the total power. Transmission does not occur in either the TE_{01} or TE_{20} modes since the proportion of power transmission for each of those modes remains around 0.

Further analysis of the power of the system (see figure 7.15) shows that power transmission does in fact occur through the TE_{11} mode. Power is preserved as the wave propagates through the system, i.e. we have a lossless network, if:

$$|S_{11}|^2 + |S_{21}|^2 = 1 \tag{7.1}$$

Analysing the power transferred through the fundamental mode in the first panel of (fig 7.15) it can be seen that this relation holds true until the cut-off frequency of the TE_{11} mode, where the power transmission through the fundamental mode starts to diminish. Similarly, in the second panel, the power transferred from the fundamental TE_{10} mode and exiting the waveguide in the TE_{11} mode increases drastically at a similar frequency,

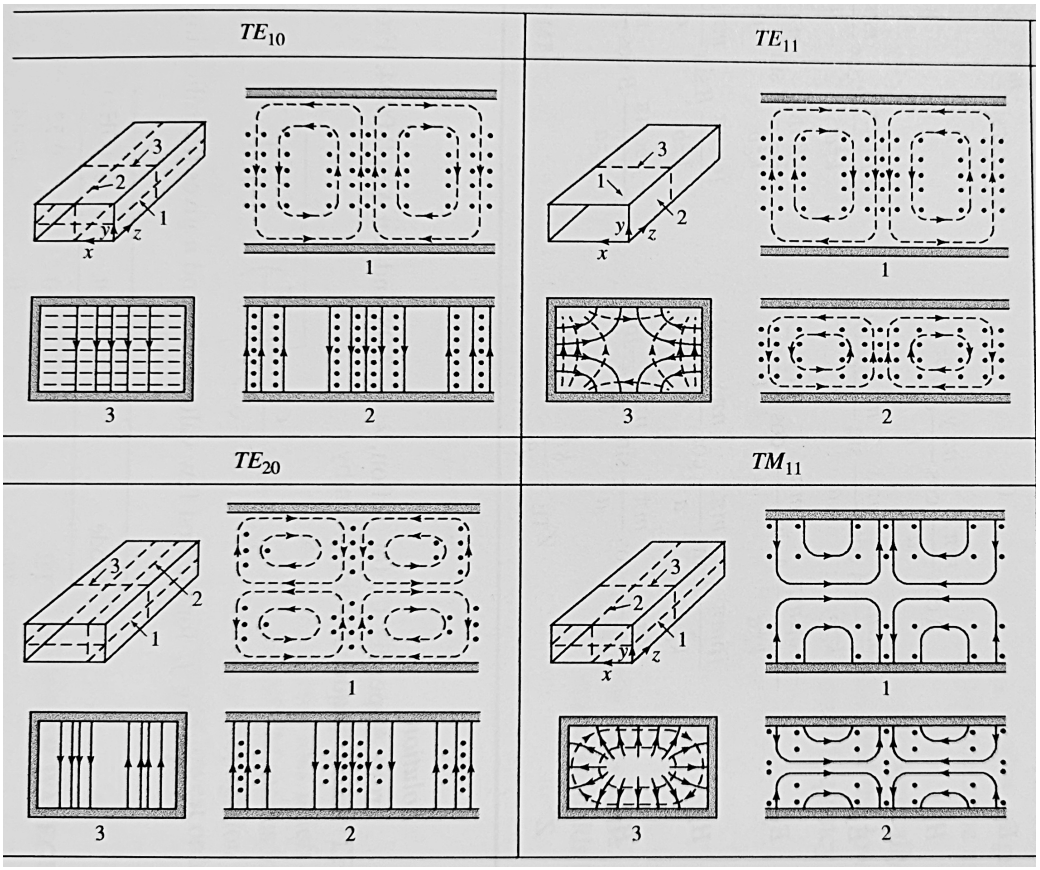

Figure 7.16: Field lines of some of the lower order modes of a rectangular waveguide [24]. Comparing the field lines along the x-z plane for the TE_{10} and TE_{11} modes shows that they are identical, allowing coupling between the modes to occur.

indicating that scattering has excited this higher mode. Averaging the fluctuations in the data above the cut-off frequency of the TE_{11} mode suggests that approximately 20% of the system power is scattered into this mode. Moreover, no significant transmission occurs through the TE_{20} or TE_{01} modes, since their proportion of power transmission remains close to zero.

Despite the TE_{20} and TE_{01} modes having lower cut-off frequencies, coupling into those modes as a result of the scattering effects does not occur. This is likely due to the fact that they do not share common modal characteristics with the fundamental mode. Looking at the cross section of the TE_{10} and TE_{11} modes along the x-z plane (figure 7.16), they both share the same field line pattern, in addition to the same m modal number. The

sharing of the field pattern allows the energy to be coupled easily between the modes at sufficiently high frequency. Although the TE_{10} and TE_{20} modes both also share a similar field line pattern along the y-z plane, the presence of the inductive post in the centre of this plane disrupts the field, preventing coupling from occurring.

7.9 Conclusions

This chapter has explored the development of a diode model from a simple switching block to a highly detailed, 3 surface layer representation. Each model has been compared to their predecessor to understand how increasing the level of detail and proximity to the real world component has an effect on the outcomes, whilst ensuring that the response is physical through qualitative comparisons to published literature.

Ultimately, the final model with the full surface layer representation provided the best balance between precision and performance. Either of the final two models could be used to understand the diode behaviour - that is with or without the physical I-layer - however the improvements in runtime and adaptability of the surface layer model offer deeper insight to the device.

A note considering the loss in power that presented itself in some of the models. The power loss was only prevalent in the off-state model and even then only when two diodes were present. This has lead to the conclusion of a capacitive interaction between the two diode structures, something that will be investigated in future research. The interaction and loss may result from the parallel positioning of the 2 diodes, and may be solved by a slight offset between the two of them, a modification not explored in this research. Furthermore, the relative permittivity of the diodes

themselves may play a role in this interaction, suggesting different diode materials may perform better and minimise this loss.

Developing the model from a simple switching block through to a 3 layer model in a progressive manner, as was conducted in this chapter, provided helpful insight into the causes and effects of the inclusion of certain elements within the RxP system. The response of the system is highly sensitive in particular to the constituent parts of the diode, so a deeper understanding of how this varies as the model is built is informative. The differences caused by introducing the bonding ribbons in place of the connecting rods allowed the cause of some artefacts to be inferred and further research into whether the shape and path of these bonding ribbons can influence the behaviour of the system could be instructive.

The real power of this model lies in the ability to precisely detail the electronic and material properties of each of the individual layers present in the PiN diode. Understanding the impact of different doping levels, dopants, sizes, configurations and more will provide invaluable insight in the development and advancement of these technologies in the future.

The next and final chapter will summarise the key findings and results from the research presented in this thesis. It will start with a brief overview of each of the chapters present here, before discussing the most important results found in this research. Finally, the chapter will end with some suggestions for further developments and avenues of research for future works based on the findings of this research.

Chapter 8

Conclusions and Future Research Directions

This chapter gives a comprehensive overview of the contents of this thesis and the success achieved throughout this research. In addition to summaries of each chapter, the key results of this research will be highlighted, along with a discussion of their significance. Finally, a conversation of the place of this research in the wider world of RF modelling will add perspective and allow ideas for future research, study and development, and their rationale, to be suggested.

8.1 Chapter Summaries

The first chapter of this thesis presented the problem that this research set out to solve. Chapter 1 started with a brief background and overview of RF systems and their importance in the increasingly connected modern world. It then introduced waveguides, some of the most common transmission lines in RF systems alongside the physics behind their operation. The problem

statement of this research subsequently followed, preceding an overview of the main aims of this project and an outline of the thesis as a whole.

The first two theory chapters arrived in chapters 2 and 3. Chapter 2 presented the physics behind electromagnetic wave propagation, with additional focus placed on Maxwell's equations and their manifestations. Particular emphasis was placed on waveguide theory, as this is the foundation of this research. Chapter 2 also introduced elements of RF and microwave engineering, fundamental electronics and the microwave analysis that was used to understand the data produced in the subsequent investigations. S-Parameters are explained in detail as the principle analysis tool for this research. Further detail is given on transmission lines, with a discussion of how they find an analogy to circuits and an indication of their use as the basis of some modelling methods offered.

A review of the prominent RF modelling method of the current era forms the majority of chapter 3. Covered in this chapter are the workings of the Finite Difference Time Domain (FDTD), Finite Element Analysis (FEA / FEM), Transmission Line Matrix Method (TLM), Method of Moments (MoM) and Unstructured Transmission Line Modelling Method (UTLM). The limitations of these methods are mentioned as well as a justification for using UTLM in this research in an effort to avoid the common problem of staircasing that arises from the discretisation of the problem space into a cubic mesh.

Chapter 4 presents the first significant results from this research. It covers a thorough and comprehensive investigation into how variations in the physical dimensions of each of the passive components within the RxP system, as well as the inclusion of the components themselves, can impact the s-parameters of the system.

The second half of this thesis focussed on the full RxP system, including the effects of the non-linear behaviour of the PiN diode. This part of the thesis started with a presentation of some of the main principles and theory behind semi-conductor physics (Chapter 5). This knowledge is useful to understand the design, function and behaviour of the diode within the RxP system. This chapter covers the concepts of p-n junctions, PiN diode uses and manufacture in addition to the electron-hole mobility and how it can be used to calculate the conductivity of a device.

A review of the modelling techniques used to model RxPs and semiconductor PiN diodes for RF and microwave applications is shown in chapter 6. Some of the more prominent methods in use today for modelling PiN diodes have been the IBIS model and the SPICE model. These are discussed, along with how suitable they would be for inclusion into the UTLM solver. Finally, an explanation is offered to why UTLM alone was selected as the preferred method for modelling these useful devices.

The full RxP simulation required the model of a PiN diode to be included in two places. To ensure the accuracy of this model, chapter 7 shows the methodical approach taken of constructing the model of a PiN diode. Starting with a simple switching block and adding increasingly more detail, the final, complete model of a PiN diode was achieved in such detail that each of the three layers of the PiN diode were defined individually. This allows in depth analysis and modification of the PiN diode, even down to the doping level present in each layer, by considering the conductivity of the layer. The full model was then used to explore the "above band" response of the RxP system, where scattering effects were found to occur. It was found that the scattering caused by the inductive post within the RxP system causes the incident power to be scattered into other, higher order modes.

8.2 Key Results

The research presented in this thesis offers a considerable advancement on the model of an RxP receiver protector system in 3 principle ways:

- An in depth piecewise analysis of the components comprising an RxP system and how their parameters can affect the performance of the system as a whole.
- Advancement on the model of a PiN diode within the system, model in fine detail to the micron scale.
- Application of the advanced model to two different areas to provide deeper insight into the behaviour of the system and how the material properties can change the response.

8.2.1 Piecewise Analysis

Chapter 4 studies in detail how the parameters of the components of the RxP system can impact the overall response of the system. The methodical and thorough approach applied in this investigation starts with an empty waveguide to establish a baseline response and that it is in agreement with the expected response. Each subsequent study adds one additional component to the RxP system. Once the component is added, a series of simulations are conducted where the parameters of that component, e.g. the diameter of the inductive post or the depth of protrusion of the upper boss, are varied to facilitate a more detailed understanding of how the behaviour of the system is dependant on these properties.

In this thesis, the addition of the inductive post, upper boss, lower cavity (and consequently elongation of the inductive post), and PTFE tape

were considered initially. The PiN diode and the encasing diode package were investigated in chapter 7.

The component that has the most significant influence on the overall behaviour of the system is predictably the inductive post. After establishing a very good approximation for the cylindrical post to minimise resource requirements, an investigation was conducted into the effects of changing the diameter of the post. This concluded that there is an optimum diameter for the post since increasing the diameter naturally stretches the reflection region to higher and higher frequencies. However, if too large, the thicker posts also introduce a secondary reflection region at higher frequencies around 30 GHz.

The next component investigated was the upper boss. Investigations were conducted into the effects of the boss diameter and the depth of protrusion into the waveguide. As with the post, the dimensions of the upper boss need to be fine tuned in order to achieve the desired performance. Larger and more protruding upper bosses increased the scattering effects significantly, but caused a variety of other relics to appear, including additional regions of transmission and reflection that could prove undesirable.

Finally, the diameter of the cavity at the bottom of the waveguide, surrounding the inductive post was introduced. This increased the scattering and interaction with the post, though also held the potential to introduce new paths of propagation and regions of transmission if too large.

8.2.2 Model Advancement

The addition and advancement of the PiN Diode model is addressed in chapter 7. Following a similar approach, the PiN diode is developed across 5 stages. The investigation starts with a simple, homogenous block of ma-

terial to represent the diode, connected with a thin rod to the inductive post above, mounted on a pedestal and encased in the diode package. The block is defined as a perfect metal in the on-state and dielectric silicon in the off-state, to model the switching behaviour of the diode in the RxP system. Across the five stages, this simple block and rod model transforms initially into two blocks, connected by ribbons, before it ultimately becomes a micron scale, three layer representation of the PiN diode connected by ribbons. This final model allows each of the P-, I- and N- layers of the diode to be defined individually and their properties governed by the material properties of the layer, including the doping level of the semiconductors.

As the model of the diode was developed, certain features had an obvious impact on the response of the system. The inclusion of the second diode, or more notably the second connecting rod in close proximity, had a profound affect on the output of the system, with the frequency of the regions of maximum and minimum transmission shifted noticeably. Additionally, the scattering caused by the second connecting rod in close proximity with the first caused a remarkable ($\approx 20\%$) increase in the power "loss" of the system. This was later shown to be scattering into higher order modes (see chapter 7).

As the model development progressed, the maximum response regions returned towards their expected frequency, with the addition of the P- and N- type semiconductor layers having the next strongest impact. It is clear that when the P- and N- layers are introduced in stage 4 of the diode model, that the response of the system again shifts, but this time, towards the excitation frequency.

The final model demonstrates improvements on existing techniques in two ways, the enhanced level of detail in which it is now possible to model PiN diodes, in addition to the improved speed of the simulations.

Discussions with industry advisors suggested that these simulations can take in excess of 3 days to complete. The simulations using the most detailed model in this research completed in a little over half that time.

The final model of a three layered PiN diode most closely reflected the expected response of the system. Given that RxP systems in practice require a significant amount of time spent on tuning them so that they exhibit the desired response, by varying the parameters explored in chapter 4 (more commonly adding PTFE tape or changing the upper boss depth), the proximity of the response of the final model to the perfectly tuned response can be considered a great success.

Furthermore, the level of detail that is achievable with this model when defining and exploring the composition of the diode could be of utmost importance in the advancement of this field in future. The ability to define the material properties of each individual diode layer opens the door to new explorations even within the same material space, allowing an examination of how the different doping levels and the elements of the dopants can influence the response of the system.

8.2.3 Application

Analysing the data from the diode model development investigation, it was clear that there was some power loss in the system. Further exploration of this comprises the latter part of chapter 7.

Using the most advanced model introduced in chapter 7, it was possible to explore the hypothesis that the power loss observed in the data was in fact scattered rather than lost. The investigation shown in this chapter demonstrates that the inductive post is capable of scattering the incident signal in the off-state into other modes with higher cut-off frequencies. This

scattering behaviour does not occur into every higher mode, but relies on some symmetry with the incident mode. Despite having a higher cut-off frequency, it was found that scattering occurred into the TE_{11} mode preferentially to the TE_{01} and TE_{20} modes. The TE_{11} mode shares the same m modal number, consequently allowing scattering into this mode to occur, and it is believed that even higher modes that share the same m modal number will also facilitate scattering at higher frequencies, though more research is needed.

In addition, alternative compositions of the PiN diode were discussed. Changing the elemental composition, and consequently the electronic properties of the PiN diode, changes the behaviour of the system overall. The conductivity of the layers of the PiN diode have a significant part to play in the strength of the response. It is highly important to match the operating band of the waveguide with the regions of strongest response provided by the PiN diode. Further research into this is required. The cost and availability of the dopants and semiconductor heterostructures will dictate which combinations are practical in industry. Furthermore, the application of interest for the semiconductor device (PiN diode) will also help establish whether certain compositions are feasible. If the maximum response of the PiN diode falls at a frequency outside the operating band of the RxP system, the RxP will be unable to protect the receiver as desired. It is hoped that the model presented in this thesis may lay the foundations for new research into the applicability of semiconductor compositions for RF applications.

8.3 Further Development and Research Ideas

Further expansions on this research could follow one of two main streams: application and advancement.

8.3.1 Advancement

Advancement of the model can come in the form of a more detailed consideration of the RxP system as a whole. Practical RxP systems often have multiple stages working in unison to prevent the incident signal propagation in the on-state. Additionally, not every stage of an RxP contains identical core components, so a thorough examination of each stage configuration could be informative.

Moreover, understanding how the PiN diode characteristics guide the response of the system is crucial in the development of RxP systems. This research has commenced the study of the PiN diode with different elemental compositions, but more work is needed to explore the consequences of properties such as layer thickness, doping level, manufacturing tolerances, and even different configurations. Furthermore, building up a bank of different diode compositions and configurations could be beneficial in the design of future RxP systems. Identifying which PiN diode responds optimally for each application can only strengthen the capabilities of the next generation of RxP systems.

The switching behaviour of the PiN diode in this research was explored by using two simulations and definitions of the PiN diode to mimic the on- and off states of the diode. This non-linear behaviour is the primary reason for the use of PiN diodes in their systems. Being able to model this non-linear switching behaviour in a single simulation and observe the

changes in a single simulation is a logical next step in the development of this model.

Further study into the higher mode scattering could also lead to technological advancements to help better deal with the power that passes through at higher frequencies, through the inclusion of mode suppression features and novel features in the RxP system.

8.3.2 Alternatives to Silicon Diodes

The most common configuration for a PiN diode in an RxP system uses a combination of doped and undoped silicon layers (see chapter 5). However, a multitude of other semiconductor heterostructures exhibit similar characteristics and can be used to replicate the switching behaviour exhibited by the PiN diode.

One significant obstacle thus far of employing these alternative configurations in an RxP system has been the need to represent them in models using approximations or equivalent circuits. The triple layered model presented in this research opens the door to being able to examine the behaviour and implementation of alternative PiN diodes within the RxP system and garner a deeper insight as to how the elemental composition of the PiN diode can affect the behaviour of the system in both the off- and on-states.

Further research into the behaviour of different elemental configurations of the PiN diode within the RxP system is now possible with this new model, though is beyond the scope of this thesis. Future works into this area will likely reveal that the main observable difference will be in the off-state and will affect the frequency of the transmission and reflection regions in a similar way to the diameter of the inductive post or the depth

of the threaded boss. Some elemental configurations may broaden the response region of the diode, leading to a wider transmission (pass) band in the off-state, while others may shift the frequency of maximum response to higher or lower frequencies.

With the high level of customisability provided by the diode model in this research, the impact of PiN diodes can be explored throughout the world of RF, including in microwave and other electrical and electronic systems. It is hoped that, in future, this model can be developed further to study some of the more interesting and intricate features of semiconductors, including how minority carrier lifetimes affect the response, modelling the thermal aspects of semiconductors and consequently exploring "burn-out".

Studying the presence of the switching behaviour of the PiN diode in other applications would expand the understanding of the operation of those systems. The switching of PiN diodes and PN junctions, as discussed in chapter 5 is ubiquitous in the modern, increasingly connected world, where initial simulations of systems and devices is a critical stage in the development process. Modelling the PiN diodes in solar cells could help improve the efficiency of those systems, modelling the diodes used in laser generation could help generate more focussed beams. Even within the world of RF, PiN diodes are used in more ways than just RxP systems.

8.4 Concluding Remarks

Modelling is becoming an ever-increasingly important part of the modern manufacturing process. In addition to reducing prototype design time, wastage and overall production cost, modelling also helps ensure that the risks of electromagnetic interference are mitigated against and that, with the ever increasing level of connectivity in the world, systems, devices and

users remain safe and uninhibited.

The ability to model such a critical and complex component in such detail cannot have its importance understated. It is the hope of this research and this researcher that the information detailed in this thesis will help inform and inspire both current and future generations of modelling engineers, designers and RF engineers and that it is just the start of future study and development into modelling these pivotal pieces of our modern world.

Bibliography

[1] I. Scott, V. Kumar, S. Greedy, D. Thomas, C. Christopoulos, and P. Sewell, "Time-domain modelling of active electrically fine features in tlm," pp. 284–287, 01 2011.

[2] M. Golio, M. N. Sadiku, J. Golio, M. Pecht, A. D. Kraus, J. T. Nessmith, J. C. Wiltse, A. D. Kucar, N. E. Buris, J. Bartlett, *et al.*, *RF and microwave applications and systems*. CRC press, 2018.

[3] F. Dowla, *Handbook of RF and wireless technologies*. Elsevier, 2003.

[4] N. Fourikis, *Advanced array systems, applications and RF technologies*. Academic Press, 2000.

[5] R. Decesari, "The use of radio frequency systems in the marine environment," in *OCEANS '85 - Ocean Engineering and the Environment*, pp. 1302–1305, 1985.

[6] N. Farrington, B. Coaker, M. Dowthwaite, G. Fletcher, and K. Newsome, "An overview of modern radar receiver protection technology and the development of electromagnetic models for the design of pre-tr cell waveguide protectors," in *April 2011 ARMMS conference*, (Steventon), 2011.

[7] N. Roberts, "A review of solid-state radar receiver protection devices," *Microwave Journal*, vol. 34, p. 121, Feb. 1991.

[8] R. F. Bilotta, "Receiver protectors: A technology update," *Microwave Journal*, vol. 40, no. 8, 1997.

[9] D. C. Broderick, "Gaseous-solid state power limiter," May 3 1966. US Patent 3,249,899.

[10] B. Coker, "Radar Receiver Protection Technology," *Microwave Journal*, no. August, 2007.

[11] "PIN Limiter Diodes in Receiver Protectors - Accessed at http://www.skyworksinc.com/uploads/documents/200480C.pdf," tech. rep.

[12] R. P. Feynman, *Feynman Lectures on Physics. Volume 2: Mainly Electromagnetism and Matter*. 1964.

[13] G. L. Matthaei, L. Young, and E. M. Jones, "Microwave filters, impedance-matching networks, and coupling structures," 1980.

[14] Newsome, Keith and Stimson, Gary and Mellor, Chris and Vukovic, Ana and Benson, Trevor, "Discussions with key members of staff at Teledyne e2V, manufacturers and suppliers of RF Systems." Personal Communications, 2018. Site Visit, 18th December 2018.

[15] A. Taflove and S. Hagness, *Computational electrodynamics: the finite-difference time-domain method. 2nd ed*, vol. 67–106. 06 2000.

[16] C. Christopoulos, "The historical development of tlm (transmission line modelling)," in *IEE Colloquium on Transmission Line Matrix Modelling - TLM*, pp. 1/1–1/4, 1991.

[17] A. Vukovic, "Investigation of mutual coupling in vivaldi antenna arrays installed in airborne radomes," *IET Conference Proceedings*, pp. 772 (4 pp.)–772 (4 pp.)(1), January 2018.

[18] P. Sewell, J. G. Wykes, T. M. Benson, C. Christopoulos, D. W. Thomas, and A. Vukovic, "Transmission-line modeling using unstructured triangular meshes," *IEEE Transactions on Microwave Theory and Techniques*, vol. 52, no. 5, pp. 1490–1497, 2004.

[19] P. Sewell, T. M. Benson, C. Christopoulos, D. W. Thomas, A. Vukovic, and J. G. Wykes, "Transmission-line modeling (TLM) based upon unstructured tetrahedral meshes," *IEEE Transactions on Microwave Theory and Techniques*, vol. 53, no. 6 I, pp. 1919–1928, 2005.

[20] P. D. Sewell, T. M. Benson, A. Vukovic, and X. Meng, "Complexity reduction of multiscale utlm cell clusters," *IEEE Journal on Multiscale and Multiphysics Computational Techniques*, vol. 2, pp. 18–28, 2017.

[21] P. D. Sewell, T. M. Benson, C. Christopoulos, D. W. P. Thomas, A. Vukovic, and J. G. Wykes, "Implicit element clustering for tetrahedral transmission-line modeling (tlm)," *IEEE Transactions on Microwave Theory and Techniques*, vol. 57, no. 8, pp. 2005–2014, 2009.

[22] A. Vukovic, P. Sewell, T. Dimitrijevic, B. Lang, S. Rihani, K. Boylan, G. Berry, N. Hattasan, D. Moodie, J. Rawsthorne, and M. Robertson, "Unstructured transmission line modelling (tlm) method for modelling of advanced photonic structures," in *2023 16th International Conference on Advanced Technologies, Systems and Services in Telecommunications (TELSIKS)*, pp. 81–84, 2023.

[23] P. Sewell, J. Wykes, A. Vukovic, D. Thomas, T. Benson, and C. Christopoulos, "Multi-grid interface in computational electromagnetics," *Electronics Letters*, vol. 40, no. 3, p. 1, 2004.

[24] D. Pozar, *Microwave Engineering, 4th Edition*. Wiley, 2011.

[25] J. Fleming, *The Principles of Electric Wave Telegraphy and Telephony*. Longmans, Green, 1919.

[26] D. J. Griffiths, *Introduction to electrodynamics*. Pearson, 2013.

[27] C. R. Nave, "Hyperphysics."

[28] T. S. Microwave, "High performance microwave interconnect products: Dielectric options."

[29] User:Waldyrious, "Diagram illustrating the relationship between the wavenumber and the other properties of harmonic waves - accessed at https://commons.wikimedia.org/wiki/file:commutative_diagram_-of_harmonic_wave_properties.svg."

[30] L. Nickelson, *Electromagnetic Theory and Plasmonics for Engineers*. Springer, 2019.

[31] C. Nantista, "Overmoded waveguide components for high-power rf," vol. 691, pp. 263–271, 12 2003.

[32] N. Marcuvitz, *Waveguide Handbook*. Institution of Electrical Engineers, 1986.

[33] F. Caspers, "Rf engineering basic concepts: S-parameters," *arXiv preprint arXiv:1201.2346*, 2012.

[34] R. E. Collin, *Foundations for microwave engineering / Robert E. Collin.* IEEE Press series on electromagnetic wave theory, 2nd ed. ed., 2001.

[35] T. S. Bird, "Definition and misuse of return loss [report of the transactions editor-in-chief]," *IEEE Antennas and Propagation Magazine*, vol. 51, pp. 166–167, April 2009.

[36] T. S. Bird, "Definition and misuse of return loss [report of the transactions editor-in-chief]," *IEEE Antennas and Propagation Magazine*, vol. 51, no. 2, pp. 166–167, 2009.

[37] L. Sevgi, "Electromagnetic problems and numerical simulation techniques," *tutorial presentation) CSCC*, vol. 99, pp. 4–8, 2006.

[38] R. F. Harrington and J. L. Harrington, *Field Computation by Moment Methods*. Oxford University Press, Inc., 1996.

[39] B. Lai, X.-W. Zhao, Z.-J. Su, and C.-H. Liang, "Higher-order mom analysis of the rectangular waveguide edge slot arrays," *IEEE Transactions on Antennas and Propagation*, vol. 59, no. 11, pp. 4338–4341, 2011.

[40] A. Aydoğan, "A hybrid mom/mm method for fast analysis of e-plane dielectric loaded waveguides," *AEU - International Journal of Electronics and Communications*, vol. 100, pp. 9–15, 2019.

[41] A. Sangster and H. Wang, "A combined fem/mom technique of coupling and radiating apertures in rectangular waveguide," *IEEE Transactions on Magnetics*, vol. 31, no. 3, pp. 1554–1557, 1995.

[42] M. Sadiku, "A simple introduction to finite element analysis of electromagnetic problems," *IEEE Transactions on Education*, vol. 32, no. 2, pp. 85–93, 1989.

[43] R. Courant, "Variational methods for the solution of problems of equilibrium and vibrations," 1943.

[44] W. Carpes, G. Ferreira, A. Raizer, L. Pichon, and A. Razek, "Tlm and fem methods applied in the analysis of electromagnetic coupling," *IEEE Transactions on Magnetics*, vol. 36, no. 4, pp. 982–985, 2000.

[45] K. Ise, K. Inoue, and M. Koshiba, "Three-dimensional finite-element solution of dielectric scattering obstacles in a rectangular waveguide," *IEEE Transactions on Microwave Theory and Techniques*, vol. 38, no. 9, pp. 1352–1359, 1990.

[46] H. Soleimani, Z. Abbas, K. Khalid, N. Yahya, and H. Soleimani, "Determination s-parameters of ptfe at x-band frequency using fem modeling rectangular waveguide," *European Journal of Scientific Research*, vol. 39, no. 1, pp. 105–110, 2010.

[47] K. Yee, "Numerical solution of initial boundary value problems involving maxwell's equations in isotropic media," *IEEE Transactions on Antennas and Propagation*, vol. 14, no. 3, pp. 302–307, 1966.

[48] D. M. Sullivan, *Electromagnetic simulation using the FDTD method*. John Wiley & Sons, 2013.

[49] U. S. Inan and R. A. Marshall, *Numerical electromagnetics: the FDTD method*. Cambridge University Press, 2011.

[50] S. Gedney, *Introduction to the finite-difference time-domain (FDTD) method for electromagnetics*. Springer Nature, 2022.

[51] A. P. Zhao and A. Raisanen, "Application of a simple and efficient source excitation technique to the fdtd analysis of waveguide and microstrip circuits," *IEEE Transactions on Microwave Theory and Techniques*, vol. 44, no. 9, pp. 1535–1539, 1996.

[52] Y. Hao and R. Mittra, *FDTD modeling of metamaterials: Theory and applications*. Artech house, 2008.

[53] E. A. Semouchkina, G. B. Semouchkin, M. Lanagan, and C. A. Randall, "Fdtd study of resonance processes in metamaterials," *IEEE*

transactions on microwave theory and techniques, vol. 53, no. 4, pp. 1477–1487, 2005.

[54] X. Meng, P. Sewell, S. Phang, A. Vukovic, and T. Benson, "Modeling curved carbon fiber composite (cfc) structures in the transmission-line modeling (tlm) method," *IEEE Transactions on Electromagnetic Compatibility*, vol. 57, 02 2015.

[55] P. Johns, "A symmetrical condensed node for the tlm method," *IEEE Transactions on Microwave Theory and Techniques*, vol. 35, pp. 370–377, Apr 1987.

[56] T. Jalali, K. Rauscher, A. Mohammadi, D. Erni, C. Hafner, W. Bächtold, and M. Shoushtari, "Efficient effective permittivity treatment for the two-dimensional finite difference time-domain simulation of photonic crystals," *Journal of Computational and Theoretical Nanoscience*, vol. 4, pp. 644–648, 05 2007.

[57] S. Dey and R. Mittra, "A locally conformal finite-difference time-domain (fdtd) algorithm for modeling three-dimensional perfectly conducting objects," *IEEE Microwave and Guided Wave Letters*, vol. 7, no. 9, pp. 273–275, 1997.

[58] Y. Zhao, P. Belov, and Y. Hao, "Accurate modelling of left-handed metamaterials using a finite-difference time-domain method with spatial averaging at the boundaries," *Journal of Optics A: Pure and Applied Optics*, vol. 9, p. S468, aug 2007.

[59] J. C. Liu, D. M. Liu, and T. M. Shao, "Fdtd simulation on laser-induced enhancement of electric field in the near-field apertureless probe system," *Laser Physics Letters*, vol. 9, p. 511, may 2012.

[60] Y. Diao, L. Zhang, D. Shi, and A. Hirata, "An effective edge conductivity for reducing staircasing error in induced electric field computation for low-frequency magnetic field dosimetry," *Physics in Medicine and Biology*, vol. 67, p. 215011, oct 2022.

[61] P. D. Sewell, T. M. Benson, C. Christopoulos, D. W. P. Thomas, A. Vukovic, and J. G. Wykes, "Implicit element clustering for tetrahedral transmission-line modeling (tlm)," *IEEE Transactions on Microwave Theory and Techniques*, vol. 57, pp. 2005–2014, Aug 2009.

[62] J. R. Shewchuk, "Lecture notes on delaunay mesh generation," 1999.

[63] X. Meng, A. Vukovic, T. M. Benson, and P. Sewell, "Extended capability models for carbon fiber composite (cfc) panels in the unstructured transmission line modeling (utlm) method," *IEEE Transactions on Electromagnetic Compatibility*, vol. 58, no. 3, pp. 811–819, 2016.

[64] L. Matthews, A. Vukovic, C. Mellor, P. Sewell, and T. Benson, "Time-domain modelling of solid state rf receiver protection systems," in *2020 14th European Conference on Antennas and Propagation (EuCAP)*, pp. 1–5, 2020.

[65] K. Yan, A. Vukovic, P. Sewell, and T. M. Benson, "Two-dimensional thermal diffusion equation solver based on unstructured transmission-line modelling and optimal delaunay triangular meshes," *IEEE Journal on Multiscale and Multiphysics Computational Techniques*, vol. 7, pp. 268–275, 2022.

[66] A. Harvey, "Standard waveguides and couplings for microwave equipment," *Proceedings of the IEE-Part B: Radio and Electronic Engineering*, vol. 102, no. 4, pp. 493–499, 1955.

[67] T. Rozzi, F. Moglie, A. Morini, W. Gulloch, and M. Politi, "Accurate full-band equivalent circuits of inductive posts in rectangular waveguide," *IEEE transactions on microwave theory and techniques*, vol. 40, no. 5, pp. 1000–1009, 1992.

[68] Y. Leviatan, P. G. Li, A. T. Adams, and J. Perini, "Single-Post Inductive Obstacle in Rectangular Waveguide," *Microwave Theory and Techniques, IEEE Transactions on*, vol. 31, no. 10, pp. 806–812, 1983.

[69] R. Beyer and F. Arndt, "Efficient modal analysis of waveguide filters including the orthogonal mode coupling elements by an mm/fe method," *IEEE Microwave and Guided Wave Letters*, vol. 5, pp. 9–11, Jan 1995.

[70] everythingRF.com, "Wr90 — wg16 — r100 - rectangular waveguide size."

[71] ELECTRICALTECHNOLOGY.ORG, Sep 2022.

[72] R. D, D. Ramakrishnan, S. Kavitha, R. Sivasakthivel, C. Latha, and K. Ramaswamy, "Classification of silicon (si) wafer material defects in semiconductor choosers using a deep learning shufflenet-v2-cnn model," *Advances in Materials Science and Engineering*, vol. 2022, pp. 1–12, 09 2022.

[73] J. Allison, *Electronic engineering semiconductors and devices*. 1990.

[74] B. Gallagher, "Introduction to solid state physics part 2 - lecture notes."

[75] "Properties of Silicon from the NSM archive, available at http://www.matprop.ru/Si_electric.

[76] "Aluminium gallium arsenide — Wikipedia, the free encyclopedia," 2022. [Accessed online at https://en.wikipedia.org/w/index.php?title=Aluminium_gallium_arsenide&oldid=1070254453].

[77] G. Kron, "Equivalent circuit of the field equations of maxwell-i," *Proceedings of the IRE*, vol. 32, no. 5, pp. 289–299, 1944.

[78] G. Kron, "Equivalent circuits to represent the electromagnetic field equations," *Phys. Rev.*, vol. 64, pp. 126–128, Aug 1943.

[79] J. Whinnery and S. Ramo, "A new approach to the solution of high-frequency field problems," *Proceedings of the IRE*, vol. 32, no. 5, pp. 284–288, 1944.

[80] J. Whinnery, C. Concordia, W. Ridgway, and G. Kron, "Network analyzer studies of electromagnetic cavity resonators," *Proceedings of the IRE*, vol. 32, no. 6, pp. 360–367, 1944.

[81] J. Whinnery and H. Jamieson, "Equivalent circuits for discontinuities in transmission lines," *Proceedings of the IRE*, vol. 32, no. 2, pp. 98–114, 1944.

[82] P. B. Johns and R. L. Beurle, "Numerical solution of 2-dimensional scattering problems using a transmission-line matrix," in *Proceedings of the Institution of Electrical Engineers*, vol. 118, pp. 1203–1208, IET, 1971.

[83] P. Russer, *The Transmission Line Matrix Method*. 01 2004.

[84] C. Christopoulos, *The Transmission-Line Modeling (TLM) Method in Electromagnetics*. Morgan and Claypool Publishers, 2006.

[85] P. B. Johns, "Numerical calculations for scattering in waveguides using a transmission line matrix," in *1971 2nd European Microwave Conference*, vol. 2, pp. 1–1, Aug 1971.

[86] P. Johns, "Application of the transmission-line-matrix method to homogeneous waveguides of arbitrary cross-section," in *Proceedings of the Institution of Electrical Engineers*, vol. 119, pp. 1086–1091, IET, 1972.

[87] T. Rowbotham and P. Johns, "Waveguide analysis by random walks," *Electronics Letters*, vol. 8, no. 10, pp. 251–253, 1972.

[88] S. Akhtarzad and P. Johns, "Transmission-line-matrix solution of waveguides with wall losses," *Electronics Letters*, vol. 9, no. 15, pp. 335–336, 1973.

[89] P. Johns, "The solution of inhomogeneous waveguide problems using a transmission-line matrix," *IEEE Transactions on Microwave Theory and Techniques*, vol. 22, pp. 209–215, Mar 1974.

[90] P. Johns, "On the relationship between tlm and finite-difference methods for maxwell's equations (short paper)," *IEEE Transactions on Microwave Theory and Techniques*, vol. 35, pp. 60–61, Jan 1987.

[91] S. Akhtarzad and P. Johns, "Solution of maxwell's equations in three space dimensions and time by the tlm method of numerical analysis," in *Proceedings of the Institution of Electrical Engineers*, vol. 122, pp. 1344–1348, IET, 1975.

[92] P. Johns and S. Akhtarzad, "Three-dimensional numerical analysis of microwave cavities using the tlm method," in *1975 IEEE-MTT-S International Microwave Symposium*, pp. 200–201, May 1975.

[93] S. Akhtarzad and P. Johns, "Three-dimensional transmission-line matrix computer analysis of microstrip resonators," *IEEE Transactions on Microwave Theory and Techniques*, vol. 123, pp. 990–997, Dec 1975.

[94] S. Akhtarzad and P. Johns, "Tlmres - the tlm computer program for the analysis of microstrip resonators (computer program descriptions)," *IEEE Transactions on Microwave Theory and Techniques*, vol. 24, pp. 675–675, Oct 1976.

[95] A. M. Lohse, P. B. Johns, and A. Wexler, "Computer graphics for transient fields," *IEEE Transactions on Education*, vol. 20, pp. 64–68, Feb 1977.

[96] W. Hoefer, "The transmission-line matrix method - theory and applications," *IEEE Transactions on Microwave Theory and Techniques*, vol. 33, no. 10, pp. 882–893, 1985.

[97] P. Saguet and E. Pic, "Utilisation d'un nouveau type de noeud dans la méthode tlm en 3 dimensions (usage of a new type of node in the 3d tlm method)," *Electronics Letters*, vol. 18, no. 11, pp. 478–480, 1982.

[98] P. Saguet and S. Tedjini, "Méthode des lignes de transmission en trois dimensions: modification du processus de simulation," in *Annales des télécommunications*, vol. 40, pp. 145–152, Springer, 1985.

[99] R. Allen, A. Mallik, and P. Johns, "Numerical results for the symmetrical condensed tlm node," *IEEE Transactions on Microwave Theory and Techniques*, vol. 35, pp. 378–382, Apr 1987.

[100] P. Naylor and C. Christopoulos, "A new wire node for modeling thin wires in electromagnetic field problems solved by transmission line modeling," *Microwave Theory and Techniques, IEEE Transactions on*, vol. 38, pp. 328 – 330, 04 1990.

[101] L. Cascio, G. Tardioli, and W. Hoefer, "Modeling of nonlinear active and passive devices in three-dimensional tlm networks," in *1997 IEEE*

MTT-S International Microwave Symposium Digest, vol. 2, pp. 383–386 vol.2, June 1997.

[102] M. Sobhy, E. Hosny, P. Russer, B. Isele, and C. Christopoulos, "Interfacing the transmission line method (tlm) and state-space (ss) techniques to analyse general non-linear structures," in *1994 Second International Conference on Computation in Electromagnetics*, pp. 299–302, 1994.

[103] N. I. Corp., "Spice - definition of a spice model," 2021.

[104] V. Thomas, M. Jones, M. Piket-May, A. Taflove, and E. Harrigan, "The use of spice lumped circuits as sub-grid models for fdtd analysis," *IEEE Microwave and Guided Wave Letters*, vol. 4, no. 5, pp. 141–143, 1994.

[105] P. Russer, P. P. So, and W. Hoefer, "Modeling of nonlinear active regions in tlm (distributed circuits)," *IEEE Microwave and guided wave letters*, vol. 1, no. 1, pp. 10–13, 1991.

[106] N. Kriplani, S. Bowyer, J. Huckaby, and M. Steer, "Modelling of an esaki tunnel diode in a circuit simulator," *Active and Passive Electronic Components*, vol. 2011, 01 2011.

[107] N. Orhanovic, R. Raghuram, and N. Matsui, "Full wave analysis of planar interconnect structures using fdtd-spice," in *2001 Proceedings. 51st Electronic Components and Technology Conference (Cat. No.01CH37220)*, pp. 489–494, 2001.

[108] I. Scott, V. Kumar, C. Christopoulos, D. Thomas, S. Greedy, and P. Sewell, "Integration of behavioral models in the full-field tlm method," *IEEE Transactions on Electromagnetic Compatibility* -

IEEE TRANS ELECTROMAGN COMPAT, vol. 54, pp. 359–366, 04 2012.

[109] H. Jiang, M. Mukherjee, J. Zhou, and J. Lloret, "Channel modeling and characteristics for 6g wireless communications," *IEEE Network*, vol. 35, no. 1, pp. 296–303, 2021.

[110] H. Patel, K. Kellogg, H. Morales, L. Dunleavy, R. Jones, and P. Head, "Nonlinear modeling of a high peak power pin limiter," *Microwave Journal*, vol. 62, no. 1, p. 60, 2019.

[111] J. Paul, C. Christopoulos, D. Thomas, and X. Liu, "Time-domain modeling of electromagnetic wave interaction with thin-wires using tlm," *IEEE Transactions on Electromagnetic Compatibility*, vol. 47, pp. 447–455, Aug 2005.

[112] I. Scott, G. Kergonou, C. Christopoulos, F. Canavero, S. Greedy, D. W. Thomas, and P. Sewell, "On the integration of behavioral component descriptions in the full-wave transmission-line modeling method," in *Proc. 29th Prog. Electromagn. Res. Symp.*, pp. 853–857, 2011.

[113] I. Scott, C. Christopoulos, D. Thomas, S. Greedy, and P. Sewell, "On the modeling of complex circuits using behavioral component descriptions embedded into the full-wave tlm method," *2011 30th URSI General Assembly and Scientific Symposium, URSIGASS 2011*, 08 2011.

[114] J. Paul, C. Christopoulos, and D. W. P. Thomas, "Correction to "time-domain modeling of electromagnetic wave interaction with thin-wires using tlm" [aug 05 447-455]," *IEEE Transactions on Electromagnetic Compatibility*, vol. 50, pp. 450–451, May 2008.

[115] P. So and W. Hoefer, "A tlm-spice interconnection framework for coupled field and circuit analysis in the time domain," *IEEE Transactions on Microwave Theory and Techniques*, vol. 50, no. 12, pp. 2728–2733, 2002.

[116] J. Angulo, I. Dodd, L. Green, S. Huq, A. Muranyi, and B. Ross, "Ibis modeling cookbook for ibis version 4.0," 2005.

[117] A. K. Varma, M. Steer, and P. D. Franzon, "Improving behavioral io buffer modeling based on ibis," *IEEE Transactions on Advanced Packaging*, vol. 31, no. 4, pp. 711–721, 2008.

[118] R. Leventhal, "How to use the ibis model," 2001.

[119] M. Casamayor, "A first approach to ibis models : What they are and how they are generated by," 2004.

[120] S. Mimouni, A. Saidane, D. Chalabi, and M. Abboun-Abid, "Transmission line matrix (tlm) modeling of self-heating in power pin diodes," *Microelectronics Journal*, vol. 79, pp. 64–69, 2018.

[121] R. H. Caverly and S. Khan, "Electrothermal modeling of microwave and rf pin diode switch and attenuator circuits," in *2013 IEEE MTT-S International Microwave Symposium Digest (MTT)*, pp. 1–4, 2013.

[122] R. H. Caverly, "Pin diode switching speed for mri applications," in *2020 IEEE MTT-S International Microwave Biomedical Conference (IMBioC)*, pp. 1–3, 2020.

[123] M. U. Nazir, M. Kashif, N. Ahsan, and Z. Y. Malik, "Pin diode modelling for simulation and development of high power limiter, digitally controlled phase shifter and high isolation spdt switch," in *Proceedings of 2013 10th International Bhurban Conference on Applied Sciences & Technology (IBCAST)*, pp. 439–445, 2013.

[124] P. Sun, P. Upadhyaya, D.-H. Jeong, D. Heo, and G. S. La Rue, "A novel sige pin diode spst switch for broadband t/r module," *IEEE Microwave and Wireless Components Letters*, vol. 17, no. 5, pp. 352–354, 2007.

[125] R. Caverly, N. Drozdovski, L. Drozdovskaia, and M. Quinn, "Spice modeling of microwave and rf control diodes," in *Proceedings of the 43rd IEEE Midwest Symposium on Circuits and Systems (Cat.No.CH37144)*, vol. 1, pp. 28–31 vol.1, 2000.

[126] Skyworks Solutions Inc., "Silicon PIN Diode Chips - accessed at https://www.skyworksinc.com/-/media/SkyWorks/Documents/Products/301-400/BRO375_-09A.pdf."

[127] Macom, "Silicon limiter diodes - accessed at https://cdn.macom.com/datasheets/ma4l_madl